CHARACTERIZATION OF CALCIUM-SILICATE-HYDRATE AND CALCIUM-ALUMINO-SILICATE-HYDRATE

BY

WILLIAM ALBERT HUNNICUTT

THESIS

Submitted in partial fulfillment of the requirements
for the degree of Master of Science in Civil Engineering
in the Graduate College of the
University of Illinois at Urbana-Champaign, 2013

Urbana, Illinois

Adviser:

Professor Leslie Struble

ABSTRACT

The primary objectives of this thesis were to synthesize calcium silicate hydrate (C-S-H) and calcium aluminosilicate hydrate (C-A-S-H) and characterize their structures with varying Ca/Si ratios and aluminum content. As a secondary objective, carbonation behavior in synthesized C-S-H was studied. C-S-H was synthesized in the lab using two different methods: the double decomposition of calcium nitrate and sodium silicate solutions, and the direct reaction between calcium oxide and fumed silica in water. In C-A-S-H the source of aluminum was sodium aluminate or aluminum nitrate. A variety of phases were present depending on the degree of carbonation of the C-S-H or C-A-S-H. C-S-H, C-A-S-H, alumina/silica gel, calcite, aragonite, and vaterite were all observed throughout the course of study. X-ray diffraction (XRD) was the technique used to identify these phases. XRD was also used to explore the changes in crystal structure with varying Ca/Si ratios and aluminum content. No significant changes to the crystal structure were found. The effect of Ca/Si ratio, aluminum content, and synthesis method were studied on the molecular scale using ^{29}Si and ^{27}Al nuclear magnetic resonance spectroscopy (NMR). An increasing Ca/Si ratio has the effect of a shorter alumino-silicate chain length and an increase in aluminum content increases the alumino-silicate chain length. Aluminum substitution occurred primarily in the bridging tetrahedron position, but also in the pairing tetrahedron position. Aluminum uptake was also examined with respect with Ca/Si ratio and was found to decrease with increasing Ca/Si ratio. The changes in chemical environment of the aluminum ion with varying Ca/(Si+Al) ratios was also observed by ^{27}Al NMR. It was found that as the Ca/(Si+Al) ratio increased, the amount of chemical shielding of the ^{27}Al nuclei decreased . Carbonation of C-S-H was also examined and it was found that the double decomposition synthesis method allows for more rapid carbonation of the C-S-H. The source of increased carbonation rate is the high pH of the solutions.

ACKNOWLEDGEMENTS

I would like to first, and foremost, thank my advisor, Professor Leslie Struble, for her guidance and support throughout this research project. Her dedication to her research and students is unparalleled and I am grateful I had the opportunity to work with her. Considerable thanks go to Dr. Jennifer Rapp as well for her invaluable help with nuclear magnetic resonance spectroscopy. Without her constant support this project would not have been possible. Professor Paramita Mondal has also contributed through her helpful discussions and I look forward to my future work with her.

My fellow colleagues deserve recognition for their helpful discussions on a multitude of topics related to this project. Eric Kim and Xu Chen provided many useful conversations on nuclear magnetic resonance and the influence of alkali ions in polymerized structures. Sravanthi Puligilla's knowledge of, and willingness to discuss, carbonation behavior was appreciated. Drew Bishop and Victor Elizondo aided me in the laboratory frequently over the past two years and their time is appreciated.

A special thank you goes to Tom Wilson and Binh Phan at CalPortland – Central Laboratory for their XRF analysis of my samples.

TABLE OF CONTENTS

1. INTRODUCTION 1

2. LITERATURE REVIEW 4

  2.1 NUCLEAR MAGNETIC RESONANCE SPECTROSCOPY 4

  2.2 STRUCTURE OF CALCIUM SILICATE HYDRATE 5

  2.3 EFFECT OF CA/SI RATIO ON MOLECULAR STRUCTURE 13

  2.4 EFFECT OF ALUMINUM ON MOLECULAR STRUCTURE 16

  2.5 CARBONATION OF C-S-H 19

3. EXPERIMENTAL PROCEDURES 21

  3.1 SYNTHESES 21

  3.2 X-RAY DIFFRACTION 27

  3.3 NUCLEAR MAGNETIC RESONANCE 28

  3.4 X-RAY FLUORESCENCE 30

  3.5 THERMOGRAVIMETRIC ANALYSIS 30

4. RESULTS 31

  4.1 XRD 32

  4.2 ^{29}Si NMR 44

  4.3 ^{27}Al NMR 76

4.4 XRF 96

4.5 TGA 105

5. DISCUSSION 108

5.1 EFFECT OF CA/SI RATIO 108

5.2 EFFECT OF AL INCORPORATION 111

5.3 DEPENDENCE OF AL UPTAKE ON CA/SI RATIO 115

5.4 CARBONATION 121

6. CONCLUSIONS 125

7. REFERENCES 127

1. INTRODUCTION

Calcium silicate hydrate (C-S-H) is the main binding component of portland cement paste, constituting 60-70% of a fully hydrated paste [1]. In portland cement, β-C_2S and C_3S hydrate to form calcium hydroxide (CH) and C-S-H. Cement shorthand nomenclature is used throughout this thesis, where C=CaO, S=SiO_2, A=Al_2O_3, H=H_2O. C-S-H and C-A-S-H imply a variable composition of these species. C-S-H is nearly amorphous, has a variable stoichiometry, and is able to incorporate guest ions, most notably aluminum. The natural calcium silicate hydrate tobermorite has been used extensively as a model for the molecular structure of C-S-H. It is likely that incorporation of aluminum into the C-S-H structure plays a role in the chemical and mechanical behavior of C-S-H [2].

Supplementary cementitious materials (SCMs) can be added to concrete mixtures to replace portland cement in order to gain beneficial properties. The most commonly used SCMs, fly ash and slag, contain substantial amounts of reactive aluminum. Kalousek was the first to show that aluminum can be incorporated into the natural calcium silicate hydrate tobermorite [3]. Since then, there have been numerous reports of aluminum in the C-S-H structure [2, 4, 5]. Aluminum substituted C-S-H (C-A-S-H) is formed when portland cement is hydrated in the presence of Al^{3+} ions [6], which are present when fly ash and slag are dissolved in water. The benefits of C-A-S-H can be achieved in concrete by adding SCMs that contain reactive aluminum to concrete mixtures.

The primary objective of the work presented in this thesis is to synthesize C-S-H and C-A-S-H, which requires substantial detailed characterization techniques. Two different synthesis methods are used, differing in starting materials and reaction time. C-S-H and C-A-S-H of different Ca/Si and Al/Si ratios are synthesized. The molecular structure of C-S-H and C-A-S-H was studied when varying these ratios. Additionally, the effect of Ca/Si ratio on the incorporation of aluminum into the structure was studied. The changes in molecular structure associated with changes in the Ca/Si and Al/Si ratios are thought to influence the mechanical properties of C-S-H and C-A-S-H and will be the subject of future work. The primary methods of characterization were: X-ray diffraction (XRD) and magic angle spinning nuclear magnetic resonance (MAS-NMR).

Carbonation of C-S-H and C-A-S-H was observed in this work and was subsequently studied. The effect of carbonation of the molecular structure of C-S-H and C-A-S-H is studied, along with factors that influence the rate of carbonation, such as the introduction of sodium ions and changes in pH.

This thesis is divided into the following chapters. Chapter 2 is a literature review discussing nuclear magnetic resonance spectroscopy, the molecular structure of C-S-H and C-A-S-H with varying Ca/Si and Al/Si ratios, and carbonation of C-S-H with guest ions. Chapter 3 describes experimental procedures, including syntheses and characterization techniques. Chapter 4 presents the results of the characterization techniques with analysis of XRD patterns and NMR spectra. Chapter 5 is a discussion of the results and in Chapter 6 conclusions are drawn.

2. LITERATURE REVIEW

2.1 NUCLEAR MAGNETIC RESONANCE SPECTROSCOPY

Nuclear magnetic resonance spectroscopy (NMR) is a powerful characterization method capable of providing information about the structure of materials. The method exploits the interaction of nonzero spin nuclei and an external magnetic field to gain information about the local atomic environment of a specific nucleus. In cementitious materials, the ^{29}Si and ^{27}Al nuclei are the most widely studied nuclei. The NMR of solids requires spinning the sample very quickly (kHz) at an angle of 54.7°, called the magic angle. This simulates the Brownian motion of a liquid that is required for NMR experiments of solids. Different nuclei have different natural abundances and spins which affect the clarity of the resulting spectra. The ^{29}Si nucleus has a spin of 1/2 and a natural abundance of 4.7% and the ^{27}Al has a spin of 5/2 and a natural abundance of 100%. Nuclei with a spin greater than 1/2 have a non-spherical electrical charge distribution that causes an electric quadrupole moment. This causes the spectral lines to be significantly broadened and interact differently with different strengths of magnetic field due to the inhomogeneous interaction with the magnetic field [7]. This often leads to difficult interpretation and limited data from the spectrum. The natural abundance of a nucleus affects the time required for an experiment to achieve an acceptable signal/noise ratio. A higher natural abundance requires less experimental time.

Much information can be gained from the ^{29}Si nucleus in cementitious materials. The presentation of structural information obtained from ^{29}Si NMR in silicates often uses Q notation: $Q^n(m\mathrm{Al})$, where Q indicates a silica tetrahedron forming bridges through n oxygen atoms with adjacent tetrahedra, of which m are alumina tetrahedra, where n and m range from 0 to 4 [8]. A Q^1 structure would have a single silica tetrahedron bonded to one other silica tetrahedron, Q^2 is a silicon tetrahedron bonded to two silica tetrahedra, and $Q^2(1\mathrm{Al})$ is a silica tetrahedron bonded to one silica tetrahedron and one alumina tetrahedron.

The information gained from ^{27}Al NMR is much more limited due to the quadrupolar interaction of the 5/2 spin nucleus. The quadrupolar interaction causes extreme line broadening that makes it nearly impossible to make fine distinctions in the local atomic environment. An increase in the magnetic field used greatly reduces these effects. The basic ^{27}Al NMR experiment only gives information about the coordination of the aluminum nucleus, and not information on specific local bonding to the nucleus. Methods do exist that can gleam more information from the ^{27}Al nucleus, such as multi-quantum NMR, double rotation NMR, and dynamic angle spinning NMR [9].

2.2 STRUCTURE OF CALCIUM SILICATE HYDRATE

The chemical composition and molecular structure of calcium silicate hydrate (C-S-H) is thought to substantially affect many properties of concrete, where it is the primary binding phase. The structure of C-S-H has been studied extensively since the first structural models were presented in 1952 [10]. Due to the low crystallinity of C-S-H, X-ray diffraction (XRD) has not been the most useful method for characterizing the material. Instead, more advanced techniques such as magic angle spinning nuclear magnetic resonance (MAS-NMR), which detects short-range order, have aided much in solving the structure of C-S-H.

2.2.1 STRUCTURAL MODELS

Several models for the molecular structure of C-S-H have been proposed, which broadly portray it is a non-crystalline calcium oxide layer sandwiched by short and discrete silicate chains [10, 11, 12, 13]. These models bear resemblance to the naturally forming tobermorite and jennite, in which a calcium oxide layer is sandwiched by infinite silicate chains. The silicate chain is comprised of tetrahedral silica in a “dreierketten” arrangement, in which the smallest repeating unit is three tetrahedra, one bridging and two pairing. Space between silicate chains is referred to as the “interlayer”. A schematic of the structure is presented in Figure 1. It has been observed experimentally that the length of the silicate chain follows $3n$-1, where n is an integer [10]. This is critical evidence of the “dreierketten” structure. The pairing tetrahedra share two oxygen atoms with the calcium oxide layer and the bridging tetrahedra share only one oxygen atom with the calcium oxide layer.

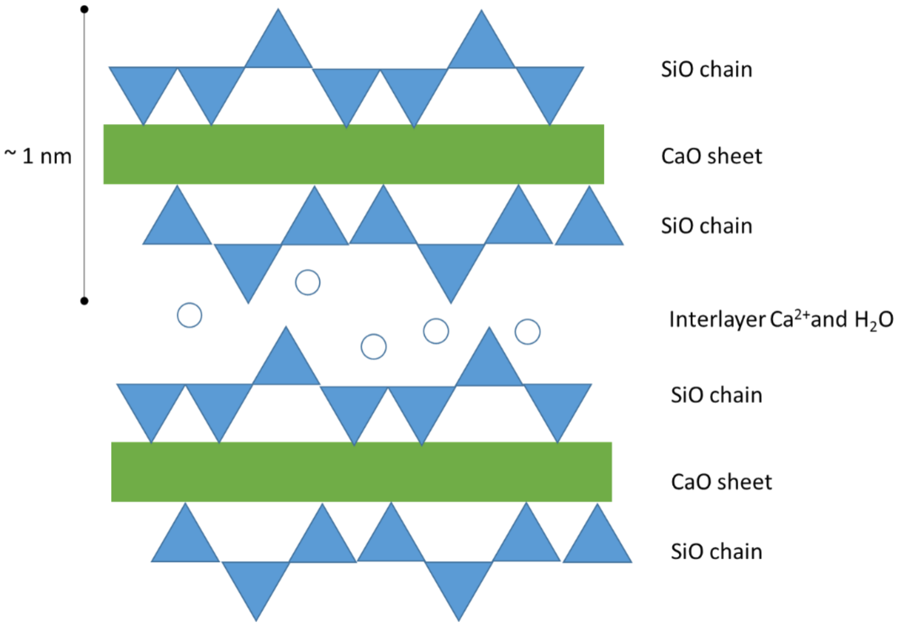

Figure 1: Idealized structure of C-S-H.

The variability of the Ca/Si ratio in C-S-H has produced many slightly different models to account for the variation. It has been observed that C-S-H has a variable stoichiometry with Ca/Si ratio in the range of 1.2 to 2.1 [14]. Tobermorite and jennite have Ca/Si ratios of 0.83 and 1.5, respectively. Therefore, to account for this variation in Ca/Si ratio, the tobermorite and jennite models for C-S-H need to be modified. Taylor and Howison [15] suggested a tobermorite model in which the Ca/Si ratio can be raised above 0.83 by the omission of bridging silica tetrahedra and replacement by calcium ions in the interlayer. Kurczyk and Schwiete [16] observed Ca/Si ratios between 1.80 and 1.92 when β-C_2S and C_3S were hydrated and proposed a model based on tobermorite with calcium hydroxide and water in the interlayer to account for the higher Ca/Si ratio. The silicate chain length was presumed to be infinite. Stade et al. proposed a model very similar to that of Kurczyk and Schwiete, with the notable difference of allowing finite silicate chains [10]. Kurczyk and Schwiete assumed that all silicate dimers were fully protonated. Taylor [13] continued to develop his earlier work in modeling the structure of C-S-H by proposing a model that is composed of structural components of jennite and 1.4 nm tobermorite. The range in Ca/Si ratio was explained by omission of bridging tetrahedra, and was linearly proportional to the reciprocal of the silicate chain length. However, limiting assumptions were made about protonation of silica tetrahedra.

Richardson and Groves [12, 17] proposed a general model that could be interpreted from the tobermorite/jennite or tobermorite/calcium hydroxide perspective. This model did not fix the level of protonation of the silicate chain. The generalized model is very similar to many of the previous models for the structure of C-S-H, but its generality allows for the specific inconsistencies of other models to be compensated. Cong and Kirkpatrick [11] proposed a defect-tobermorite structure similar to 1.4 nm tobermorite, except with a substantial amount of defects and less order. These defects stem from the omission of bridging tetrahedra and the silica tetrahedra are displaced and rotated relative to the CaO layer. Electroneutrality is maintained by Ca^{2+} and OH^- in the interlayer depending on the availability of Ca^{2+}. Richardson [18] noted that the models by Cong and Kirkpatrick [11], Nonat and Lecoq [19], and Chen et al. [20] are very similar to the generalized Richardson and Groves model.

2.2.2 INCORPORATION OF ALUMINUM

Richardson and Groves' model also accounts for guest ions to be incorporated into the C-S-H structure. Kalousek [3] was the first to note that aluminum ions can substitute for silicon in the silicate chain in tobermorite and suggested that substitution only occurs in the bridging tetrahedra. Komarneni et al. [21] synthesized tobermorite with aluminum by direct reaction in a Parr bomb and examined samples by XRD and MAS-NMR. The authors observed that aluminum is tetrahedrally coordinated in tobermorite. Aluminum occurred in both Q^2 (chain) and Q^3 (branching) sites, as inferred from ^{29}Si NMR. A schematic of aluminum in a Q^3 site is presented in Figure 2. Faucon et al. [5] noted tetrahedral and octahedral aluminum in C-A-S-H synthesized by direct reaction of calcium hydroxide, silica, and gypsite in water. The octahedral aluminum was suggested to occur in the octahedral layer or interlayer of C-A-S-H. Two different tetrahedral aluminum sites were assigned: In the bridging tetrahedra and the pairing tetrahedra positions with a majority being in the bridging position [22, 23]. These assignments were based on an advanced NMR method known as triple quantum NMR (3Q-NMR), which gives better resolution of quadrupolar nuclei, in addition to ^{29}Si MAS-NMR, which indicated aluminum linkage to tetrahedral silicon. The maximum Al[4]/(Si+Al[4]) was 0.26. The authors noted that this is still well below the expected maximum of 0.50 in accordance with the Lowenstein rule, which states that no Al-O-Al bonds will occur. The explanation of this is that high electrostatic repulsion is induced within the aluminosilicate chains by the net negative charge of aluminum and that a minimum distance between aluminum tetrahedra is required. The addition of sodium into the chemical system allowed for a higher degree of aluminum substitution, most likely due to charge balancing of aluminum by sodium ions in the interlayer.

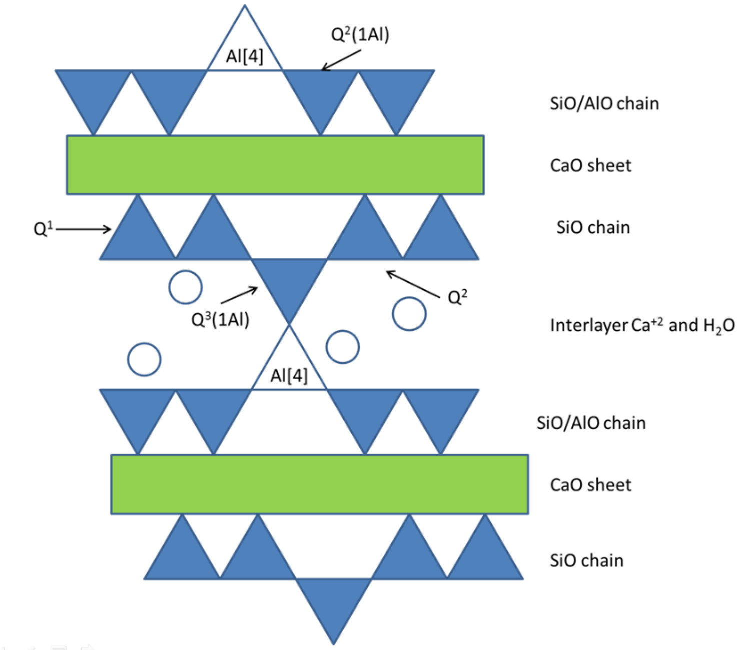

Figure 2: Idealized structure of C-A-S-H with crosslinking.

Sun et al. [2] found tetrahedral, pentahedral, and octahedral aluminum in C-S-H synthesized from the double decomposition of sodium silicate and calcium nitrate. Double decomposition refers to the chemical reaction of two solutions that produces two products, one precipitates and the other remains in solution. Tetrahedral aluminum occurred in the bridging tetrahedra site while pentahedral and octahedral aluminum occur in the interlayer and possibly on particle surfaces. The presence of aluminum substituting for calcium in the octahedral layer was ruled out due to lack of change in the XRD pattern when aluminum was incorporated into the structure. Incorporation of aluminum in the octahedral layer would have caused a change in the (hk0) dimensions. The tetrahedral aluminum in the bridging site was found to be in three different chemical environments by ^{29}Si MAS-NMR and ^{27}Al MAS-NMR: Q^3 sites bonding across the interlayer, Q^2 sites charge balanced by Ca^{2+}, Na^+, or H^+ in the interlayer, and Q^2 sites charged balanced by pentahedral and octahedral aluminum in the interlayer. It was suggested that aluminum enters the bridging tetrahedra site preferentially since this position shares only one bond with the calcium oxide layer, and the pairing position shares two bonds with the calcium oxide layer. Therefore, the bridging position is more able to accommodate a different size atom. The Al[4]-O bond length is approximately 0.01 nm longer than the Si-O bond length and there is more room to fit into the C-S-H structure at bridging sites than pairing sites. The maximum observed substitution of silicon by tetrahedral aluminum (Al[4]/(Si+Al[4])) was 0.22. Samples with longer reaction times had an Al[4]/(Si+Al[4]) of 0.17, corresponding to 1/6 of all tetrahedra, or 1/2 of bridging tetrahedra.

Andersen et al. [6, 24] hydrated white portland cement in water and a solution of $NaAlO_2$. Tetrahedral, pentahedral, and octahedral aluminum were detected by ^{27}Al MAS-NMR, but it was determined that only tetrahedral aluminum occurs in the silicate chain while pentahedral aluminum occurs in the interlayer. The octahedral aluminum was thought to occur in other aluminate phases, such as ettringite, monosulfate, and a third aluminate hydrate phase by evidence from cross polarization MAS-NMR experiments. When Faucon [25] found octahedral aluminum, the authors assigned it to the octahedral layer of C-A-S-H, substituting for calcium. However, Andersen et al. produced substantial evidence that octahedral aluminum does not substitute for calcium in the octahedral layer in C-S-H [6, 24]. Tetrahedral aluminum was found to occur only in Q^2 sites by ^{29}Si MAS-NMR. The amount of aluminum substitution in C-S-H (Al/Si) ranged from 0.059 to 0.104. The authors suggested that high amounts of aluminum (Al/Si≈0.20) can only be incorporated into synthetic C-S-H when the Al[4]/Si ratios of the initial reagents are high, such as in Faucon's work [5, 22, 23].

Schneider et al. [26] activated blast-furnace slag cements with various activation and curing conditions. The ^{27}Al and ^{29}Si MAS-NMR corroborated to indicate that tetrahedral aluminum is occurring in the silicate chain of C-S-H, but it was not possible to discern whether aluminum was in the bridging and pairing positions. It was found that less substitution occurred when activated with CH and more substitution occurred when activated with solutions containing high concentrations of Na_2O. It is thought that sodium plays a key role in charge balancing the aluminum tetrahedra.

Molecular dynamics simulations have also allowed for study of the incorporation of aluminum in C-S-H and gives a slightly different insight to the nature of aluminum substitution. Faucon et al. [27] studied C-S-H with Ca/Si ratios of 0.66 and 0.83, which are closer to that of tobermorite than C-S-H from portland cement hydration, with the incorporation of aluminum. When aluminum was placed in the bridging tetrahedra and the structure was relaxed, no rupture of the aluminosilicate chain was observed and the charge deficit was compensated primarily by protons. When aluminum is positioned in the pairing tetrahedra the chain breaks and Q^1 tetrahedra are formed. It was observed that, despite this reorganization, there was no chain ending aluminum tetrahedron.

Manzano et al. [28] showed that, when aluminum is incorporated, the 3*n*-1 chain length is still maintained, as observed in C-S-H not substituted by aluminum by Richardson [10]. It was thought that chain growth was caused by the merging of dimers to create pentamers. It was noted that the energy gains to create Si monomers was higher than to produce dimers, so the merging mechanism is secondary to monomer production. When aluminum provides the link between dimers the merging energy is significantly higher than when silicon provides the link, resulting in a more favorable process. Aluminum was also considered in the pairing and chain ending positions and it was found that aluminum is most favorable in the bridging position followed by pairing and chain ending. In a separate molecular dynamics study, Manzano et al. [29] noted that, as the Ca/Si ratio of the C-S-H increases, aluminum is more likely to be incorporated into the pairing tetrahedra position.

2.3 EFFECT OF CA/SI RATIO ON MOLECULAR STRUCTURE

The Ca/Si ratio of C-S-H is variable in the range of 1.2 to 2.1 in hydrated cement [14]. This variability has an effect on the molecular structure of C-S-H. Modern and well accepted models for the structure of C-S-H consider the change in Ca/Si ratio by omitting bridging silica tetrahedra and adding interlayer Ca^{2+} when the Ca/Si ratio is increased [10]. Grutzeck et al. [30] synthesized C-S-H by direct reaction of fumed silica and freshly calcined $CaCO_3$ in water with Ca/Si ratios ranging from 0.00 to 1.31. Samples with a Ca/Si ratio below 0.12 consisted of Q^3 and Q^4 silica tetrahedra at -100.7 ppm and 114.5 ppm as measured by ^{29}Si NMR. The sample at Ca/Si=0.12 Q^3 and Q^4

sites were still present and a new peak at -85.0 ppm assigned to Q^2 appeared. At Ca/Si=0.91 a small shoulder attributed to Q^1 appeared, indicating the end of a silicate chain. At Ca/Si ratios above 1.07 contained only peaks attributable to Q^2 and Q^1.

Cong and Kirkpatrick [11] synthesized C-S-H with Ca/Si ratios ranging from 0.41 to 1.85. The highest Ca/Si ratio that formed phase-pure C-S-H was 1.56, above which calcium hydroxide was also formed. Amorphous silica was present when the Ca/Si ratio was 0.41. The crystal cell dimensions of the C-S-H varied with Ca/Si ratios. The ‘a’ dimension increased and the ‘b’ and ‘c’ dimensions decreased with increasing Ca/Si ratios. The ^{29}Si NMR results indicate that samples with Ca/Si ratios at or below 0.79 had Q^3 peaks at approximately -94 ppm. The sample with Ca/Si=0.41 also had Q^4 peaks which were assigned to silica gel. In higher Ca/Si ratios, only Q^1 and Q^2 peaks were observed. The ratio $Q^1/\Sigma Q^i$ was used as indicator of silicate chain polymerization and decreased as Ca/Si increased. At Ca/Si>1.3 the amount of polymerization decreased less rapidly than at lower Ca/Si ratios.

Garcia-Lodeiro et al. [31] synthesized C-S-H by double decomposition of sodium silicate and calcium nitrate with Ca/Si ratios of ranging from 0.39 to 1.54. The authors noted that substantial carbonation occurred in all samples except for those with Ca/Si ratios of 1.02 and 1.54. This was intentionally done by exposing the reaction to laboratory air during synthesis. In the samples with Ca/Si ratios of 0.75, 0.67, and 0.65 a peak at approximately -83 ppm appeared which was assigned to Q^2 silica tetrahedra in the bridging position, in addition to Q^2 in the pairing position and Q^1. The other samples with higher Ca/Si also showed intensity in this range, but a clear peak could not be identified due to overlap of the Q^2 pairing and Q^1 peaks. In the two samples that were not carbonated, the mean chain length (MCL) of the silicate chain was 4.68 and 3.02 silica tetrahedra for Ca/Si ratios of 1.02 and 1.54, respectively.

Faucon et al. [27] conducted molecular dynamics simulations with Ca/Si ratios of 0.66 and 0.83. At Ca/Si=0.66 the chains were infinitely long and at Ca/Si=0.83 about 15% of the silica tetrahedra were Q^1. When the Ca/Si=0.66 the oxygen atoms bonded to the bridging silica tetrahedra that were not shared with pairing tetrahedra were hydroxylated. When the Ca/Si=0.83 Ca^{2+} is in the interlayer and creates a charge deficit on the oxygen atoms bonded to the bridging silica tetrahedra that were not shared with pairing tetrahedra. This is the result of the rupture of the silicate chain and subsequent hydroxylation of the silica tetrahedra and formation of Q^1 environments.

Dolado et al. [1] used molecular dynamics simulations of C-S-H with varying Ca/Si ratios to examine the structure. C-S-H with Ca/Si ratios of 0.7, 1.0, 1.4, and 2.0 were simulated. It was found that the presence of Ca atoms decreases the rate of polymerization of the silica chain. The simulation with Ca/Si=0.7 had 15% Q^3+Q^4 environments and that proportion decreased with increasing Ca/Si ratios. At Ca/Si=2.0 all nonlinear environments were absent. Calcium ions were concluded to enforce linear structures. Additionally, the ratio of $Q^1/(Q^1+Q^2+Q^3)$, an inverse indicator of silicate chain length, increased as the Ca/Si ratio increased.

2.4 EFFECT OF ALUMINUM ON MOLECULAR STRUCTURE

When aluminum enters C-S-H the molecular structure is modified. Combinations of ^{29}Si and ^{27}Al NMR have provided much insight to the structure of C-A-S-H due to the ability to probe short-range order. A key modification to the molecular structure of C-(A)-S-H is the change in the mean chain length (MCL) of the silicate chain, which can be calculated from ^{29}Si NMR deconvoluted peak areas as [14]:

$$\mathrm{MCL} = \frac{2}{\frac{Q^1}{Q^1 + Q^2(0\mathrm{Al}) + \frac{3}{2}Q^2(1\mathrm{Al})}} \tag{1}$$

Sun et al. [2] synthesized C-A-S-H with Ca/(Al+Si) ratios of 0.86, 1.18 and 1.4 and with Al/(Al+Si) of 0.00, 0.08, 0.15, and 0.30 for each Ca/(Al+Si) and characterized the samples using ^{29}Si and ^{27}Al NMR. As aluminum was added the intensity of the Q^1 peak decreased and the intensity of the Q^2(1Al) peak increased, indicating an increase in MCL. Additionally, signal was present in the range that can be assigned to Q^3(1Al), which indicates linking of silicate chains through the bridging tetrahedra.

Puertas et al. [32] examined alkali activated slag cements, activated with waterglass or NaOH, and portland cement pastes. The ^{29}Si NMR indicated that C-S-H formed from hydration of portland cement was dominated by Q^1 and had a MCL of 3.80. Slags activated with NaOH had high Q^2(1Al) contents, MCL of 8.00, and low Q^3 content. In the slag pastes activated with waterglass large amounts of aluminum entered the structure and the MCL increase to 12.71. Higher amounts of Q^3 were detected, as well. The use of waterglass added silicon to the system and decreased the

Ca/Si ratio of the C-S-H. The decrease in Ca/Si ratio may be the cause of the difference between activated slag pastes.

Andersen et al. [6] hydrated white portland cement with water and with a solution of 0.3 M $NaAlO_2$. Aluminum from the $NaAlO_2$ solution was taken up into the bridging tetrahedra and the quantity of aluminum increased with hydration time. When hydration occurred in $NaAlO_2$ solution, the C-(A)-S-H had a slightly longer chain length at every time interval measured (12 hours to 1 year) than the C-(A)-S-H hydrated in water. The difference ranged between 0.08 and 0.58 tetrahedra.

Garcia-Lodeiro et al. [33] synthesized C-S-H from the double decomposition of calcium nitrate and sodium silicate solutions. A control sample and samples with NaOH, NaOH and $Al(NO_3)_3$, and NaOH and $Al(NO_3)_3$ and Na_2SiO_3 were characterized. The control sample was predominately Q^1 from ^{29}Si NMR while the rest of the samples showed large Q^2 peaks with small Q^1 peaks. Peaks assigned to Q^3 and Q^4 sites were also detected, most likely from a silica gel-like material with ionic substitutions. The MCL for samples the control sample and sample with NaOH were 3.05 and 9.44, respectively. MCL was not given for samples with NaOH and $Al(NO_3)_3$ and samples with NaOH, $Al(NO_3)_3$, and Na_2SiO_3, but the proportion of Q^1 was low compared to $Q^2(n\text{Al})$ sites, indicating long chain lengths.

Garcia-Lodeiro [34] studied C-S-H synthesized with a target Ca/Si ratio of 1.9 and the effect of the simultaneous addition of aluminum nitrate and sodium hydroxide. The addition of aluminum and sodium caused a shift in the ^{29}Si NMR spectra from predominantly Q^1 to Q^2. Small amounts of Q^3 were present and it was inferred that this arose from silica gel due to carbonation of the samples. The possibility of sample carbonation make it difficult to draw conclusions on the effect of the simultaneous addition of aluminum and sodium on the molecular structure of C-S-H.

Andersen et al. [24] hydrated white portland cement in 0.3 M and 0.5 M solutions of $NaAlO_2$ and characterized the pastes with ^{29}Si and ^{27}Al NMR. A steady increase in $Q^2(1Al)$ intensity was detected with time and the intensity was greater with higher concentrations of $NaAlO_2$. The MCL was consistently higher for higher concentrations of $NaAlO_2$ and increased with time. After 2 years, the MCL of the cement hydrated in water, 0.3 M $NaAlO_2$, and 0.5 M $NaAlO_2$ were 3.85, 5.17, and 6.09, respectively. A method of calculating the mean chain length of "pure" SiO_4 tetrahedra was suggested as:

$$\mathrm{MCL_{Si}} = \frac{Q^1 + Q^2 + Q^2(1Al)}{\frac{1}{2}(Q^1 + Q^2(1Al))} \tag{2}$$

The $\mathrm{MCL_{Si}}$ were 3.13, 3.55, and 3.56 for cement hydrated in water, 0.3 M $NaAlO_2$, and 0.5 M $NaAlO_2$, respectively. Since the $\mathrm{MCL_{Si}}$ values are lower than the MCL values the authors concluded that the alumina tetrahedra are linking existing silicate chains.

Manzano et al. [29] used molecular dynamics to study aluminum in C-S-H and the resulting molecular structure. Linear structures (Q^2) were always found to be dominant, but as the Al/Si ratio increased the proportion of Q^3+Q^4 increased for various Ca/Si ratios. Similarly, as Al/Si increased the MCL increased. Simulations showed good agreement with experimental MCL data.

2.5 CARBONATION OF C-S-H

Carbonation of C-S-H is an issue that has plagued many characterization studies of synthesized C-S-H. Four phases of calcium carbonate exist with increasing stability, amorphous calcium carbonate, vaterite, aragonite, and calcite [35]. Carbonated C-S-H becomes highly porous with a low Ca/Si ratio, upon further reaction, hydrous silica is formed with a Q^3 and Q^4 structure [36].

Garcia-Lodeiro et al. [33] noted that when synthesized C-S-H was mixed with a solution of 8 M NaOH, calcite peaks appeared in the XRD pattern and the ^{29}Si spectrum indicated a large increase in MCL, from 3.05 to 9.44. Additionally, Q^3 and Q^4 sites were present, which are associated with the formation of silica gel. The authors stated that the addition of highly concentrated alkali solution caused polymerization of the silicate structure.

Groves et al. [37] studied hydrated C_3S pastes in regard to carbonation in a CO_2 environment. By XRD, calcite was the most dominant polymorph of calcium carbonate, with some vaterite. From ^{29}Si NMR, as the carbonation time increased the predominant peak shifted from Q^1 to Q^2 with some Q^3 and Q^4 becoming apparent after 4 hours and abundant after 8 hours. When the paste was carbonated for 16 hours a large amorphous hump was observed in the XRD pattern around 20° 2θ indicating silica gel. It was stated that the calcium hydroxide present in the C_3S paste initially carbonated more quickly than C-S-H, but the rate decreased after approximately half of the CH had reacted. C-S-H continued to carbonate through this period.

Garcia-Loderio [38] studied synthesized C-S-H with Ca/Si of 1.9 mixed with different amounts of an 8M solution of sodium hydroxide to achieve specific Na_2O/SiO_2 ratios. FTIR analysis indicated that calcium carbonate was present in all samples. When NaOH was added, the CH band that was present in the control sample disappeared and the intensity of the calcite bands increased. It is expected that the addition of NaOH would encourage the precipitation of CH due to the common ion effect. The authors proposed that Ca^{2+} is being redistributed on the surface of C-S-H or N-S-H (sodium silicate hydrate) to satisfy surface charges and that sodium silicate gels are formed or the degree of silicate polymerization in C-S-H is increased by the addition of NaOH. As the amount of NaOH increased, bands in the FTIR spectra indicated that silica gel may be forming. The authors also stated that carbonation can cause polymerization and silica gel formation and cannot be ruled out for the development of these characteristics. Other literature indicates that these characteristics are typical of carbonation of C-S-H [37].

3. EXPERIMENTAL PROCEDURES

3.1 SYNTHESES

C-S-H and C-A-S-H were synthesized by two methods using different sources of calcium and silicon. The double decomposition method was chosen for its fast reaction rate while the direct reaction was chosen for the lack of extraneous ions in the reaction. Both methods have been used frequently for C-S-H synthesis [2, 4, 5, 20, 34].

The sample names follow the formatting presented here. "MATERIAL"_"SYNTHESIS METHOD"_"Ca/Si OR Ca/(Si+Al)""IDENTIFIER," where the "MATERIAL" is CSH or CASH, "SYNTHESIS METHOD" is DD, for double decomposition, or DR, for direct reaction, "Ca/Si OR Ca/(Si+Al)" is a numeral, and "IDENTIFIER" is an alphabetic character used to differentiate similar samples, their meaning is stated in the text.

3.1.1 DOUBLE DECOMPOSITION

C-S-H was synthesized by double decomposition of solutions of sodium silicate and calcium nitrate. Nanopure water was boiled to remove dissolved CO_2 and subsequently placed under vacuum and rapidly cooled to room temperature using an ice water slurry. Quantities of sodium silicate ($Na_2SiO_3 \cdot 9H_2O$ Fisher Scientific) and calcium nitrate ($Ca(NO_3) \cdot 4H_2O$ Fisher Scientific), shown in Table 1, where added to 125 mL and 75 mL of water, respectively. The calcium nitrate solution was added drop by drop to the continuously stirred sodium silicate solution under continuous nitrogen flow to avoid exposure to CO_2. A precipitate formed immediately. The 500 mL HDPE bottle containing the solution and precipitate was backfilled with nitrogen, capped, and allowed to stir for one hour. The precipitate was then filtered using a Buchner funnel and Whatman Grade 50 filter paper (2.7 µm). Samples CSH_DD_1.0A, CSH_DD_1.3A, and CSH_DD_1.5A were rinsed with 100 mL of degassed Nanopure water and 200 mL of ethanol. Samples CSH_DD_1.1B, CSH_DD_1.3B, CSH_DD_0.8B, CSH_DD_1.5B, and CSH_DD_0.9B were rinsed with 2 liters of degassed Nanopure water.

C-A-S-H was synthesized by taking half of the C-S-H synthesized by the above method and adding it to 140 mL of a solution of sodium aluminate backfilled with nitrogen and stirring for 24 hours. Additionally, CASH_DD_2.2H and CASH_DD_2.2L were synthesized in a similar method with high, “H”, and low, “L”, aluminum amounts. The precipitate was then filtered using a Buchner funnel and Whatman Grade 50 filter paper (2.7 µm) and rinsed with 2 liters of degassed Nanopure water. Table 1 shows the proportions of each reagent used in synthesis.

Table 1: Double decomposition synthesis reagents.

Sample	$Na_2SiO_3{\cdot}9H_2O$ (grams)	$Ca(NO_3){\cdot}4H_2O$ (grams)	$NaAlO_2$ (grams)
CSH_DD_1.0A	19.04	11.67	-
CSH_DD_1.3A	19.04	15.16	-
CSH_DD_1.5A	19.04	17.50	-
CSH_DD_0.8B	19.04	12.20	-
CSH_DD_0.9B	19.04	14.20	-
CSH_DD_1.1B	19.04	17.50	-
CSH_DD_1.3B	19.04	20.60	-
CSH_DD_1.5B	19.04	23.70	-
CASH_DD_0.8B	19.04	12.20	5.00
CASH_DD_0.9B	19.04	14.20	5.00
CASH_DD_1.1B	19.04	17.50	5.00
CASH_DD_1.3B	19.04	20.60	5.00
CASH_DD_1.5B	19.04	23.70	5.00
CASH_DD_2.2H	19.04	26.12	4.40
CASH_DD_2.2L	19.04	26.12	2.20

3.1.2 DIRECT REACTION

C-S-H was synthesized by the direct reaction of calcium oxide and fumed silica in water. Calcium oxide was obtained by calcining $CaCO_3$ (Sigma-Aldrich) at 900°C for 24 hours and storing in a vacuum desiccator. Fumed silica (SiO_2, Sigma-Aldrich) was placed in an oven at 105°C for at least three hours to remove water. Nanopure water was boiled to remove dissolved CO_2 and subsequently placed under vacuum and rapidly cooled to room temperature using an ice water slurry. Quantities of calcium oxide (CaO) and fumed silica, shown in Table 2, were dry mixed in 500 mL HDPE bottles. Four hundred mL of degassed Nanopure water was added to the bottles, backfilled with nitrogen, shaken, and allowed to stir for one week. The precipitate was then filtered using a Buchner funnel and Whatman Grade 50 filter paper (2.7 µm) and rinsed in two batches with 100 mL of degassed Nanopure water and 200 mL of ethanol for each batch.

C-A-S-H was synthesized similarly to the C-S-H. Nanopure water was boiled to remove dissolved CO_2 and subsequently placed under vacuum and rapidly cooled to room temperature using an ice water slurry. For samples CASH_DR_1.0A, CASH_DR_1.3A, CASH_DR_1.5A, CASH_DR_1.0B, CASH_DR_1.3B, and CASH_DR_1.5B quantities of calcium oxide (CaO), fumed silica (SiO_2), and aluminum nitrate ($Al(NO_3)_3{\cdot}9H_2O$ Sigma-Aldrich), shown in Table 2, were dry mixed in 500 mL HDPE. Four hundred mL of degassed Nanopure water was added to the bottles, backfilled with nitrogen, shaken, and allowed to stir for one week. For samples

CASH_DR_0.9H, CASH_DR_1.1H, CASH_DR_1.3H, CASH_DR_1.5H, CASH_DR_1.7H, CASH_DR_0.9L, CASH_DR_1.1L, CASH_DR_1.3L, CASH_DR_1.5L, and CASH_DR_1.7L quantities of calcium oxide (CaO) and fumed silica (SiO_2), shown in Table 2, were dry mixed in a 500 mL HDPE bottle. Four hundred mL of degassed Nanopure water was added to the bottles, backfilled with nitrogen, shaken, and allowed to stir for one week. Then, the precipitate was split in two and each was placed in a 140 mL of a solution of aluminum nitrate, backfilled with nitrogen, and allowed to stir for 24 hours. The precipitate was then filtered using a Buchner funnel and Whatman Grade 50 filter paper (2.7 µm) and rinsed in two batches with 100 mL of degassed Nanopure water and 200 mL of ethanol for each batch. Sample CASH_DR_1.0C was synthesized by taking 3 grams of CSH_DR_1.0A and adding it to 400 mL of aluminum nitrate solution, backfilled with nitrogen, and stirred for 24 hours. The precipitate was then filtered using a Buchner funnel and Whatman Grade 50 filter paper (2.7 µm) and rinsed in two batches with 100 mL of degassed Nanopure water and 200 mL of ethanol for each batch.

The sample names for direct reaction synthesis follow the formatting listed below. Sample names ending in “A” have a nominal Ca/Si ratio equal to the number preceding it while sample names ending in ”B” have a nominal Ca/(Si+Al) ratio equal to the number preceding it. Sample names ending in “H” have a nominal Al/Si=1/6 and sample names ending in “L” have a nominal Al/Si=1/12. The sample name ending in “C” has a nominal Ca/Si ratio of 1.0.

Table 2: Direct reaction synthesis reagents.

Sample	CaO (grams)	SiO_2 (grams)	$Al(NO_3)_3 \cdot 9H_2O$ (grams)
CSH_DR_1.0A	14.48	15.52	0.00
CSH_DR_1.3A	16.45	13.56	0.00
CSH_DR_1.5A	17.50	12.50	0.00
CASH_DR_1.0C	14.48	15.52	9.38
CASH_DR_1.0A	9.97	8.90	11.14
CASH_DR_1.3A	11.77	8.09	10.14
CASH_DR_1.5A	12.82	7.63	9.56
CASH_DR_1.0B	14.48	15.52	19.38
CASH_DR_1.3B	16.45	13.56	16.93
CASH_DR_1.5B	17.50	12.50	15.61
CASH_DR_0.9H	9.13	10.87	3.50
CASH_DR_1.1H	10.13	9.87	3.16
CASH_DR_1.3H	10.96	9.04	2.90
CASH_DR_1.5H	11.67	8.33	2.67
CASH_DR_1.7H	12.27	7.73	2.48
CASH_DR_0.9L	9.13	10.87	1.75
CASH_DR_1.1L	10.13	9.87	1.58
CASH_DR_1.3L	10.96	9.04	1.45
CASH_DR_1.5L	11.67	8.33	1.33
CASH_DR_1.7L	12.27	7.73	1.24

3.1.3 CARBONATION TREATMENT

C-S-H was treated with four different solutions to examine the effect of alkali and hydroxide ions on carbonation. Two grams of dried CSH_DR_1.3A with a nominal Ca/Si ratio of 1.3 were placed in Nanopure water, 0.1 M solution of NaOH, 0.1 M solution of KOH, and 0.1 M solution of $NaNO_3$ and allowed to stir for one hour in open air. The water used in these solutions was not boiled and contained dissolved CO_2. The pH of the solutions were 6.32, 12.83, 12.88, and 6.44, respectively read by a pH meter. The solutions were filtered using a Buchner funnel and Whatman Grade 50 filter paper (2.7 µm). The solids were dried and analyzed with XRD, TGA, and ^{29}Si NMR.

3.1.4 DRYING PROCEDURE

After filtering and rinsing, the C-S-H and C-A-S-H were dried for characterization. The samples were placed in a vacuum oven set at 40°C at -18 inches of Hg from atmospheric pressure. Drying below 50°C does not cause significant changes in the crystal structure of C-S-H [39]. The samples were dried to constant mass and stored in a vacuum desiccator until characterization. Samples CASH_DD_2.2H and CASH_DD_2.2L were allowed to dry to constant mass in a vacuum desiccator at room temperature. These samples were dried at room temperature due to a malfunction of the vacuum oven.

3.2 X-RAY DIFFRACTION

X-Ray diffraction (XRD) was performed to identify crystalline phases and observe changes in the unit cell dimensions in the C-(A)-S-H. Samples were ground using a mortar and pestle and passed through a #200 sieve. The sample passing the #200 sieve was packed into a low-background sample holder. A Siemens-Bruker D5000 powder diffractometer with Cu-Kα radiation in the theta/theta configuration was used for measurements. The diffractometer was operated at 40 kV and 30 mA. Measurements were made from 2° to 60° 2θ at a rate of 1°/min with a step size of 0.02° 2θ. The diffraction pattern was analyzed using MDI Jade. Peaks were indexed using PDF cards from Jade and literature.

3.3 NUCLEAR MAGNETIC RESONANCE

Solid state magic angle spinning nuclear magnetic resonance was performed on sampled to characterize the local atomic structure of ^{29}Si and ^{27}Al nuclei.

3.3.1 ^{29}Si NMR

The ^{29}Si NMR measurements were made using a Varian Unity Inova 300 spectrometer (7.05 T) operating at 59.6 MHz. A 4-mm Chemagnetic probe was used, spinning at 10 kHz. Chemical shifts were measured relative to tetramethylsilane (TMS). The direct polarization experiment used a $\pi/2$ flip angle (2.45 μs pulse width) with ^{1}H decoupling and a recycle delay of 60 seconds. The acquisition time was 20.48 ms. In total, 1536 scans were made for most samples. Samples CASH_DR_1.0A and CASH_DR_1.0B were run with 3725 scans due to low signal intensity when run with 1536 scans.

3.3.2 ^{27}Al NMR

^{27}Al NMR measurements were made using a Varian VNMRS 750WB (17.6 T) operating at 195 MHz, a Varian VNS 750NB (17.6 T) operating at 195 MHz, and a Varian Unity Inova 300 spectrometer (7.05 T) operating at 78.2 MHz. A 4-mm T_3 Triple Res HXY Solids probe was used for the 17.6 T spectrometers, spinning at 15 kHz, and a 4-mm Chemagnetic probe was used for the 7.05 T spectrometer, spinning at 12 kHz. Chemical shifts were measured relative to aluminum nitrate ($Al(NO_3)_3$). The direct polarization experiment used a $\pi/12$ flip angle (1.5 μs pulse width) and a recycle delay of 5 seconds. A small flip angle was used to ensure that the response was in the linear regime, and thus quantitative, meaning that deconvolution of peaks yields accurate comparisons of different chemical environments [40]. The acquisition time was 20 ms. In total, 256 scans were made for each sample.

3.3.3 DECONVOLUTION

Analysis and deconvolution of NMR spectra were performed using MestreLab Research Mnova NMR for MAS-NMR experiments. Spectra were phase and baseline corrected. Exponential apodization was applied based on the line width of the spectra. Deconvolution is a method of separating a complex curve into individual curves. The following parameters were adjusted to achieve a good fit: chemical shift, peak height, peak width, and Lorentzian/Gaussian (l/g) line shape. The areas of each individual curve are quantitative with respect to the amount of nuclei in that specific chemical environment. Equation 3 was used to aid in deconvolution:

$$\frac{Bridging\ tetrahedra}{Pairing\ tetrahedra} = \frac{\frac{1}{2}Q^2(1Al) + {Q_B}^2}{Q^2(1Al) + {Q_P}^2} \approx \frac{1}{2} \quad (3)$$

where ${Q_B}^2$ and ${Q_P}^2$ are silicon nuclei in the bridging and pairing position, respectively. This equation assumes a dreierketten silicate structure [10] and that aluminum is only occurring in the bridging tetrahedra position [2, 21, 28].

3.4 X-RAY FLUORESCENCE

X-Ray fluorescence was provided by Binh Phan and Tom Wilson at the central laboratory at the CalPortland Company.

3.5 THERMOGRAVIMETRIC ANALYSIS

Thermogravimetric analysis (TGA) was performed on samples to examine the thermal decomposition, with specific interest in the decomposition of $CaCO_3$ in the sample due to carbonation. A TA Instruments Q50 TGA was used for measurements. Samples were run at a heating rate of 20°C/min up to 1000°C in a nitrogen environment with a flow rate of 60 mL/min. Alumina crucibles were used and the sample weight was approximately 5 mg. Data were processed using TA Instruments Universal Analysis 2000.

4. RESULTS

The calcium silicate hydrate (C-S-H) and calcium aluminosilicate hydrate (C-A-S-H) were characterized in order to understand the structure and composition of the synthesized materials. The mean chain length and presence of crosslinking between chains was of specific interest. Both materials are susceptible to changes in their structure by interaction with atmospheric carbon dioxide and careful consideration was given to these changes and to the presence of calcium carbonate ($CaCO_3$). A variety of characterization techniques were used to probe the materials, including XRD, ^{29}Si and ^{27}Al NMR, XRF, and TGA. Results from these experiments are presented below.

4.1 XRD

4.1.1 C-S-H SYNTHESIZED BY DOUBLE DECOMPOSITION

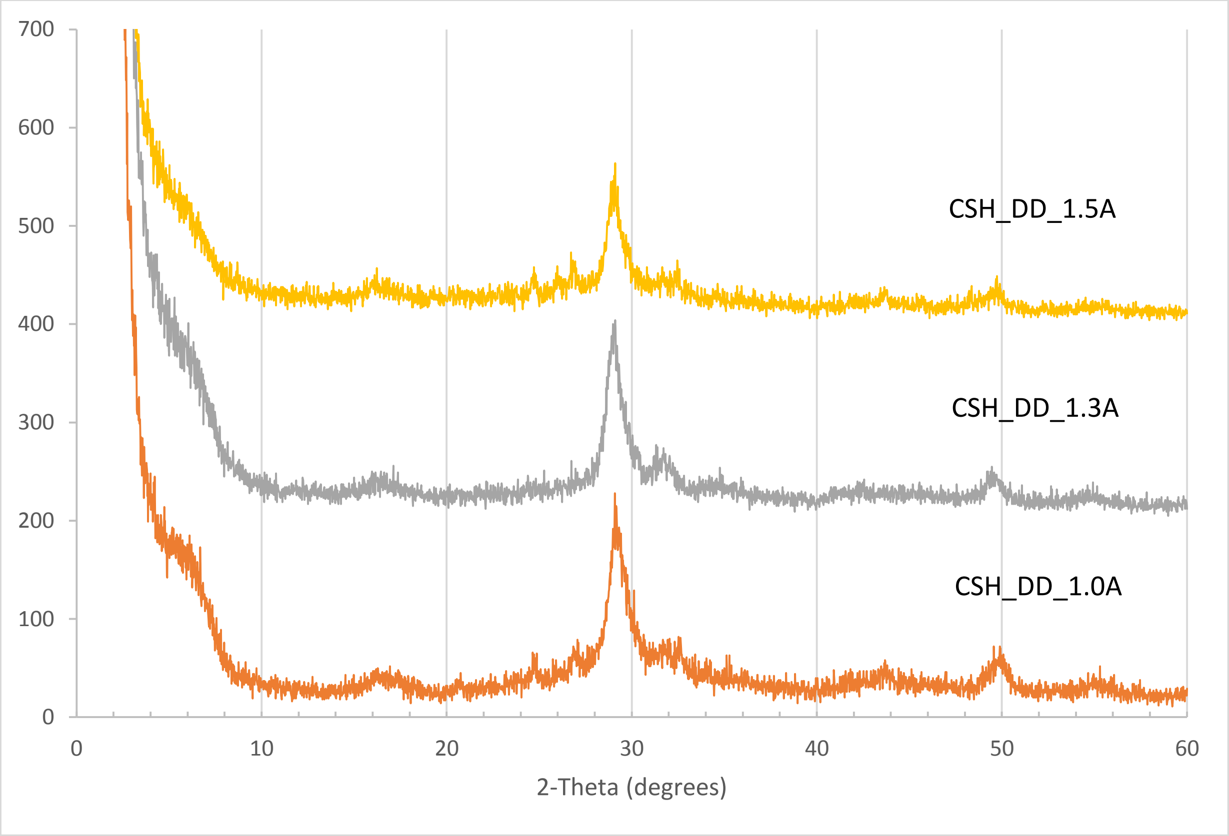

Figure 3: XRD pattern of CSH_DD_1.5A, CSH_DD_1.3A, and CSH_DD_1.0A.

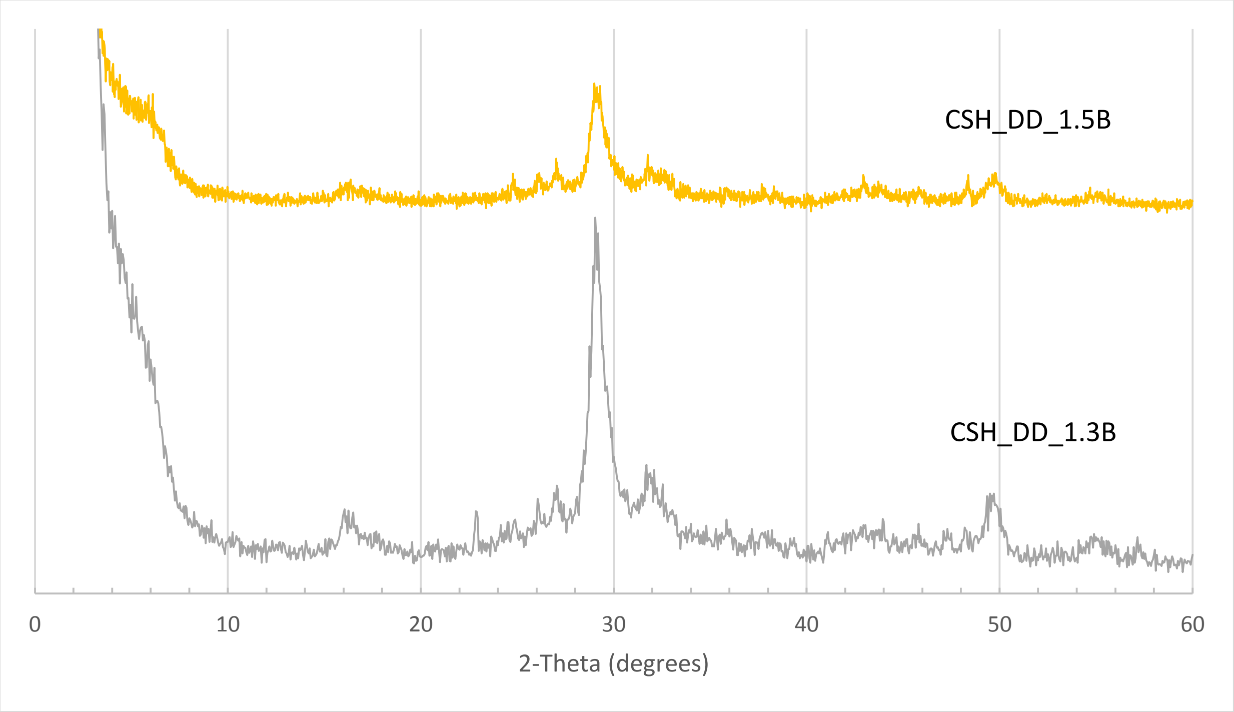

Figure 4: XRD pattern of CSH_DD_1.5B and CSH_DD_1.3B.

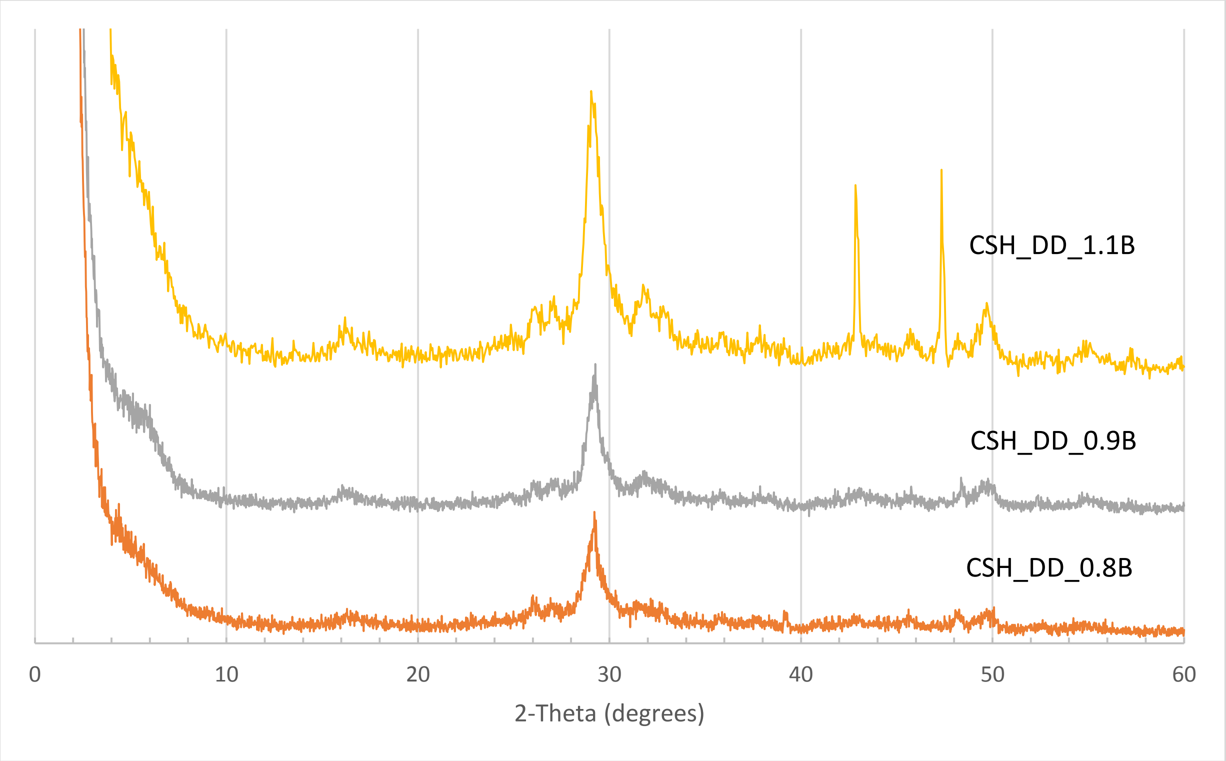

Figure 5: XRD pattern of CSH_DD_1.1B, CSH_DD_0.9B, and CSH_DD_0.8B.

The XRD patterns for C-S-H synthesized by double decomposition, presented in Figures 3-5, all have intense peaks centered around 29.2° (2θ), which is the dominant peak in both C-S-H and calcite. Other peaks indicating that C-S-H is present are at 16.9°, 32.0°, 42.7°, 49.8°, and 55.3°. CSH_DD_1.3A, CSH_DD_1.0A, CSH_DD_1.5B, CSH_DD_1.3B, and CSH_DD_0.9B have basal peaks ([00*l*] reflection). In addition to C-S-H, samples CSH_DD_1.0A, CSH_DD_1.3B, and CSH_DD_1.1B show amorphous humps in the 25-35° range, indicating silica gel.

CSH_DD_1.5A and CSH_DD_1.5B have calcite (29.5°, 36.1°, 48.6°), aragonite (26.1°, 27.1°,45.8°), and vaterite (24.8°, 26.8°, 32.8°) peaks. CSH_DD_1.3B, CSH_DD_1.1B, and CSH_DD_0.9B have calcite (29.5°, 23.0°, 43.0°, 47.4°, 57.3°) and vaterite (24.9°, 27.0°, 32.8°, 50.0°) peaks. The peaks in CSH_DD_1.1B at 43.0° and 47.4° are very intense, the reason for this is unknown. CSH_DD_0.8B has calcite (23.0°, 29.5°, 35.9°, 39.3°) and aragonite (26.1°, 27.0°, 32.8°, 48.4°) peaks. CSH_DD_1.0A has only vaterite (20.9°, 24.8°, 27.0°, 32.8°, 50.0°) as a $CaCO_3$ polymorph. CSH_DD_1.3A did not show any $CaCO_3$ polymorph peaks.

4.1.2 C-S-H SYNTHESIZED BY DIRECT REACTION

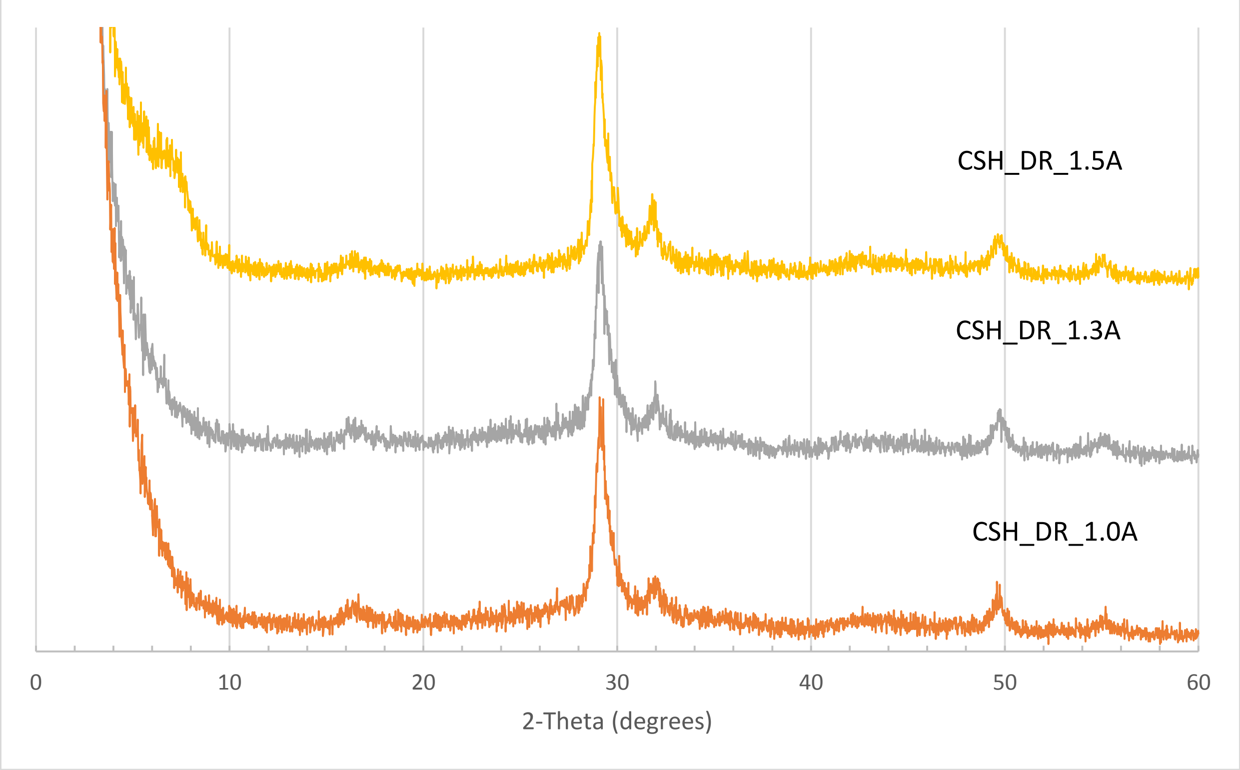

Figure 6: XRD pattern of CSH_DR_1.5A, CSH_DR_1.3A, and CSH_DR_1.0A.

The XRD patterns for C-S-H synthesized by direct reaction, presented in Figure 6, all have intense peaks centered around 29.2° (2θ), which is the dominant peak in both C-S-H and calcite. Other peaks indicating that C-S-H is present are at 16.9°, 32.0°, 42.7°, 49.8°, and 55.3°. A basal peak ([00*l*] reflection) is seen in CSH_DR_1.5A. None of these samples exhibited $CaCO_3$ polymorphs.

4.1.3 C-A-S-H SYNTHESIZED BY DOUBLE DECOMPOSITION

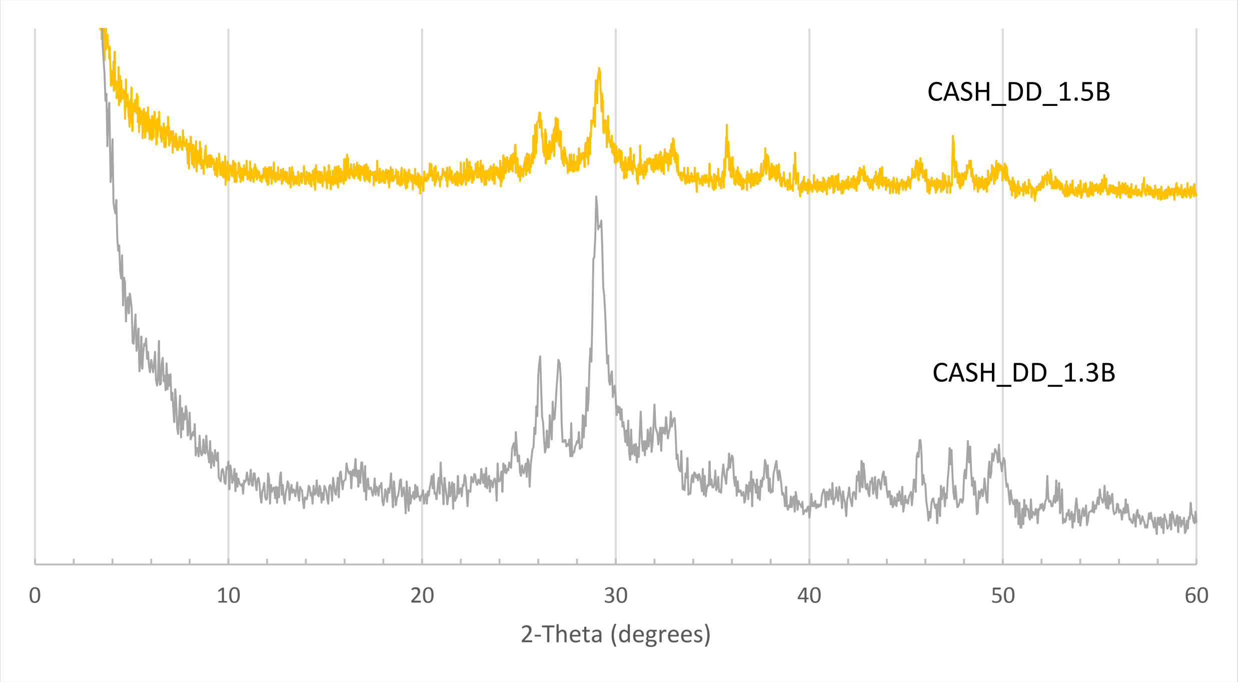

Figure 7: XRD pattern of CASH_DD_1.5B and CASH_DD_1.3B.

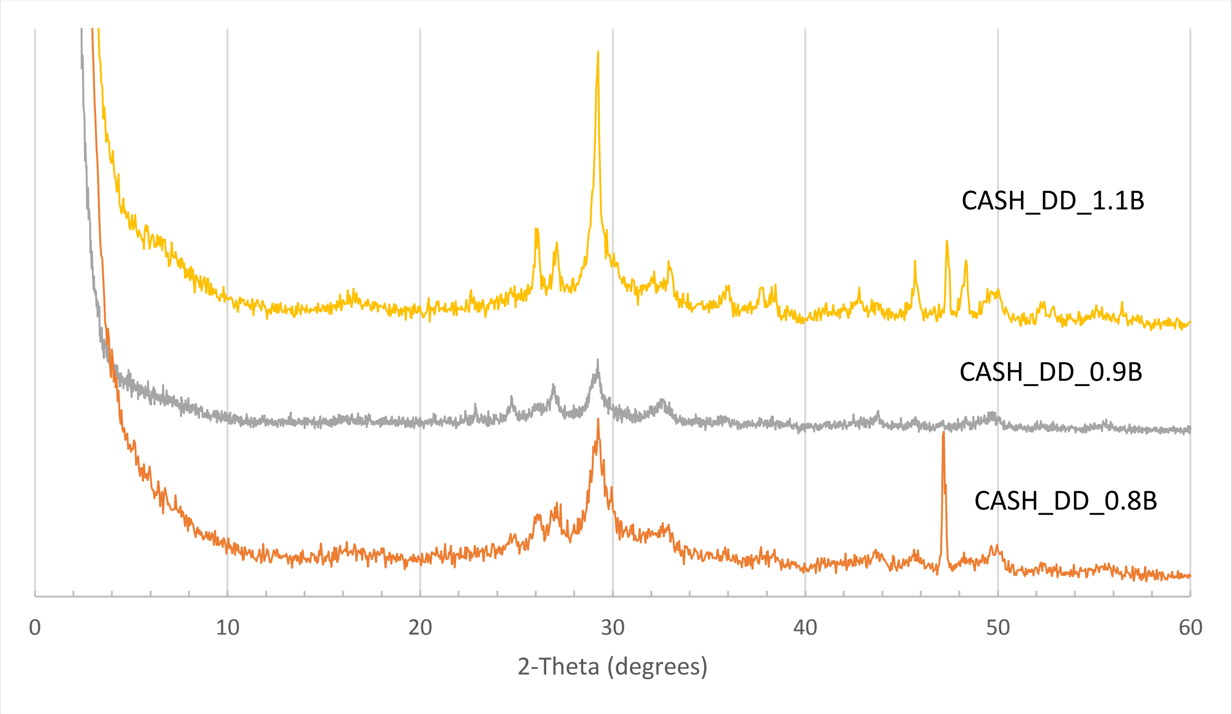

Figure 8: XRD pattern of CASH_DD_1.1B, CASH_DD_0.9B, and CASH_DD0.8B.

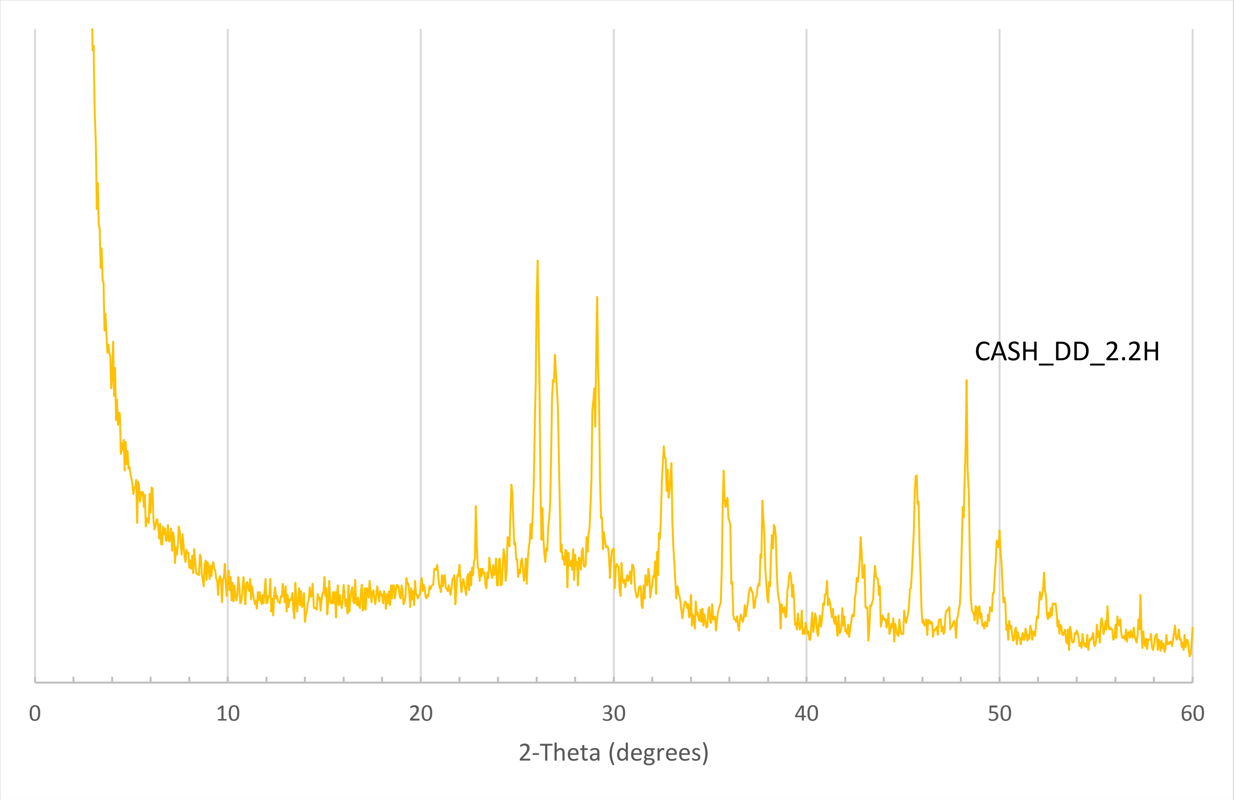

Figure 9: XRD pattern of CASH_DD_2.2H.

The XRD patterns for C-A-S-H synthesized by double decomposition, presented in Figures 7-9, all have intense peaks centered around 29.2° (2θ), which is the dominant peak in both C-S-H and calcite. Other peaks indicating that C-S-H is present are at 16.9°, 32.0°, 42.7°, 49.8°, and 55.3°. CASH_DD_1.1B and CASH_DD_1.3B have basal peaks ([00*l*] reflection). CASH_DD_1.3B, CASH_DD_1.1B, CASH_DD_0.8B, and CASH_DD_2.2H have amorphous humps in the 22-30° range, which indicates silica gel with alumina.

CASH_DD_1.5B and CASH_DD_1.3B have calcite (23.1°, 29.5°, 35.6°, 47.4°), aragonite (26.1°, 27.0°, 37.7°, 45.8°), and vaterite (24.8°, 27.0°, 50.0°, 32.7°) peaks. CASH_DD_1.1B has calcite (29.5°, 35.9°, 47.3°, 48.2°) and aragonite (26.1°, 27.0°, 37.7°, 45.8°) peaks. CASH_DD_0.9B has calcite (23.1°, 29.5°, 36.0°) and vaterite (20.9°, 24.7°, 27.0°, 32.6°) peaks. CASH_DD_0.8B has vaterite (20.9°, 24.9°, 27.0°, 32.7°) and aragonite (26.1°, 27.0°, 37.9°, 38.4°, 45.7°) peaks. The strong reflection at 47.1° in CASH_DD_0.8B is could either be a calcite or calcium hydroxide peak, but no other peaks from either phase were observed.

CASH_DD_2.2H appears to be predominately calcium carbonate as evidenced by the strong reflections of calcite, aragonite and vaterite and the large amorphous hump. Very little, or no, C-S-H remains in this sample.

4.1.4 C-A-S-H SYNTHESIZED BY DIRECT REACTION

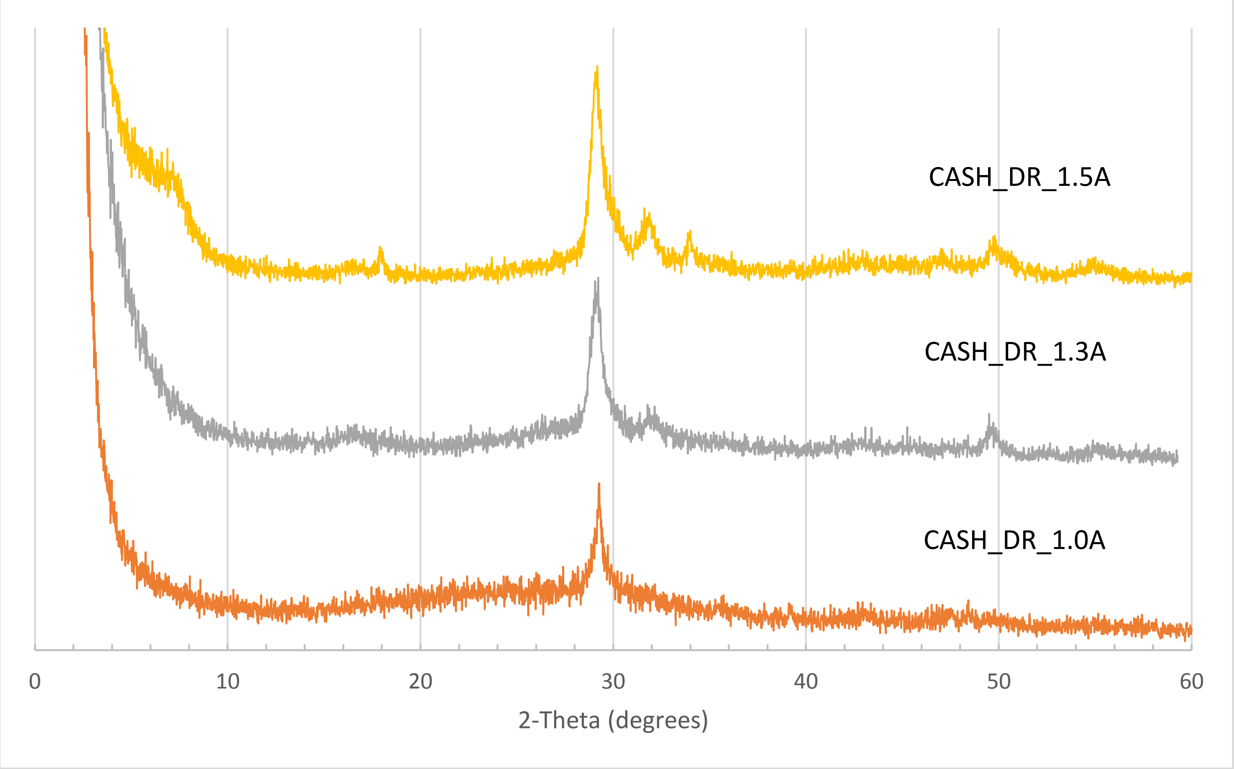

Figure 10: XRD pattern of CASH_DR_1.5A, CASH_DR_1.3A, and CASH_DR_1.0A.

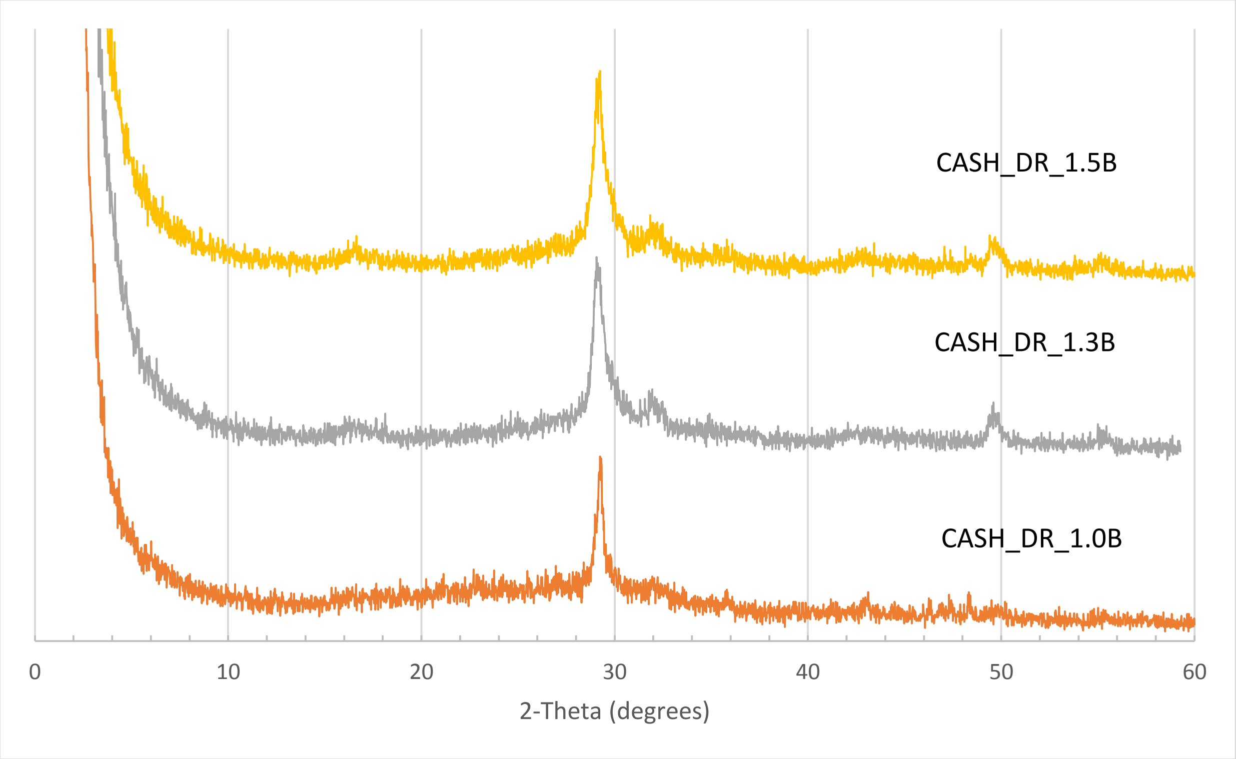

Figure 11: XRD pattern of CASH_DR_1.5B, CASH_DR_1.3B, CASH_DR_1.0B.

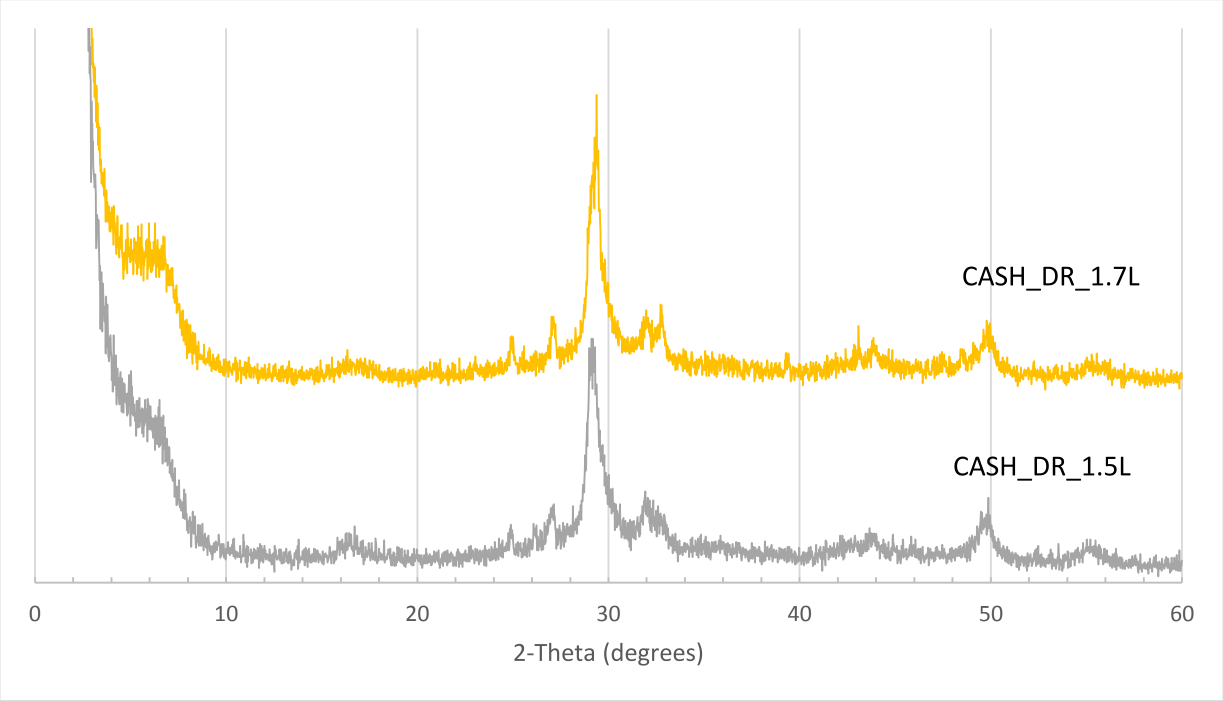

Figure 12: XRD pattern of CASH_DR_1.7L and CASH_DR_1.5L.

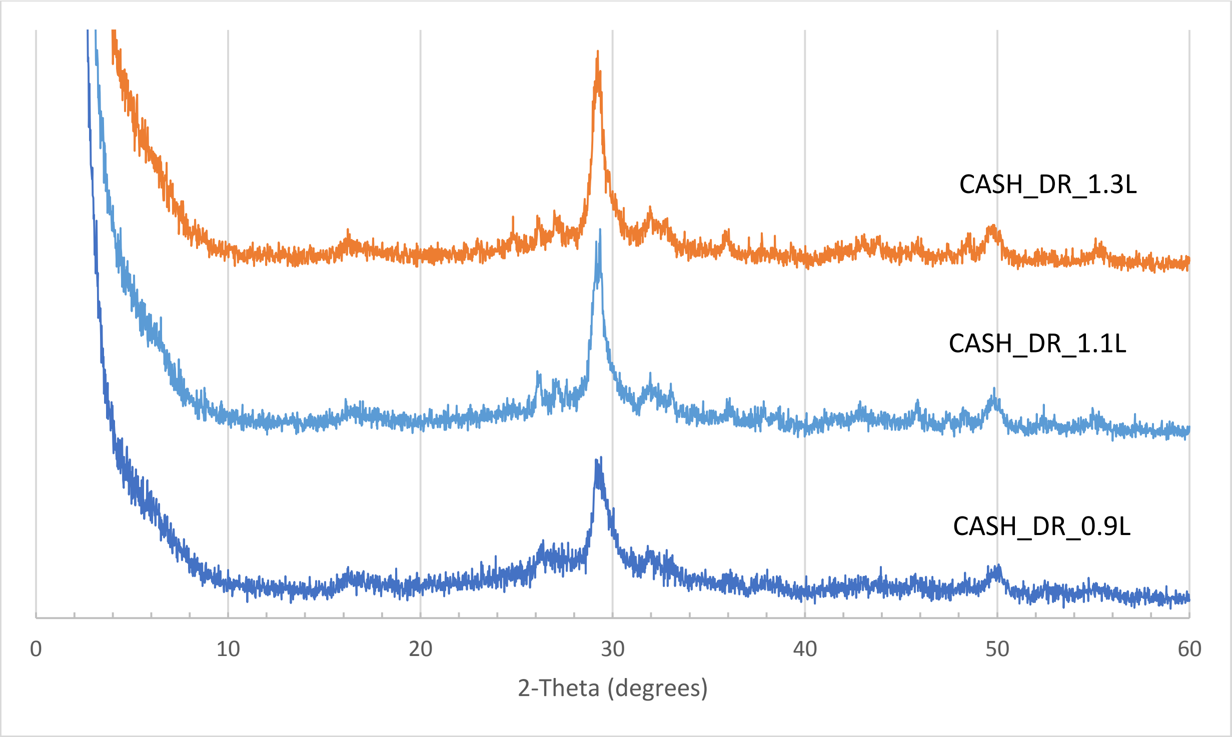

Figure 13: XRD pattern of CASH_DR_1.3L, CASH_DR_1.1L, and CASH_DR_0.9L.

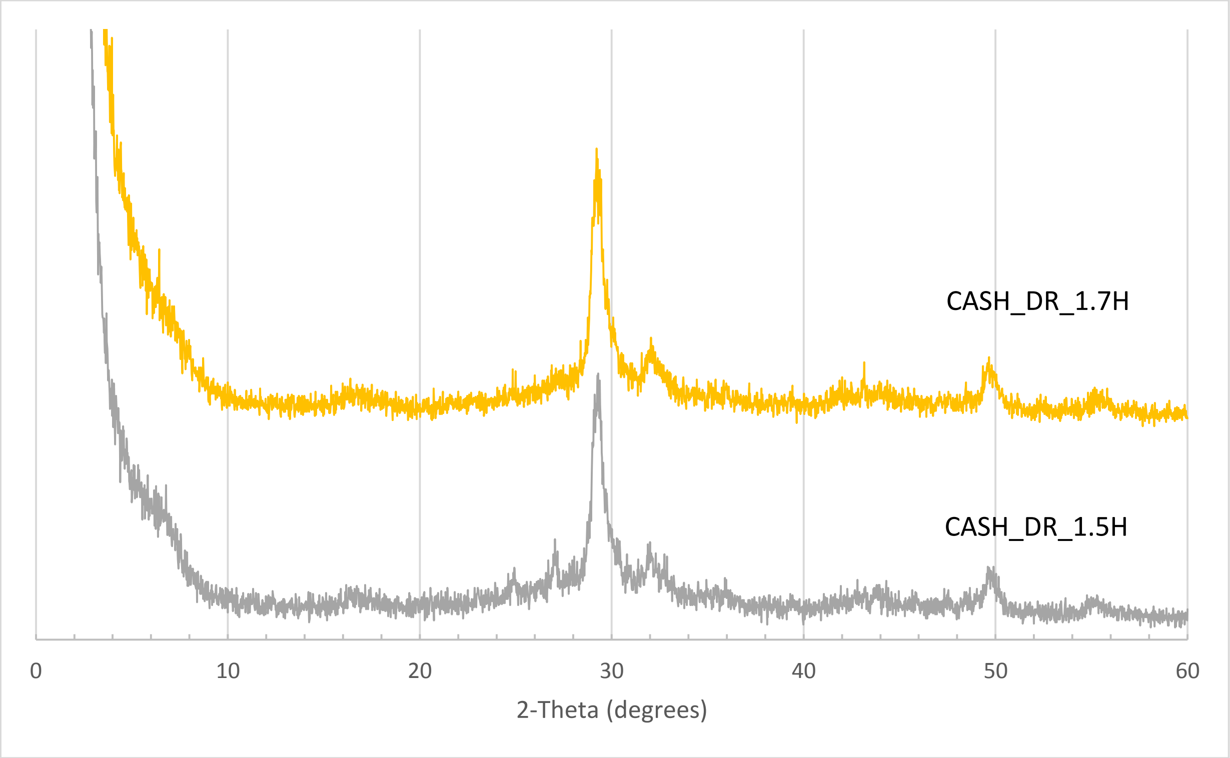

Figure 14: XRD pattern of CASH_DR_1.7H and CASH_DR_1.5H.

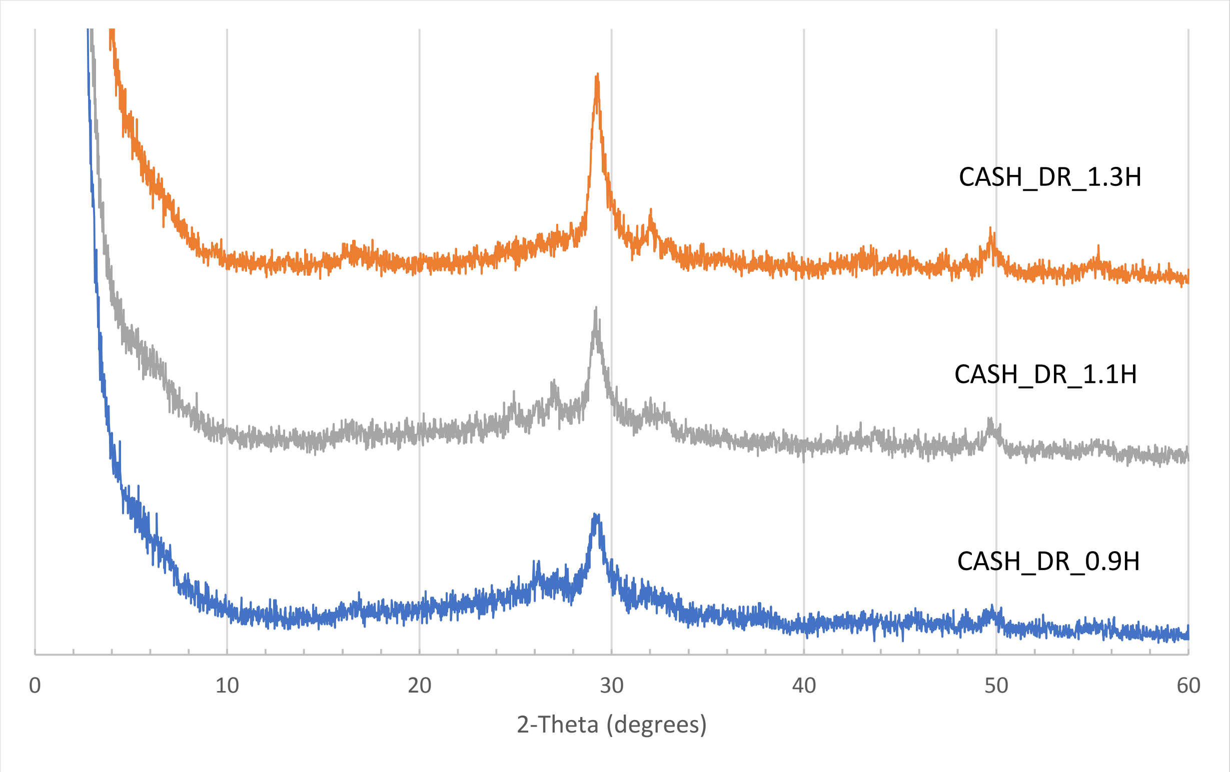

Figure 15: XRD pattern of CASH_DR_1.3H, CASH_DR_1.1H, and CASH_DR_0.9H.

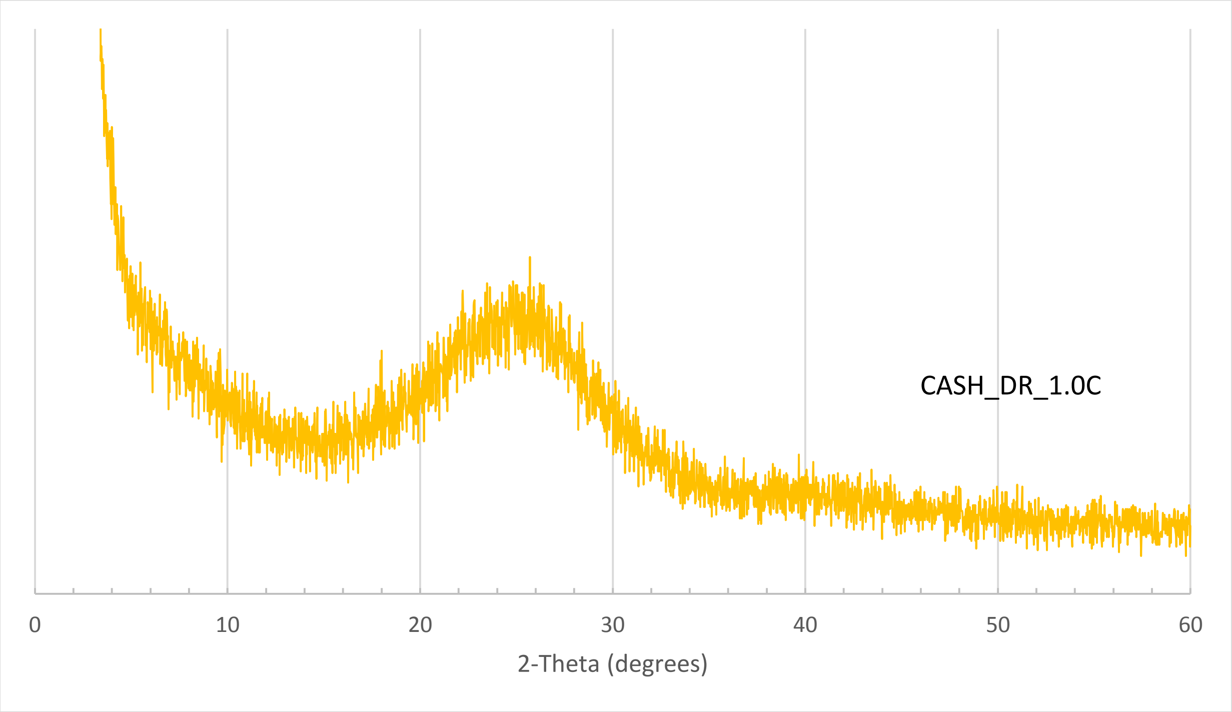

Figure 16: XRD pattern of CASH_DR_1.0C.

The XRD patterns for C-A-S-H synthesized by direct reaction, presented in Figures 10-16, all have intense peaks centered around 29.2° (2θ), which is the dominant peak in both C-S-H and calcite, except for CASH_DR_1.0C. CASH_DR_1.0C has a large amorphous hump from 15° to 34° and no other reflections. This sample is most likely entirely an alumina/silica gel. Other peaks indicating that C-S-H is present are at 16.9°, 32.0°, 42.7°, 49.8°, and 55.3°. Samples CASH_DR_1.0A, CASH_DR_1.0B, CASH_DR_0.9L, CASH_DR_1.5H, CASH_DR_1.1H, and CASH_DR_0.9H have amorphous humps in the 22-30° range, which indicates alumina/silica gel. Samples CASH_DR_1.5A, CASH_DR_1.7L, CASH_DR_1.5L, and CASH_DR_1.5H have basal peaks ([00*l*] reflection).

CASH_DR_1.3A, CASH_DR_1.3B, and CASH_DR_1.7H contain no $CaCO_3$ polymorph peaks. CASH_DR_1.5A contains three low, broad peaks that can be assigned to calcium hydroxide; no $CaCO_3$ polymorphs are present. CASH_DR_1.3H has very low intensity calcite (29.5°, 47.5°, 48.6°) peaks and the quantity of calcite is low. CASH_DR_1.0A and CASH_DR_1.0B do not have enough C-S-H peaks to assign this phase, only calcite (29.5°, 35.8°, 43.2°, 48.3°) peaks are present. CASH_DR_1.5B contains only calcite (22.9°, 29.5°, 36.0°, 48.5°) as a $CaCO_3$ polymorph. CASH_DR_1.7L and CASH_DR_1.5H contain calcite (23.0°, 29.5°, 39.3°, 47.6°, 48.6°) and vaterite (24.8°, 27.0°, 32.6°, 50.0°) peaks. CASH_DR_1.5L exhibits aragonite (26.1°, 27.3°, 32.8°, 50.0°) and vaterite (24.9°, 27.3°, 32.8°, 50.0°) peaks. CASH_DR_1.1H has only vaterite (24.9°, 27.0°, 32.9°, 50.0°) peaks. CASH_DR_0.9L, CASH_DR_1.1L, and CASH_DR_0.9H have calcite

(29.5°, 36.1°, 47.6°, 48.4°) and aragonite (26.1°, 27.0°, 37.8°, 50.0°) peaks. CASH_DR_1.3L contains calcite (23.1°, 29.5°, 35.9°, 48.6°), aragonite (26.2°, 27.0°, 32.8°, 38.3°, 45.4°), and vaterite (24.9°, 27.0°, 32.8°, 50.0°).

4.1.5 CARBONATION TREATMENT OF C-S-H

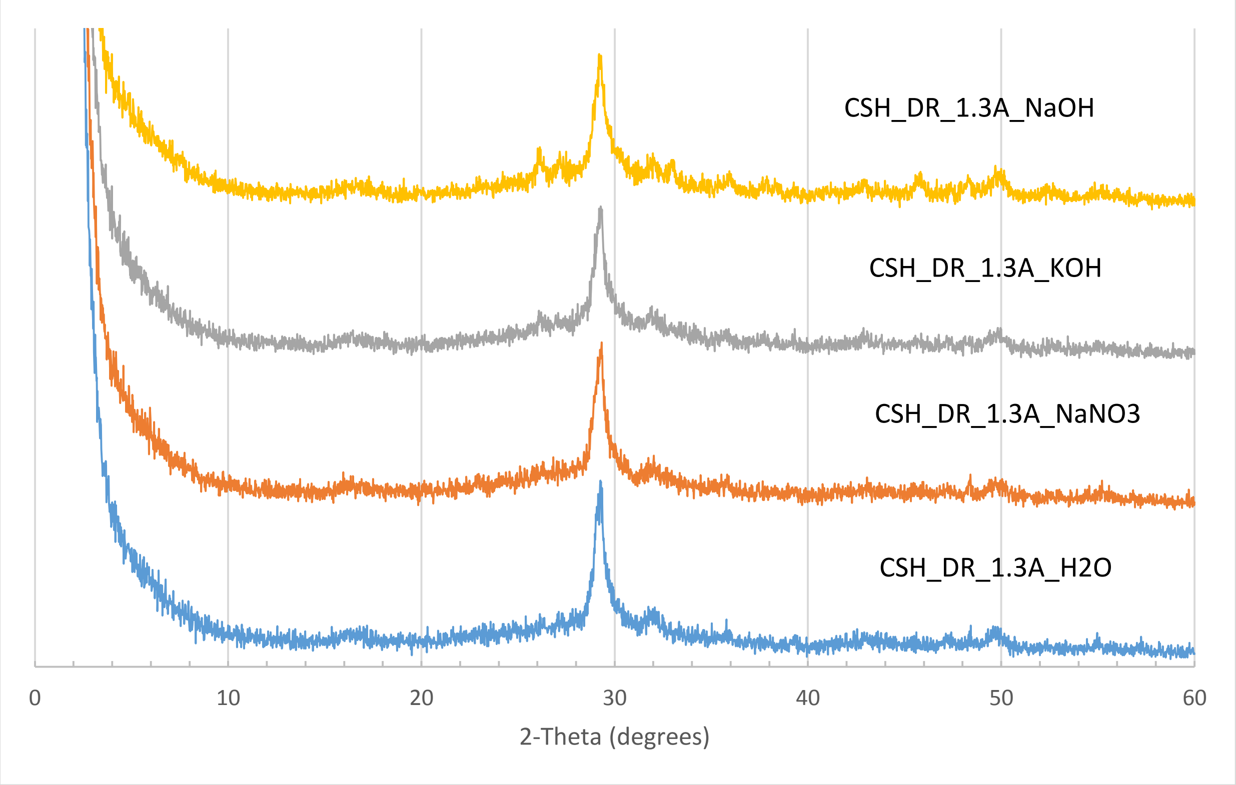

Figure 17: XRD pattern of carbonation treatment samples.

All C-S-H sample subjected to the carbonation treatment still show peaks associated with C-S-H at 16.9°, 29.2°, 32.0°, 42.7°, 49.8°, and 55.3°, as presented in Figure 17. Additionally, calcite and aragonite peaks are clearly visible in CSH_DR_1.3A_NaOH and CSH_DR_1.3A_KOH at 29.2°, 35.8° for calcite, and 39.4° and 26.2°, 27.1°, 37.8°, 45.7°, 48.3°, and 52.6° for aragonite. CSH_DR_1.3A_$NaNO_3$ and CSH_DR_1.3A_H_2O

contain calcite peaks at 29.2°, 35.8°, and 48.5°. CSH_DR_1.3A_NaOH appears to have the most distinct carbonate peaks, followed by CSH_DR_1.3A_KOH.

4.2 ^{29}Si NMR

All of the ^{29}Si spectra presented in this section are composed of three curves: the experimental curve (black), the individual peaks (red), and the sum of the individual peaks (blue).

4.2.1 C-S-H SYNTHESIZED BY DOUBLE DECOMPOSITION

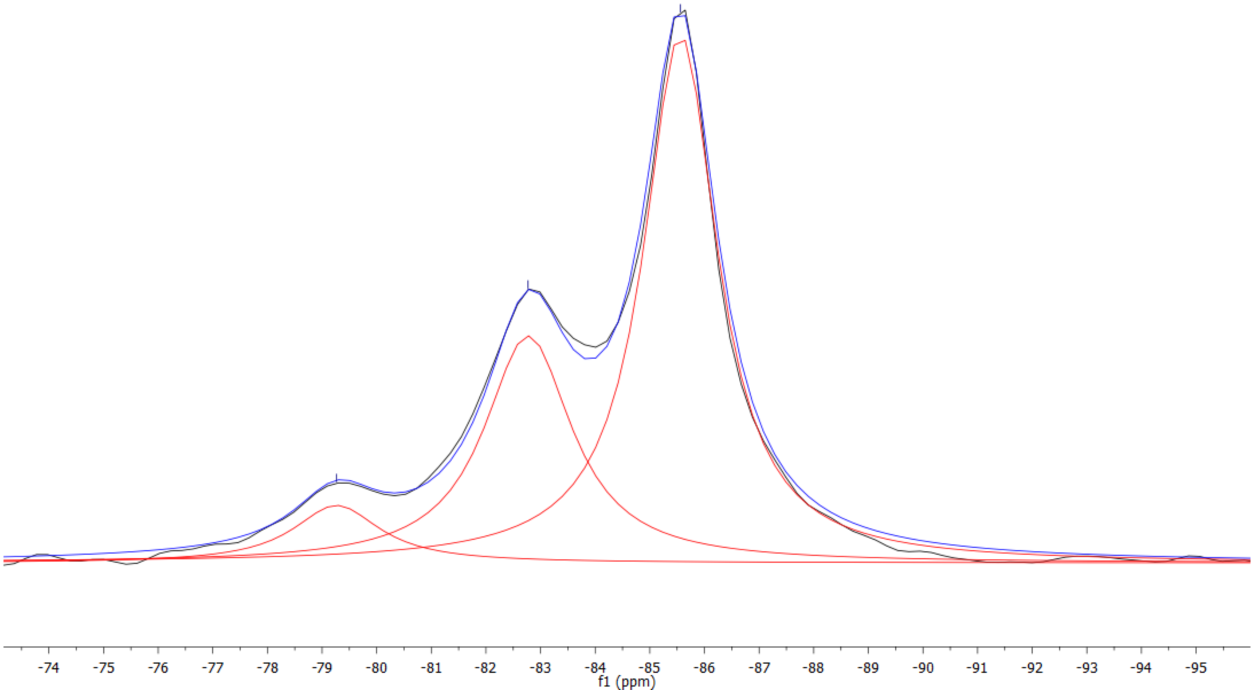

Figure 18: ^{29}Si NMR spectrum of CSH_DD_1.0A.

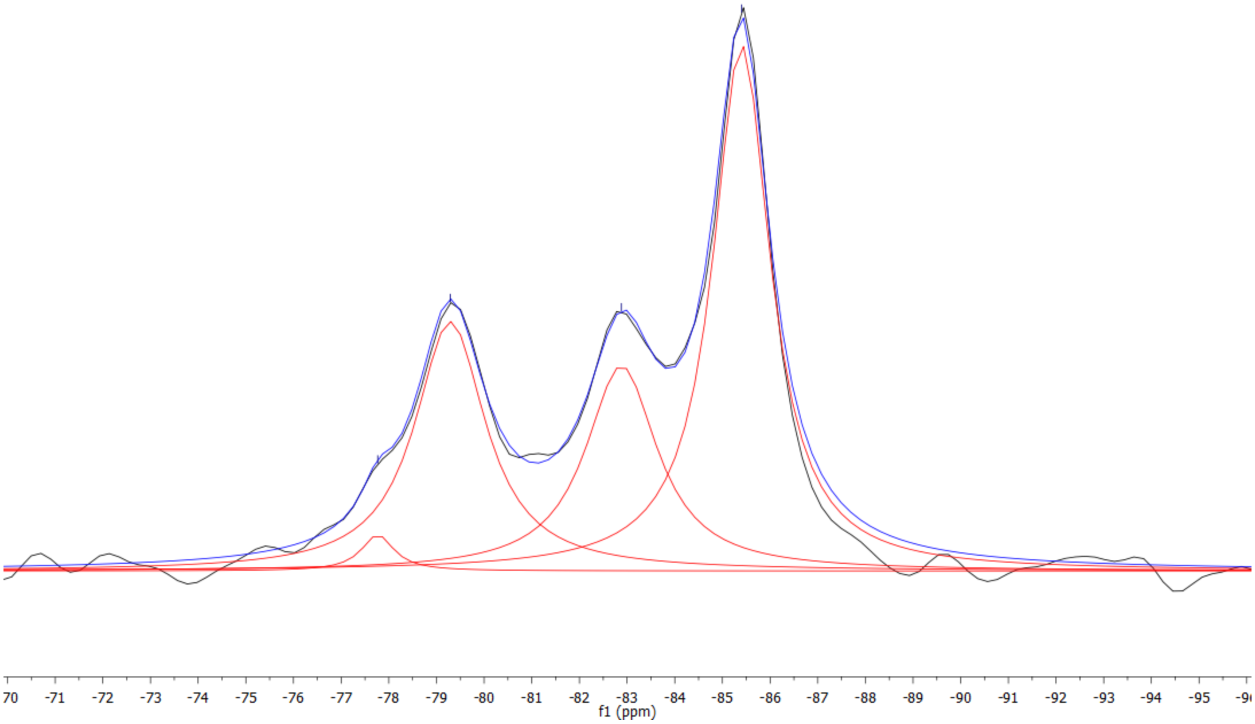

Figure 19: ^{29}Si NMR spectrum of CSH_DD_1.3A.

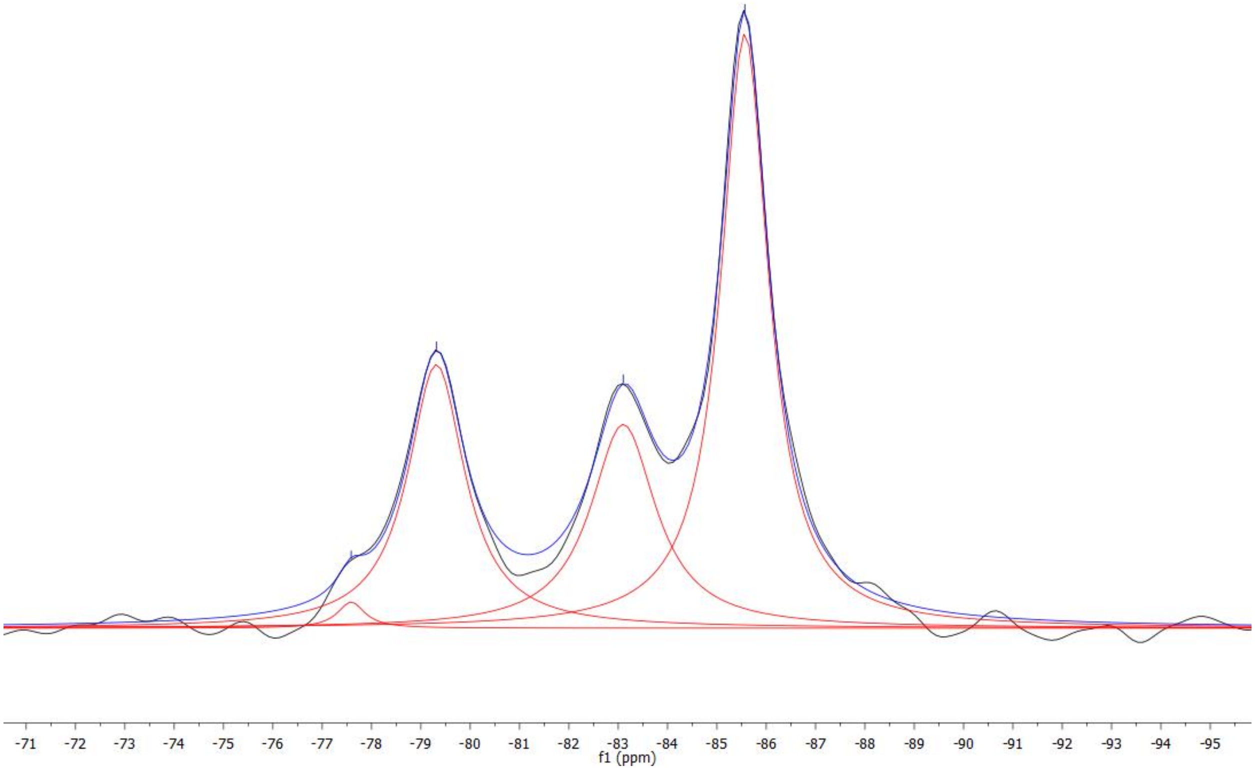

Figure 20: ^{29}Si NMR spectrum of CSH_DD_1.5A.

Table 3: Deconvolution peak properties for CSH_DD_1.0A, CSH_DD_1.3A, and CSH_DD_1.5A.

	$Q^n(mAl)$	Chemical shift (ppm)	Width (ppm)	Proportion
CSH_DD_1.0A	Q^1(0Al)	-79.3	1.93	7.8%
	Q^2_B(0Al)	-82.8	1.94	31.2%
	Q^2_P(0Al)	-85.6	1.64	61.0%
CSH_DD_1.3A	Q^1(0Al)?	-77.8	0.82	1.8%
	Q^1(0Al)	-79.3	1.79	27.6%
	Q^2_B(0Al)	-82.9	1.83	23.1%
	Q^2_P (0Al)	-85.4	1.46	47.4%
CSH_DD_1.5A	Q^1(0Al)?	-77.6	0.67	1.2%
	Q^1(0Al)	-79.3	1.39	26.1%
	Q^2_B(0Al)	-83.1	1.61	23.2%
	Q^2_P(0Al)	-85.6	1.17	49.4%

The ^{29}Si spectra of the C-S-H synthesized by double decomposition, shown in Figures 18-20 with peak properties in Table 3, show a dreierketten structure, similar to previous reports [11, 12]. The Q^1(0Al) peak at approximately -79.3 ppm and the Q^2_P(0Al) peak at approximately -85.5 ppm has been reported previously [2, 11, 31]. The Q^2_B(0Al) at approximately -83.0 has been previously reported as well, but not as frequently [25, 31] . CSH_DD_1.3A and CSH_DD_1.5A have very similar spectra, with large amounts of Q^2, which indicate a long MCL. CSH_DD_1.0A has a smaller proportion of Q^1, indicating it has a longer MCL than CSH_DD_1.3A and CSH_DD_1.5A. The peaks at -77.8 and -77.6 are of low intensity, and may be in the noise range. However, they may represent a Q^1 environment with a slightly less magnetically shielded chemical environment. A cause of this may be a difference in the ion that is charge balancing some of the end-chain silica sites.

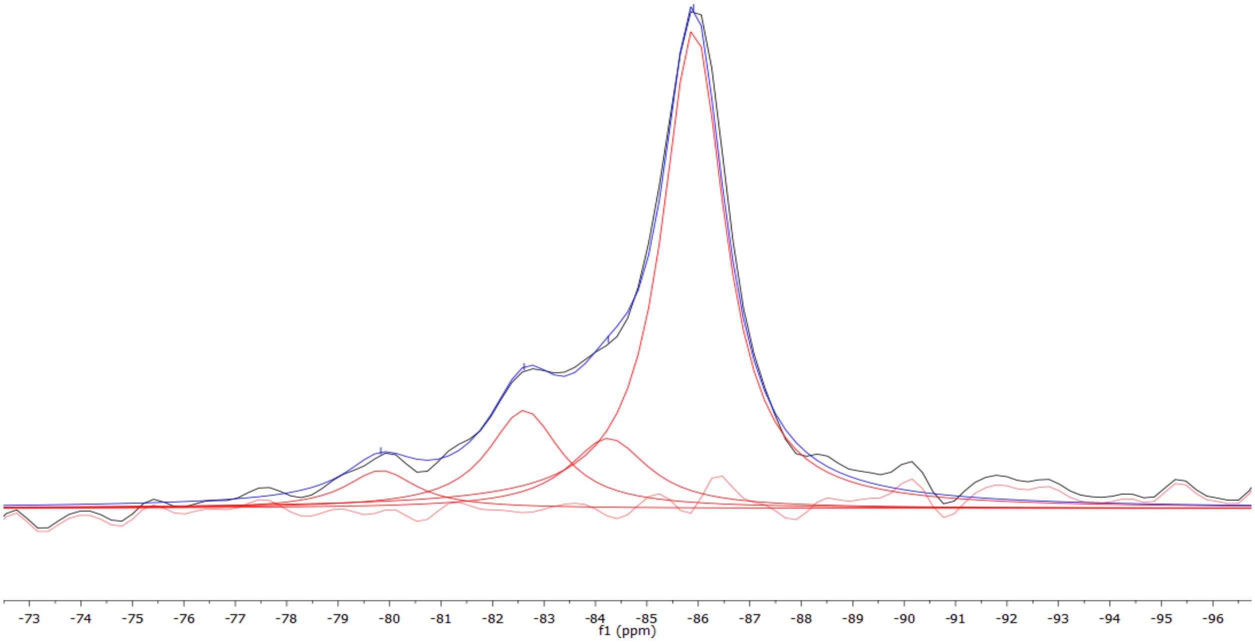

Figure 21: ^{29}Si NMR spectrum of CSH_DD_0.8B.

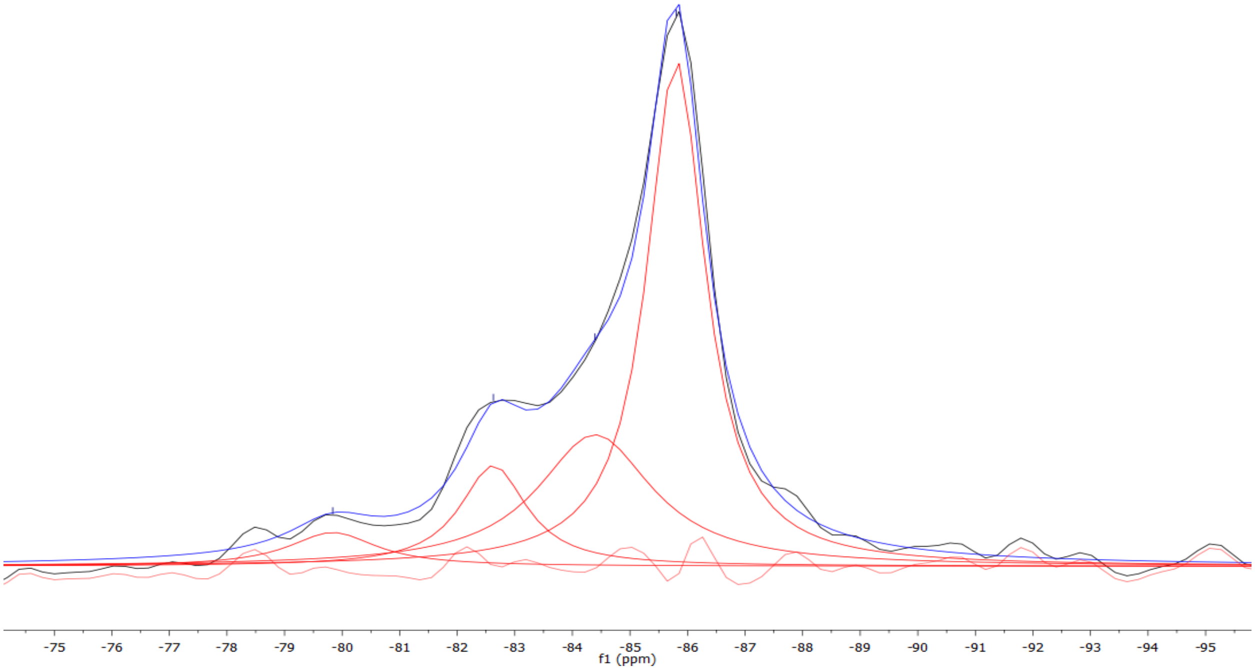

Figure 22: ^{29}Si NMR spectrum of CSH_DD_0.9B.

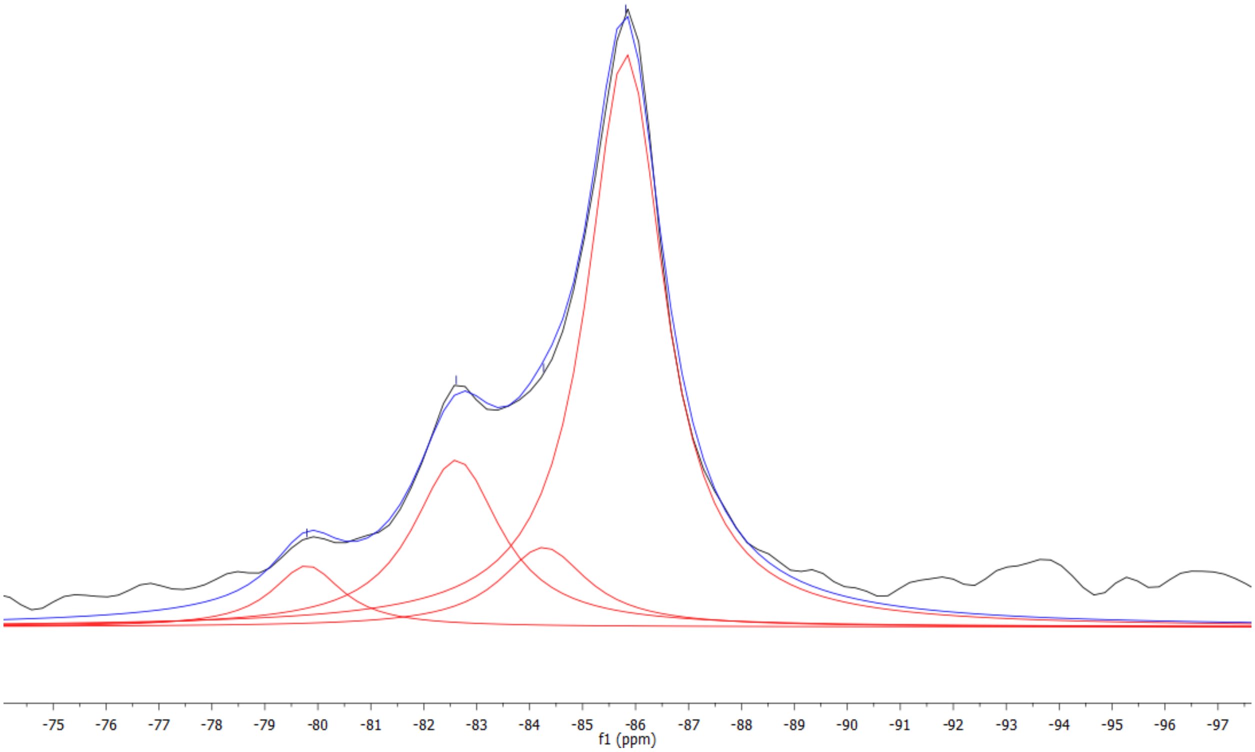

Figure 23: ^{29}Si NMR spectrum of CSH_DD_1.1B.

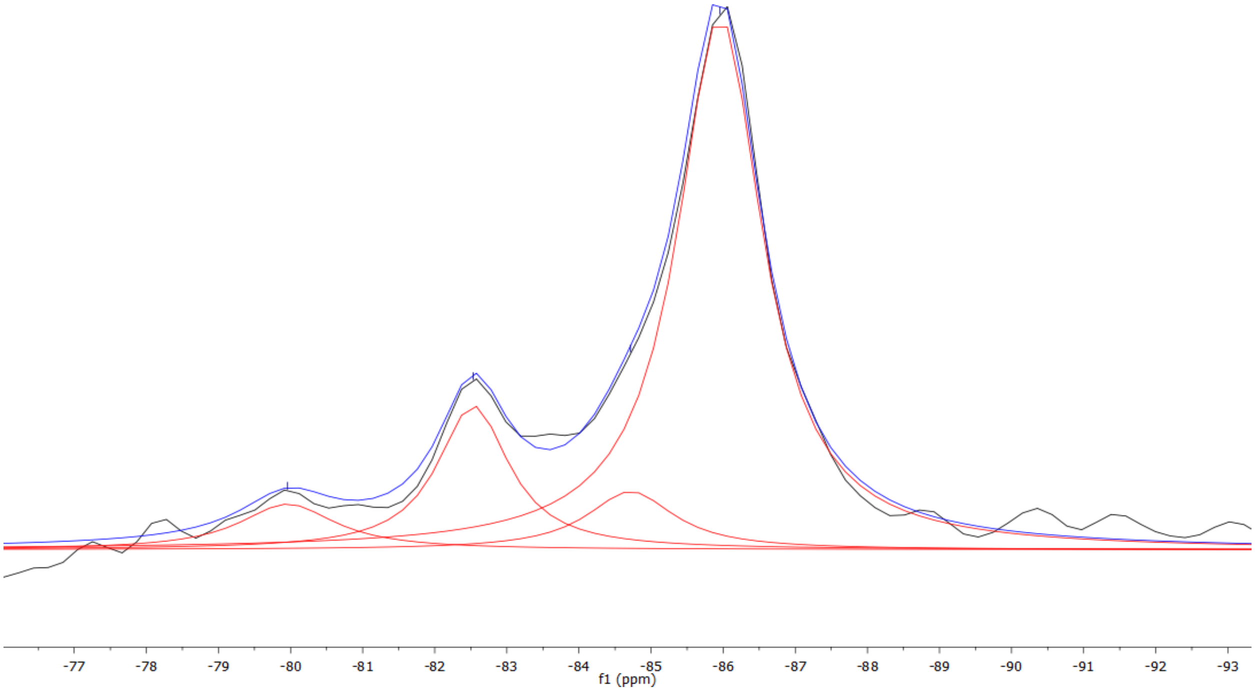

Figure 24: ^{29}Si NMR spectrum of CSH_DD_1.3B.

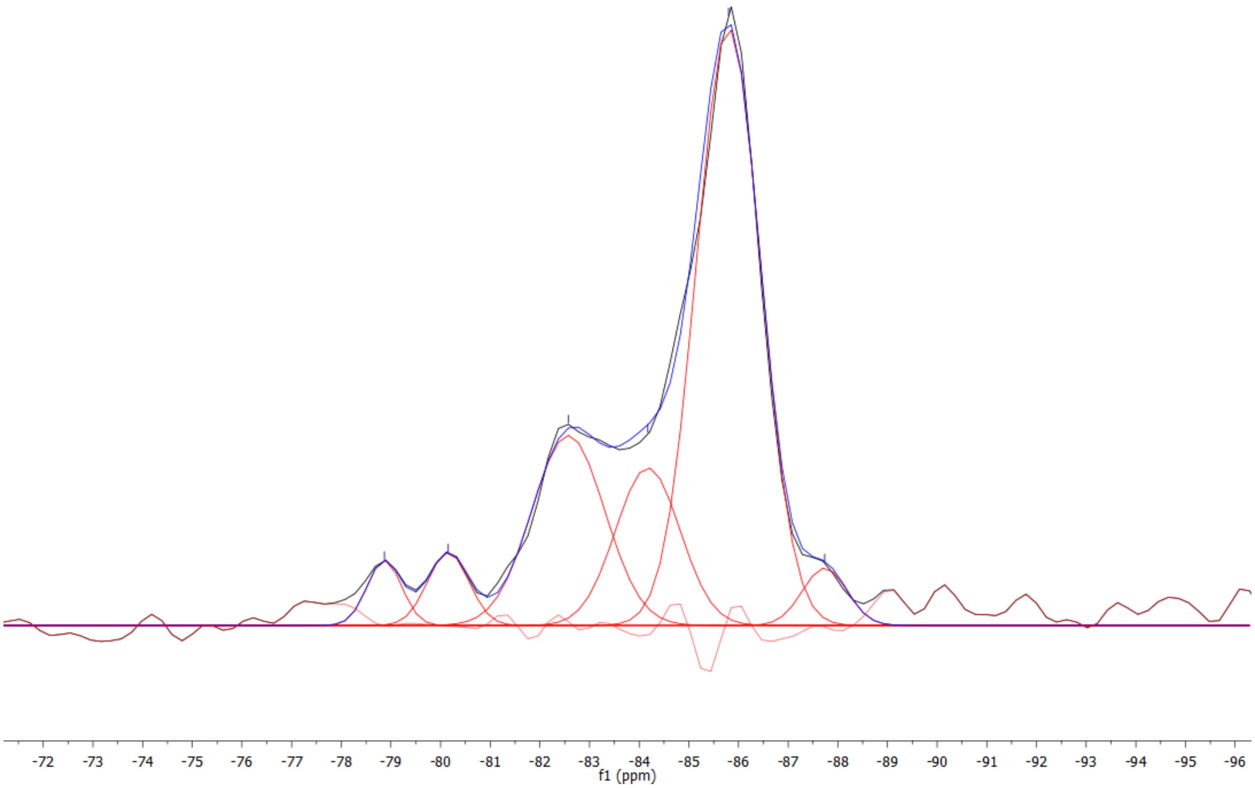

Figure 25: ^{29}Si NMR spectrum of CSH_DD_1.5B.

Table 4: Deconvolution peak properties for CSH_DD_0.8B, CSH_DD_0.9B, CSH_DD_1.1B, CSH_DD_1.3B, and CSH_DD_1.5B.

	$Q^n(m\mathrm{Al})$	Chemical shift (ppm)	Width (ppm)	Proportion
CSH_DD_0.8B	$Q^1(0\mathrm{Al})$	-79.8	1.66	5.8%
	$Q^2_B(0\mathrm{Al})$	-82.6	1.69	15.5%
	$Q^2_B(0\mathrm{Al})$?	-84.2	1.88	12.3%
	$Q^2_P(0\mathrm{Al})$	-85.9	1.49	66.4%
CSH_DD_0.9B	$Q^1(0\mathrm{Al})$	-79.8	1.84	5.5%
	$Q^2_B(0\mathrm{Al})$	-82.6	1.41	12.4%
	$Q^2_B(0\mathrm{Al})$?	-84.4	2.41	27.9%
	$Q^2_P(0\mathrm{Al})$	-85.8	1.22	54.2%
CSH_DD_1.1B	$Q^1(0\mathrm{Al})$	-79.8	1.61	6.1%
	$Q^2_B(0\mathrm{Al})$	-82.6	2.01	20.9%
	$Q^2_B(0\mathrm{Al})$?	-84.3	2.01	10.0%
	$Q^2_P(0\mathrm{Al})$	-85.8	1.76	63.0%
CSH_DD_1.3B	$Q^1(0\mathrm{Al})$	-80	1.63	6.7%
	$Q^2_B(0\mathrm{Al})$	-82.5	1.21	15.8%
	$Q^2_B(0\mathrm{Al})$?	-84.7	1.46	7.8%
	$Q^2_P(0\mathrm{Al})$	-86	1.44	69.7%
CSH_DD_1.5B	$Q^1(0\mathrm{Al})$?	-78.9	0.82	3.2%
	$Q^1(0\mathrm{Al})$	-80.2	0.97	4.3%
	$Q^2_B(0\mathrm{Al})$	-82.6	1.73	19.7%
	$Q^2_B(0\mathrm{Al})$?	-84.2	1.53	14.5%
	$Q^2_P(0\mathrm{Al})$	-85.8	1.53	54.7%
	$Q^3(0\mathrm{Al})$	-87.7	1.06	3.6%

The ^{29}Si spectra of the C-S-H samples prepared by double decomposition, presented in Figures 21-25 and peak properties in Table 4, reveal a dreierketten structure, as previously seen. All samples have a low Q^1 proportion and similar proportions of Q^2_B(0Al) to Q^2_P(0Al). All samples contain an unidentified peak at approximately -84.3 ppm. This peak is above the noise threshold and may be a Q^2_B(0Al) site that is charge balanced by an ion that causes more magnetic shielding than the ion that is charge balancing the Q^2_B(0Al) site at approximately -82.5 ppm. A possibility is Na^{1+} providing the charge balance for Q^2_B(0Al) instead of Ca^{2+}, which would result in a chemical shift. However, normally the bridging tetrahedron site is charge balanced by Ca^{2+} and the chemical shift is located at approximately -82.6 ppm and a bridging tetrahedron site charge balanced by Na^{1+} would have a less negative chemical shift than if it were charge balanced by Ca^{2+} since the atomic number of sodium is lower than that of calcium. Therefore, this is not a reasonable explanation. The origination of this peak is still unknown, but it should be noted that when a peak is located under the area of a more intense peak there is limited confidence. Sample CSH_DD_1.5B also contains an unidentified peak at -78.9 ppm, which is similar in position to the unidentified peaks in CSH_DD_1.3A and CSH_DD_1.5A. Again, charge balancing ions may be the cause of this small peak in the Q^1 range. CSH_DD_1.5B also contains a small amount of Q^3(0Al) at -87.7 ppm, indicating crosslinking of dreierketten chains through the silica bridging tetrahedra [2, 21, 34] . CSH_DD_1.5B showed $CaCO_3$ polymorphs by XRD and the carbonation of the C-S-H may be the source of Q^3 bonds across the silicate chains.

4.2.2 C-S-H SYNTHESIZED BY DIRECT REACTION

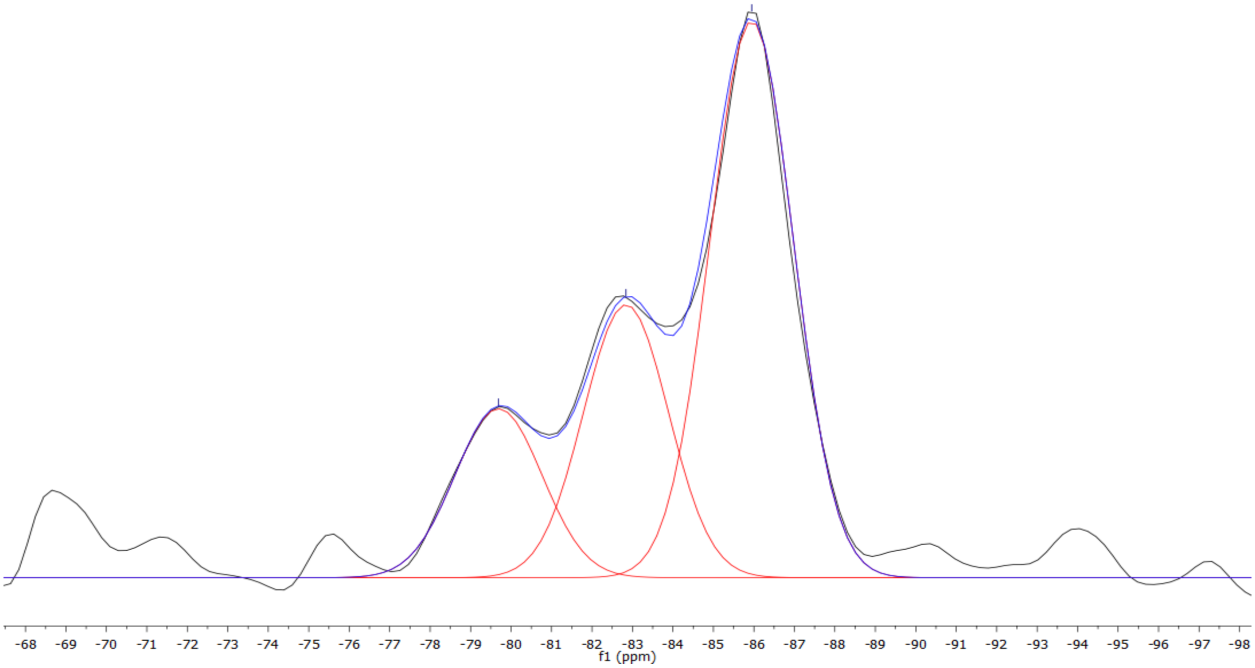

Figure 26: ^{29}Si NMR spectrum of CSH_DR_1.0A.

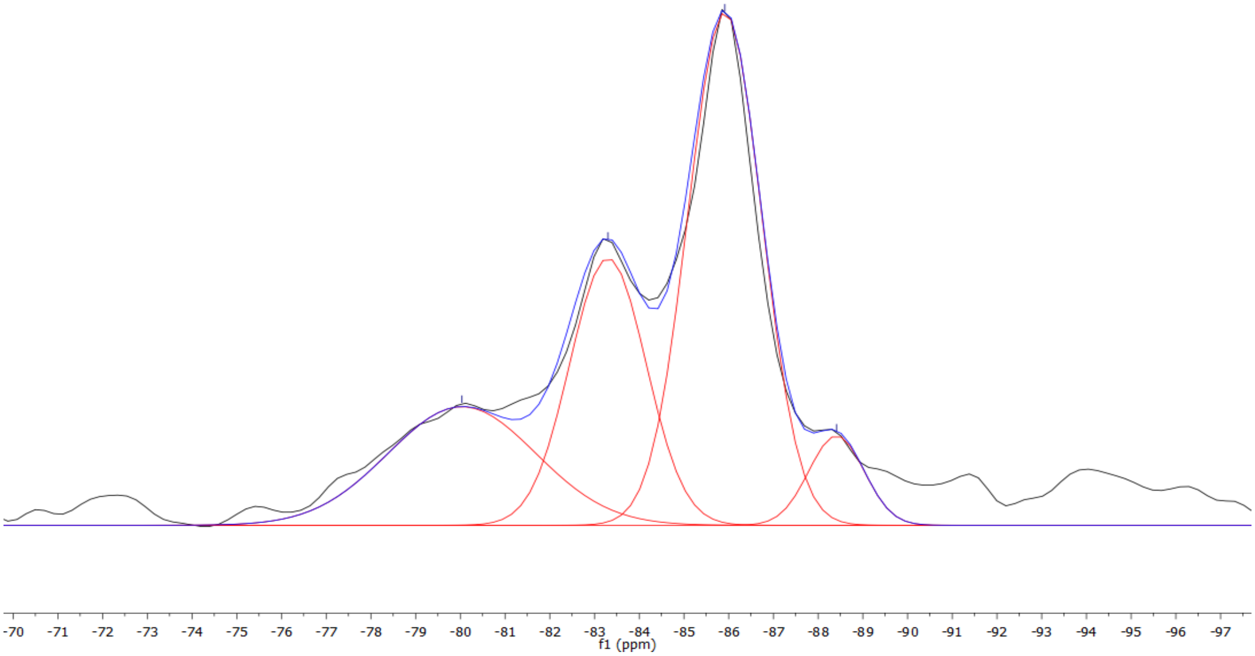

Figure 27: ^{29}Si NMR spectrum of CSH_DR_1.3A.

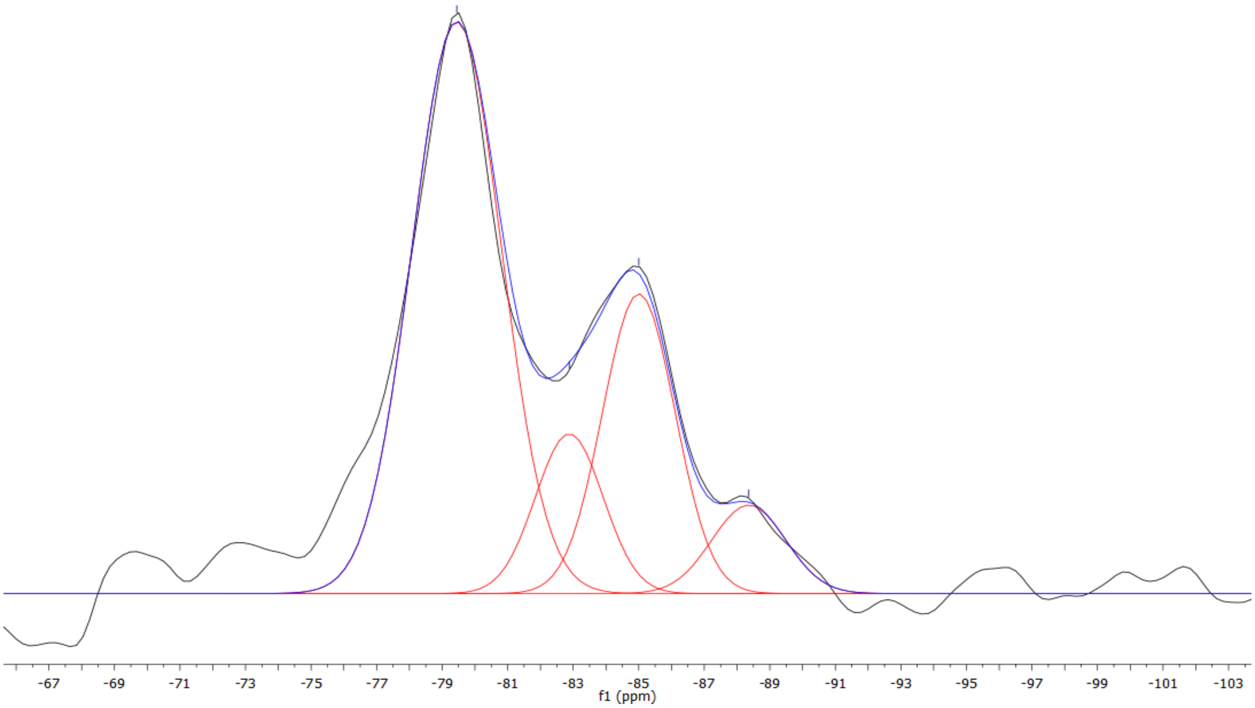

Figure 28: ^{29}*Si NMR spectrum of CSH_DR_1.5A.*

Table 5: Deconvolution peak properties for CSH_DR_1.0A, CSH_DR_1.3A, and CSH_DR_1.5A.

	Q^n(*mAl*)	Chemical shift (ppm)	Width (ppm)	Proportion
CSH_DR_1.0A	Q^1(0Al)	-79.7	2.53	17.5%
	Q^2_B(0Al)	-82.8	2.46	27.5%
	Q^2_P(0Al)	-85.9	2.43	55.0%
CSH_DR_1.3A	Q^1(0Al)	-80	3.89	21.7%
	Q^2_B(0Al)	-83.3	2.01	25.2%
	Q^2_P(0Al)	-85.9	1.94	46.9%
	Q^3(0Al)	-88.4	1.46	6.1%
CSH_DR_1.5A	Q^1(0Al)	-79.4	3.20	56.7%
	Q^2_B(0Al)	-82.9	2.43	12.0%
	Q^2_P(0Al)	-85	2.60	24.1%
	Q^3(0Al)	-88.4	2.65	7.2%

The ^{29}Si spectra of the C-S-H samples prepared by direct reaction, presented in Figures 26-28 and peak properties in Table 5, reveal a dreierketten structure, as previously seen. The proportion of Q^1(0Al) increases with the Ca/Si ratio of the starting reagents, indicating a shorter MCL. CSH_DR_1.3A and CSH_DR_1.5A also contain a small amount of Q^3(0Al), which crosslinks chains through silica bridging tetrahedra.

4.2.3 C-A-S-H SYNTHESIZED BY DOUBLE DECOMPOSITION

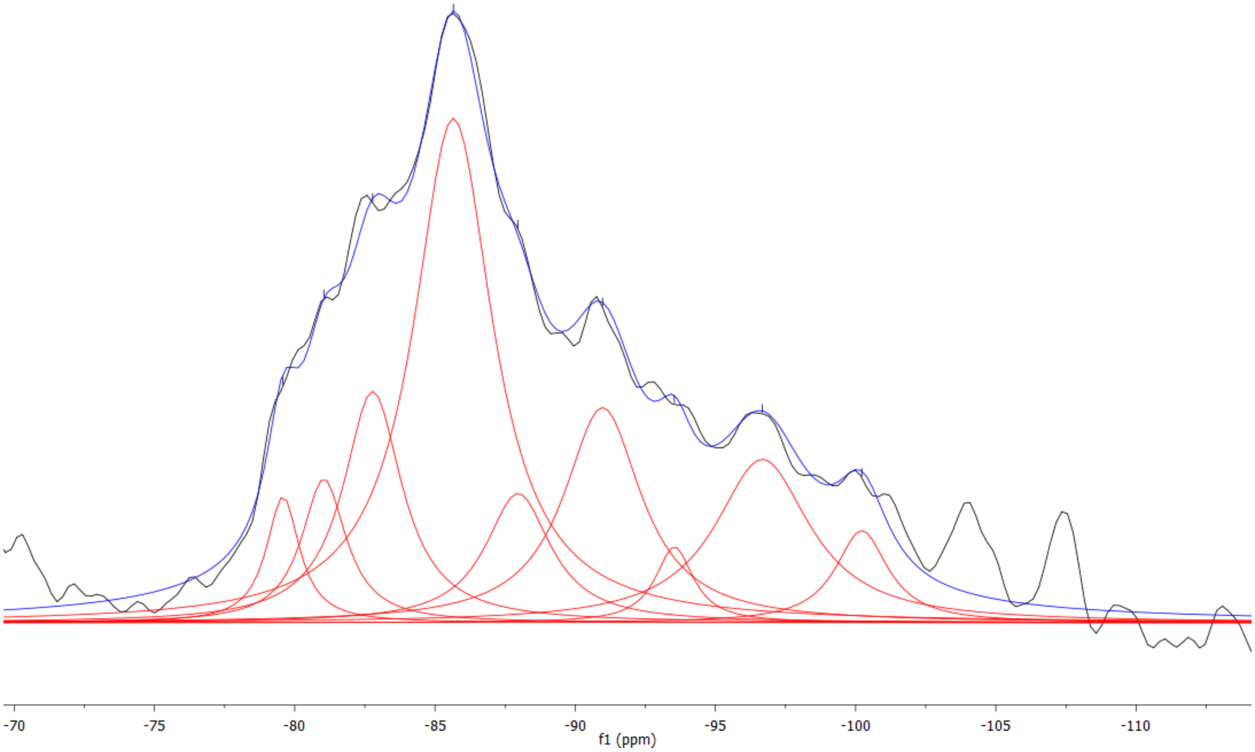

Figure 29: ^{29}Si NMR spectrum of CASH_DD_0.9B.

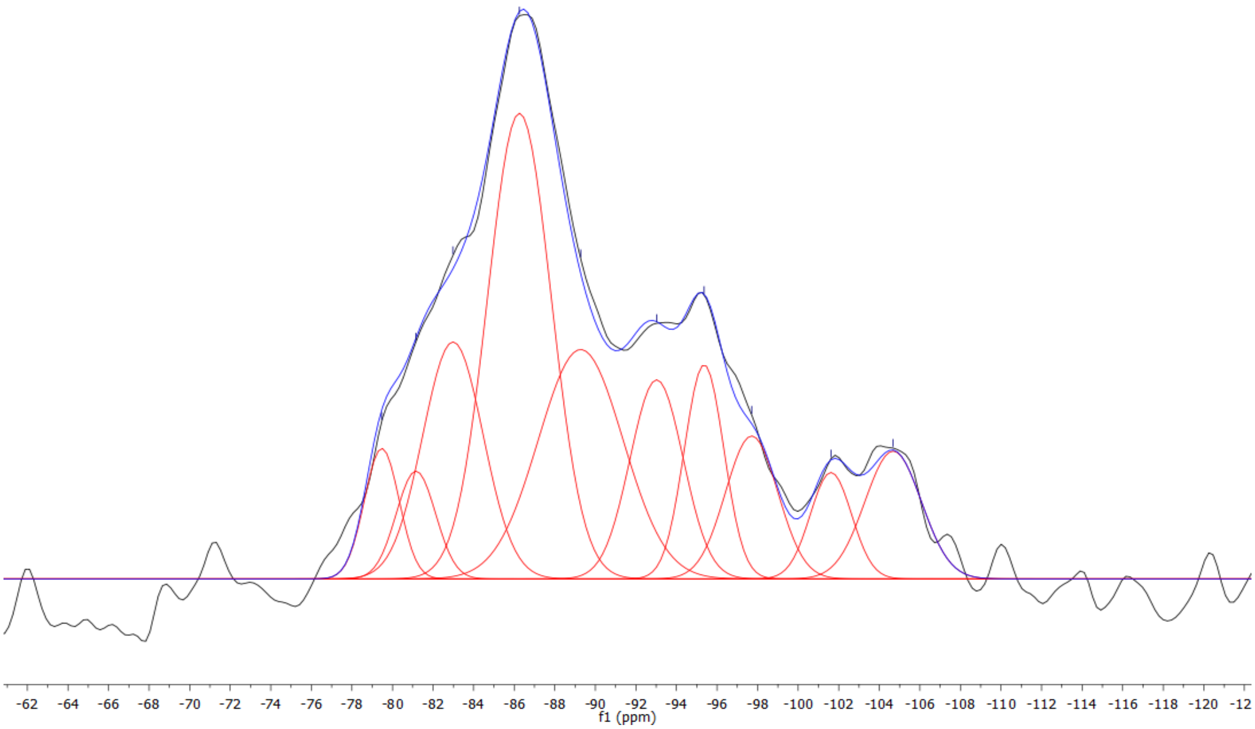

Figure 30: ^{29}Si NMR spectrum of CASH_DD_1.1B.

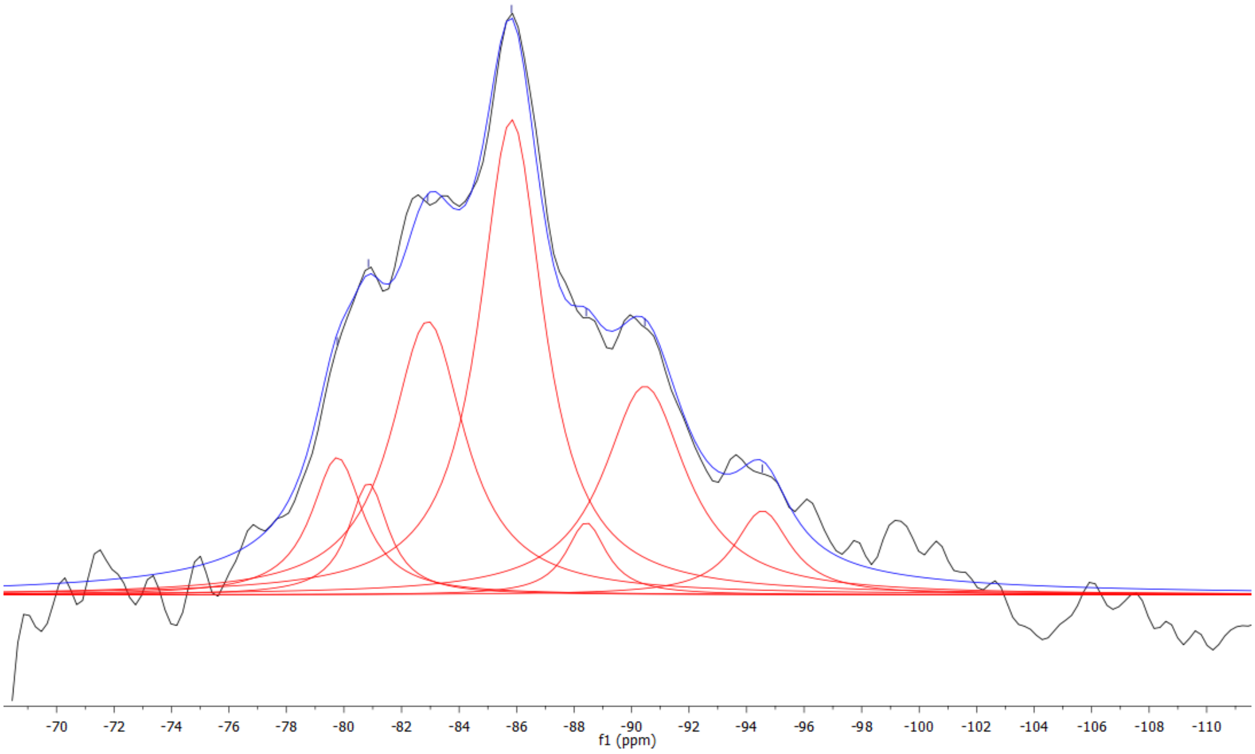

Figure 31: ^{29}Si NMR spectrum of CASH_DD_1.3B.

Table 6: Deconvolution peak properties for CASH_DD_0.9B, CASH_DD_1.1B, and CASH_DD_1.3B.

	Q^n(*mAl*)	Chemical shift (ppm)	Width (ppm)	Proportion
CASH_DD_0.9B	Q^1(0Al)	-79.6	1.42	3.7%
	Q^2_P(1Al)	-81	1.91	5.7%
	Q^2_B(0Al)	-82.8	2.55	12.1%
	Q^2_P(0Al)	-85.7	3.42	35.5%
	Q^3(1Al)	-88	2.83	7.5%
	Q^3(0Al)	-91	3.35	14.9%
	Q^4(2Al)	-93.5	1.64	2.6%
	Q^4(1Al)	-96.7	4.11	13.8%
	Q^4(0Al)	-100.2	2.28	4.3%
CASH_DD_1.1B	Q^1(0Al)	-79.5	2.01	4.4%
	Q^2_P(1Al)	-81.2	2.28	4.1%
	Q^2_B(0Al)	-83	3.50	13.9%
	Q^2_P(0Al)	-86.3	3.69	28.7%
	Q^3(1Al)	-89.3	4.91	18.9%
	Q^3(0Al)	-93	3.07	10.2%
	Q^4(2Al)	-95.4	2.30	8.2%
	Q^4(1Al)	-97.7	3.03	7.3%
	Q^4(0Al)	-101.6	2.40	4.3%
CASH_DD_1.3B	Q^1(0Al)	-79.8	2.20	8.2%
	Q^2_P(1Al)	-80.8	1.68	5.1%
	Q^2_B(0Al)	-82.9	3.10	23.2%
	Q^2_P(0Al)	-85.8	2.70	35.0%
	Q^3(1Al)	-88.4	1.71	3.4%
	Q^3(0Al)	-90.5	3.45	19.7%
	Q^4(2Al)	-94.6	2.36	5.4%

The ^{29}Si spectra for C-A-S-H samples are somewhat more complex than the spectra for C-S-H samples. Additional peaks exist due to the 3-5 ppm downfield chemical shift that is caused by a silica tetrahedron being bonded to an alumina tetrahedron instead of another silica tetrahedron. The ^{29}Si spectra for the C-A-S-H samples synthesized by double decomposition, presented in Figures 29-31 and peak properties in Table 6, show peaks associated with the dreierketten structure that describes C-S-H as well as peaks with higher polymerization that are attributed to alumina/silica gel. Each sample has a Q^2_P(1Al) peak at approximately -81.0 ppm that indicates alumina in the bridging tetrahedra [2, 21, 24]. The proportion of this peak is similar across the samples. The proportion of Q^1(0Al) increases with the Ca/Si ratio of the starting reagents, indicating a shorter MCL with Ca/Si ratio. There is some difficulty in assigning the coordination and Al/Si connectivity of the peaks associated with silica gel since the amount of aluminum is variable and the peaks are generally not well defined. The Q^3(mAl) peaks may be part of the C-A-S-H or the alumina/silica gel [2, 21] . The Q^4(mAl) peaks are all associated with alumina/silica gel, supported by the presence of $CaCO_3$ polymorphs observed from XRD. The Q^4(mAl) peaks are assigned from general ranges of chemical shifts: Q^4(4Al) at -80 to -85 ppm, Q^4(3Al) at -85 to -98 ppm, Q^4(2Al) at -93 to -103 ppm, Q^4(1Al) at -96 to -110 ppm, and Q^4(0Al) at -100 to -120 ppm [41].

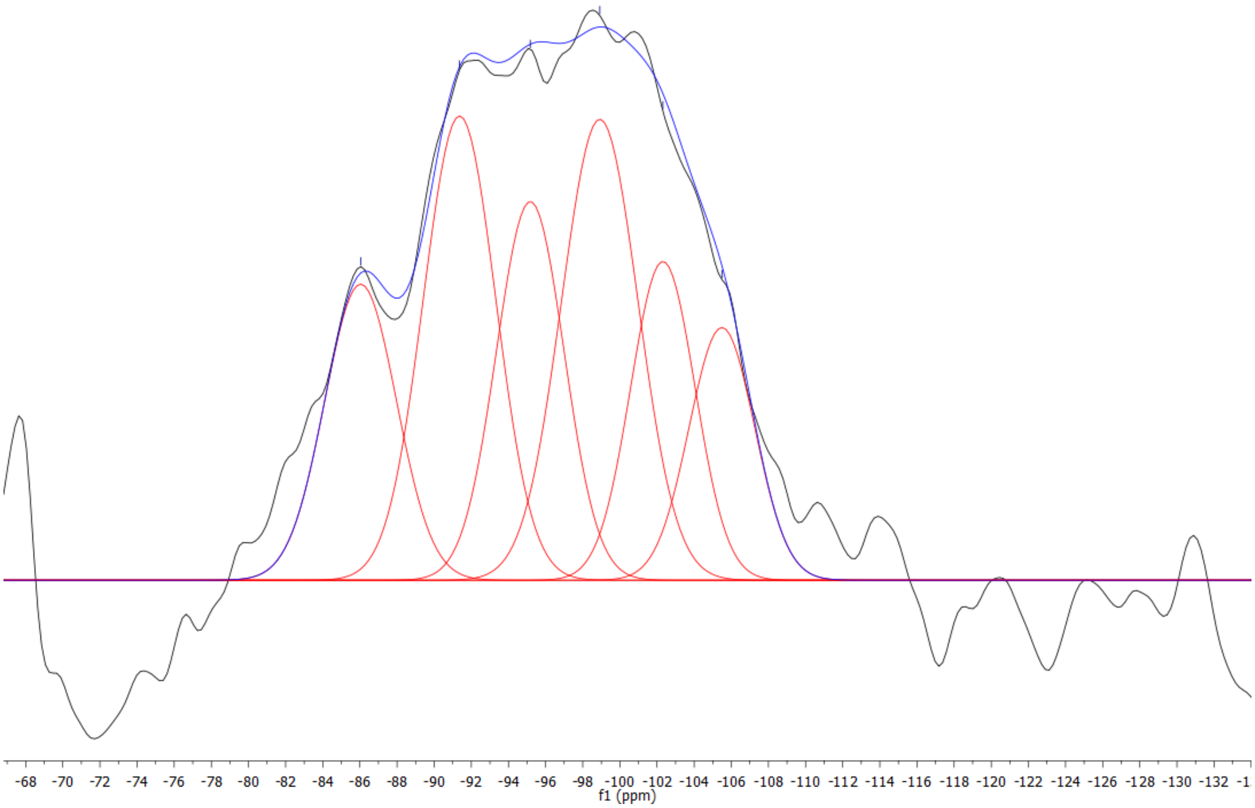

Figure 32: ^{29}Si NMR spectrum of CASH_DD_2.2H.

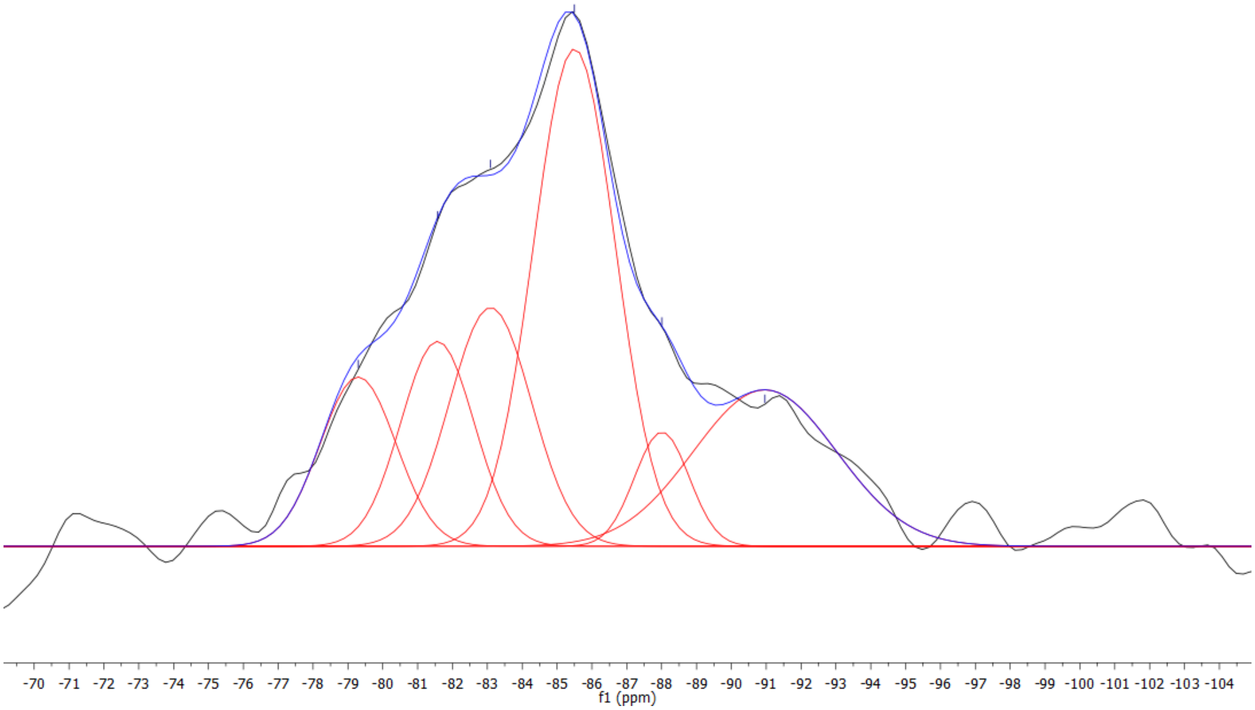

Figure 33: ^{29}Si NMR spectrum of CASH_DD_2.2L.

Table 7: Deconvolution peak properties for CASH_DD_2.2H and CASH_DD_2.2L.

	Q^n(*mAl*)	Chemical shift (ppm)	Width (ppm)	Proportion
CASH_DD_2.2H	Q^4(3Al)	-86	4.54	13.9%
	Q^3(0Al)	-91.4	4.59	22.0%
	Q^4(2Al)	-95.2	4.27	16.7%
	Q^4(1Al)	-98.9	4.84	23.1%
	Q^4(0Al)	-102.3	4.07	13.4%
	Q^4(0Al)	-105.5	4.16	10.8%
CASH_DD_2.2L	Q^1(0Al)	-79.3	2.56	11.0%
	Q^2_P(1Al)	-81.6	2.46	12.8%
	Q^2_B(0Al)	-83.1	2.77	16.7%
	Q^2_P(0Al)	-85.5	2.77	34.9%
	Q^3(1Al)	-88	1.84	5.3%
	Q^3(0Al)	-91	4.83	19.2%

The ^{29}Si spectra, presented in Figure 32 and peak properties in Table 7, for CASH_DD_2.2H is entirely Q^3(0Al) and Q^4(mAl), indicating that there is only alumina/silica gel. CASH_DD_2.2L, presented in Figure 33 and peak properties in Table 7, shows peaks characteristic of C-A-S-H with a large proportion of Q^3(mAl). It is likely that the Q^3(mAl) peaks are associated with crosslinking C-A-S-H and not alumina/silica gel since there is no Q^4(mAl) presence.

4.2.4 C-A-S-H SYNTHESIZED BY DIRECT REACTION

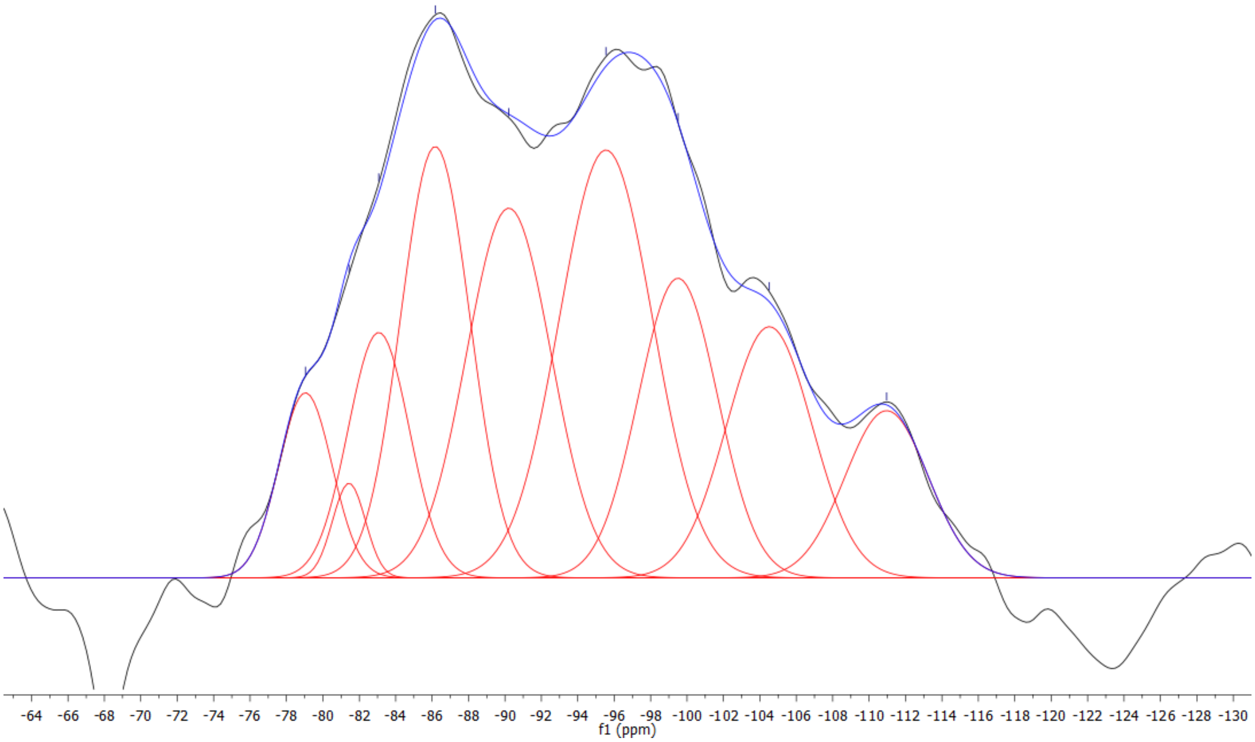

Figure 34: ^{29}Si NMR spectrum of CASH_DR_1.0A.

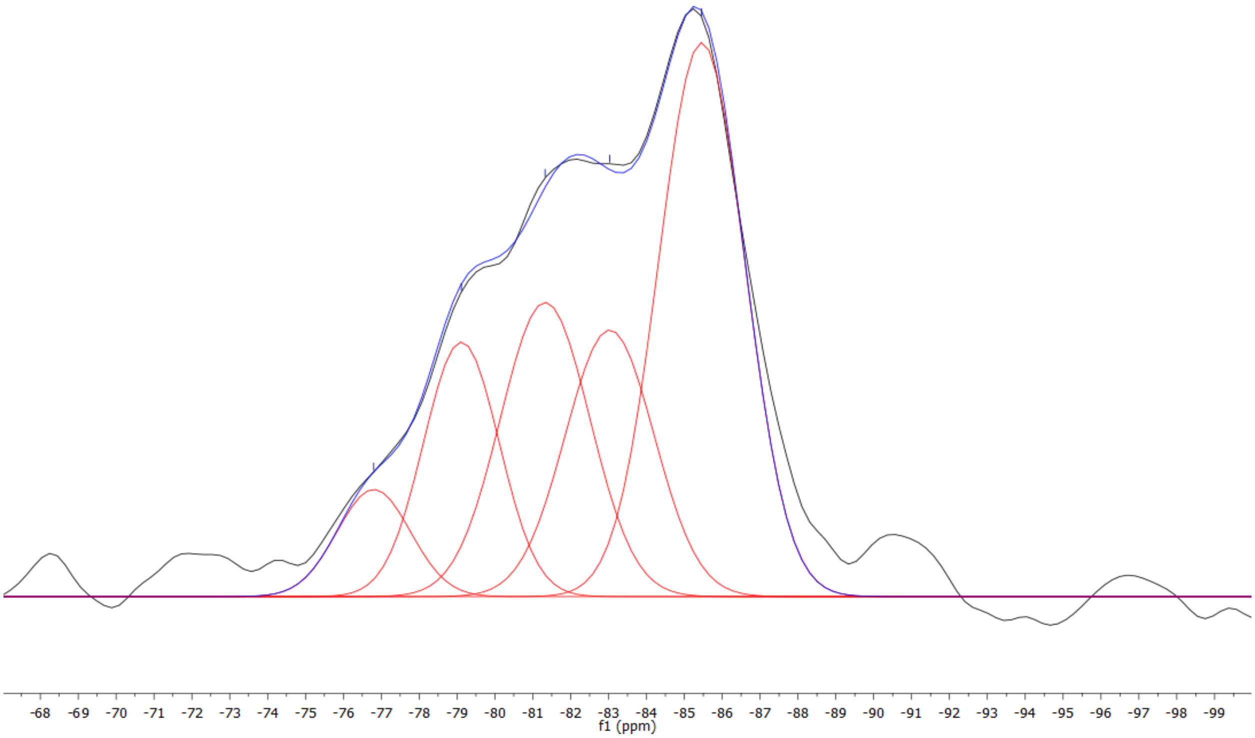

Figure 35: ^{29}Si NMR spectrum of CASH_DR_1.3A.

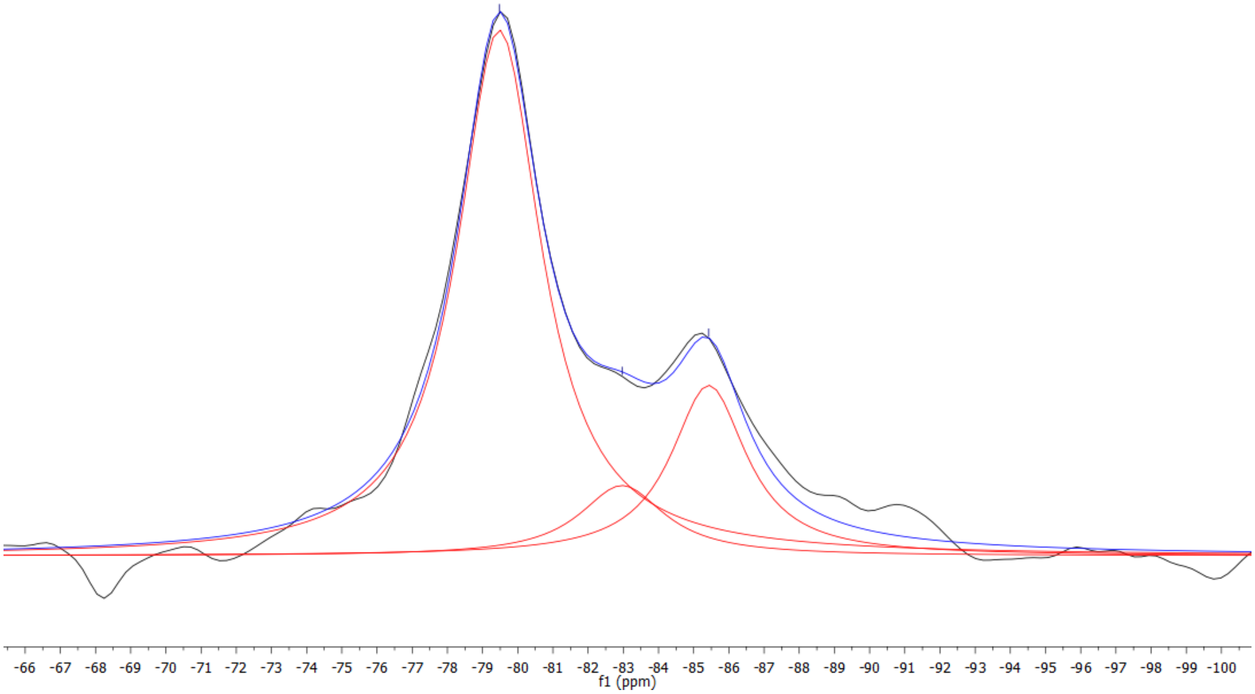

Figure 36: ^{29}Si NMR spectrum of CASH_DR_1.5A.

Table 8: Deconvolution peak properties for CASH_DR_1.0A, CASH_DR_1.3A, and CASH_DR_1.5A.

	Q^n(*mAl*)	Chemical shift (ppm)	Width (ppm)	Proportion
CASH_DR_1.0A	Q^1(0Al)	-79	3.45	5.3%
	Q^2_P(1Al)	-81.4	2.13	1.7%
	Q^2_B(0Al)	-83.1	3.96	8.0%
	Q^2_P(0Al)	-86.2	4.48	15.9%
	Q^3(1Al)	-90.2	5.46	16.6%
	Q^4(2Al)	-95.5	6.02	21.2%
	Q^4(1Al)	-99.5	5.11	12.6%
	Q^4(0Al)	-104.5	5.53	11.4%
	Q^4(0Al)	-111	5.38	7.4%
CASH_DR_1.3A	Q^1(1Al)	-76.8	2.28	6.3%
	Q^1(0Al)/Q^2_B(1Al)	-79.1	2.35	9.1%/6.3%
	Q^2_P(1Al)	-81.3	2.78	21.1%
	Q^2_B(0Al)	-83	2.75	19.0%
	Q^2_P(0Al)	-85.5	2.67	38.2%
CASH_DR_1.5A	Q^1(0Al)	-79.5	2.88	70.0%
	Q^2_B(0Al)	-83	2.93	9.5%
	Q^2_P(0Al)	-85.4	2.60	20.5%

The ^{29}Si spectra for CASH_DR_1.0A, presented in Figure 34 and peak properties in Table 8, indicates large amounts of alumina/silica gel with some C-A-S-H. Sample CASH_DR_1.3A, presented in Figure 35 and peak properties in Table 8, has typical C-A-S-H peaks, in addition to a peak at -76.8 ppm which can be assigned to Q^1(1Al). This assignment is made based on the 3 to 5 ppm chemical shift downfield from the Q^1(0Al) peak at approximately -79.5 when an alumina tetrahedron is bonded to the tetrahedral silica. It is highly likely that a Q^2_B(1Al) environment can be inferred from the presence of the Q¹(1Al) peak because Al[4] must be in a pairing position, as shown in Figure 37.

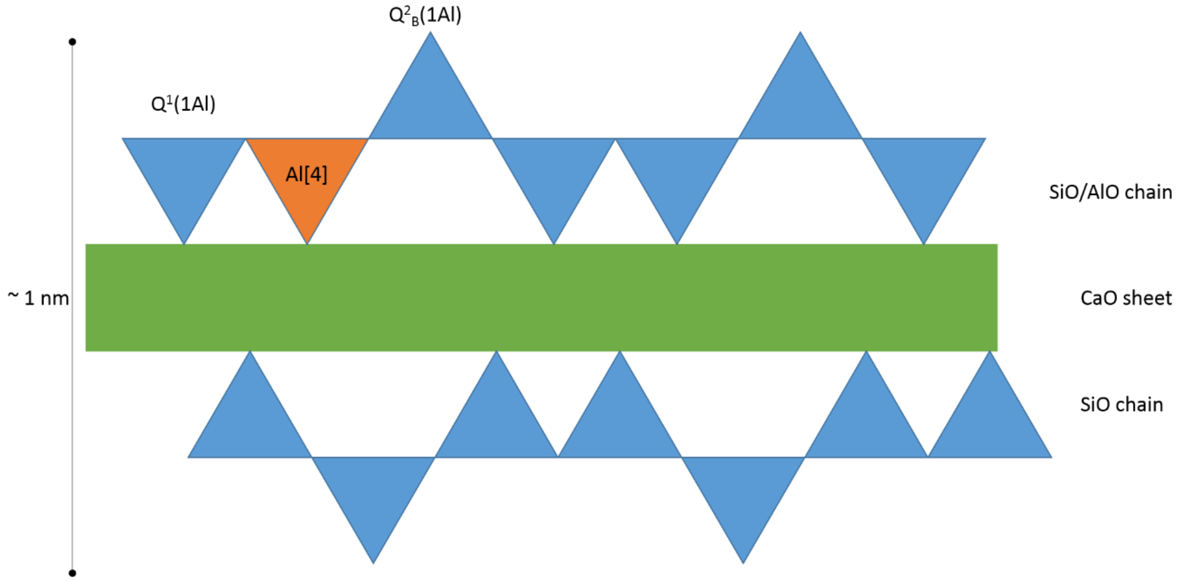

Figure 37: Molecular structure and associated ^{29}Si NMR peaks assignments for Al[4] in the pairing tetrahedron.

Aluminum in the pairing tetrahedron has been reported previously, although to a limited extent [22, 23]. However, the previous reports of aluminum in the pairing position came from data obtained by triple quantum ^{27}Al experiments This environment has been assigned to spectra which show a Q^1(1Al) peak. The assumption that there is no Al[4] in a chain ending site is reasonable since the MCL of the samples is long. If there is no chain ending Al[4], then the quantity of Q^2_B(1Al) must be equal to or greater than the quantity of Q^1(1Al). The quantity of Q^2_B(1Al) would be greater than Q^1(1Al) if Al[4] occurred in a pairing tetrahedron in the middle of the chain. For the purposes of this study, they are assumed to be equal. The Q^2_B(1Al) and Q^1(0Al) peaks overlap and are not possible to differentiate by means of deconvolution, thus the proportion of Q^1(0Al) and Q^2_B(1Al) were found by subtracting the area of the peak at -76.8 ppm from the area of the peak at -79.1 ppm. The presence of the Q^1(1Al) peak means that alumina is going into some pairing tetrahedra positions, not exclusively into bridging tetrahedra. CASH_DR_1.5A, presented in Figure 36 and peak properties in Table 8, has a very intense Q^1(0Al) peak which indicates short MCL. No Q^2_P(1Al) peak is present, indicating that no aluminum entered the structure. This is confirmed from ^{27}Al NMR in the next section.

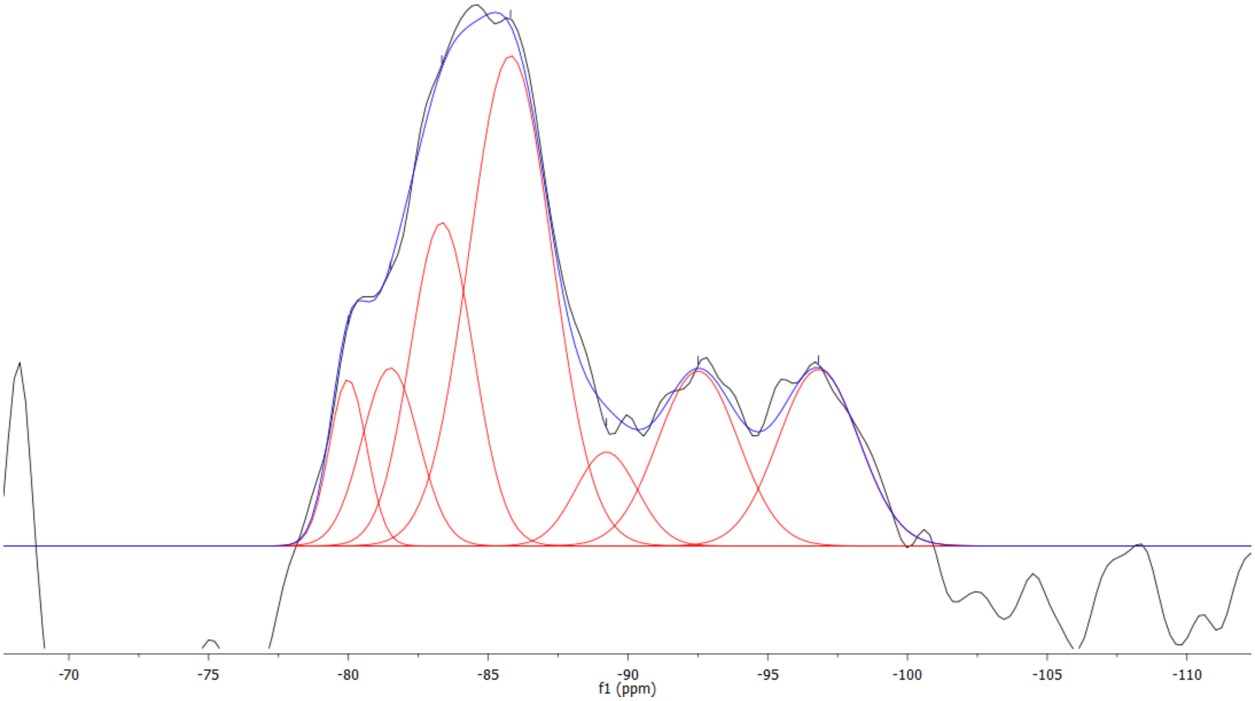

Figure 38: ^{29}Si NMR spectrum of CASH_DR_1.0B.

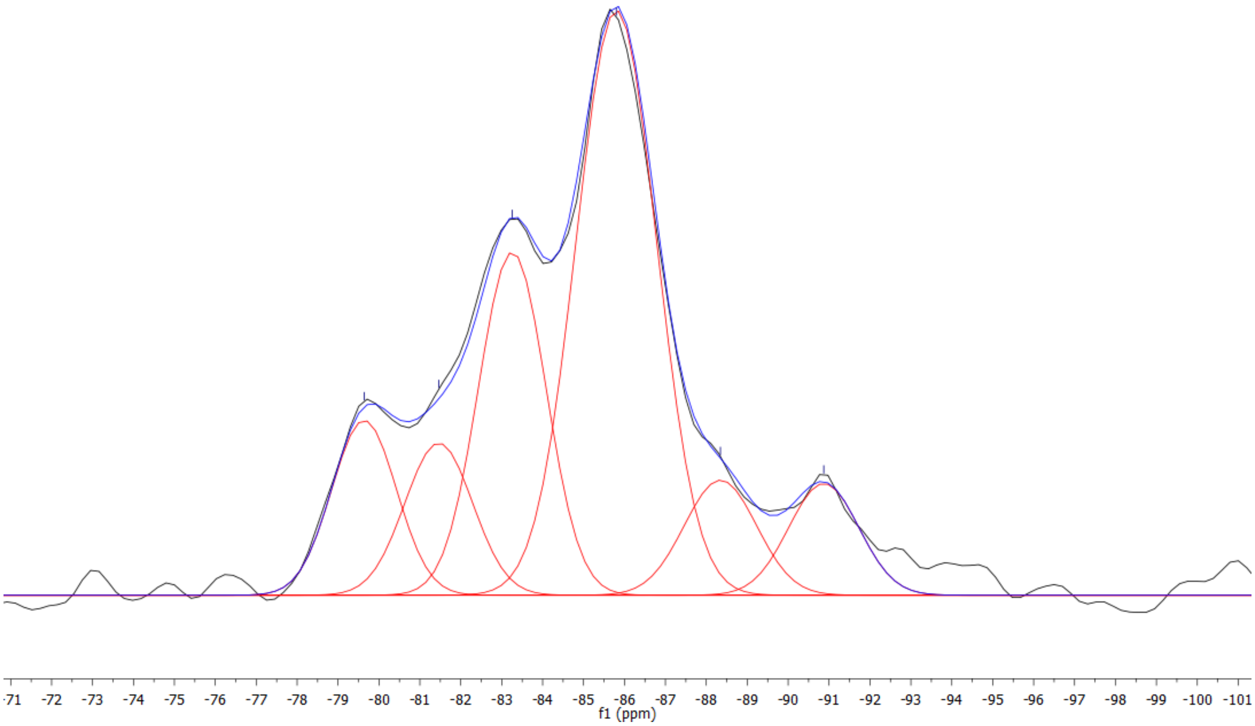

Figure 39: ^{29}Si NMR spectrum of CASH_DR_1.3B.

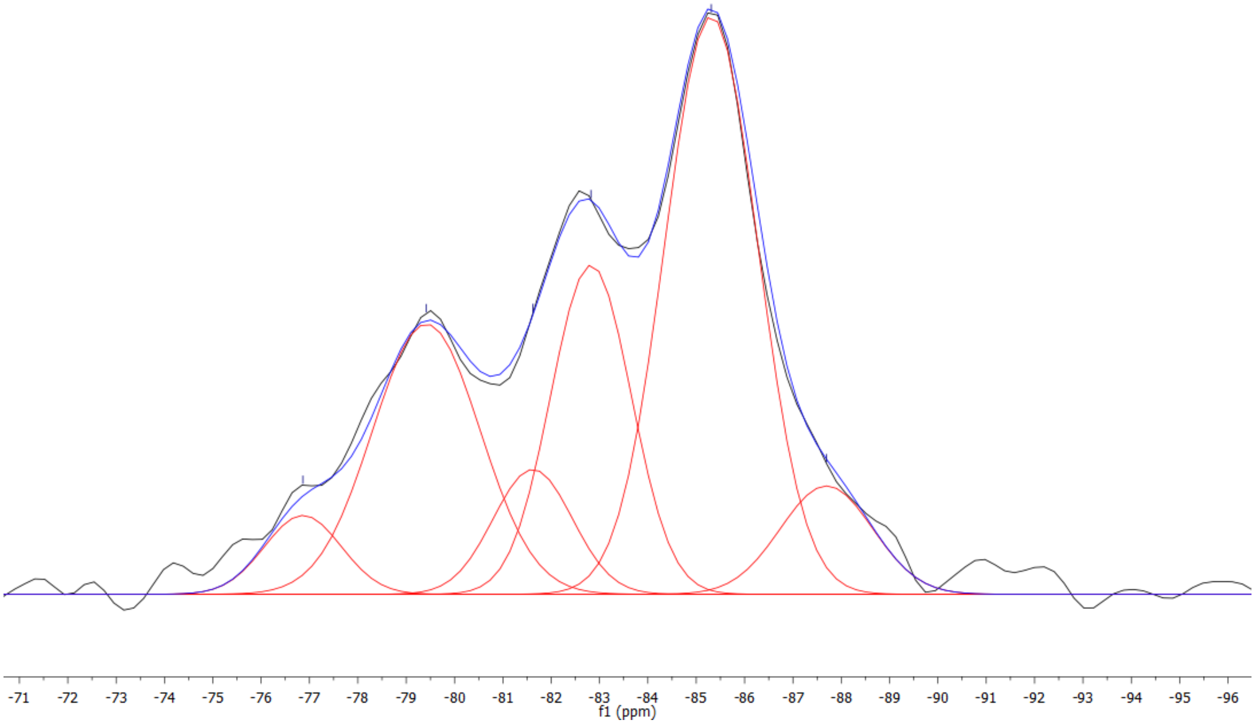

Figure 40: ^{29}Si NMR spectrum of CASH_DR_1.5B.

Table 9: Deconvolution peak properties for CASH_DR_1.0B, CASH_DR_1.3B, and CASH_DR_1.5B.

	$Q^n(mAl)$	Chemical shift (ppm)	Width (ppm)	Proportion
CASH_DR_1.0B	Q^1(0Al)	-80	1.56	5.6%
	Q^2_P(1Al)	-81.5	2.36	9.0%
	Q^2_B(0Al)	-83.3	2.65	18.3%
	Q^2_P(0Al)	-85.8	3.47	36.4%
	Q^3(1Al)	-89.2	2.58	5.2%
	Q^3(0Al)	-92.5	3.39	12.7%
	Q^4(2Al)	-96.8	3.39	12.8%
CASH_DR_1.3B	Q^1(0Al)	-79.6	1.86	10.5%
	Q^2_P(1Al)	-81.5	1.94	9.6%
	Q^2_B(0Al)	-83.3	1.94	21.4%
	Q^2_P(0Al)	-85.8	2.31	43.6%
	Q^3(1Al)	-88.3	2.08	7.7%
	Q^3(0Al)	-90.9	2.01	7.3%
CASH_DR_1.5B	Q^1(1Al)	-76.9	1.86	4.5%
	Q^1(0Al)/Q^2_B(1Al)	-79.4	2.61	17.0%/4.5%
	Q^2_P(1Al)	-81.6	1.93	7.3%
	Q^2_B(0Al)	-82.8	1.96	19.6%
	Q^2_P(0Al)	-85.3	2.26	39.7%
	Q^3(1Al)	-87.7	2.25	7.4%

The ^{29}Si spectra for CASH_DR_1.0B, presented in Figure 38 and peak properties in Table 9, indicates C-A-S-H with some alumina/silica gel present. The Q^3(*m*Al) connectivity may be in the C-A-S-H or the alumina/silica gel. CASH_DR_1.3B, presented in Figure 39 and peak properties in Table 8, has a C-A-S-H structure with some Q^3(*m*Al) connectivity associated with crosslinking of the C-A-S-H. CASH_DR_1.5B, presented in Figure 40 and peak properties in Table 8, has a C-A-S-H structure with crosslinking through alumina bridging tetrahedra and some alumina in the pairing tetrahedra, as evidenced by the presence of a Q^3(1Al) and Q^1(1Al) peak, respectively. A schematic of this environment is shown in Figure 41.

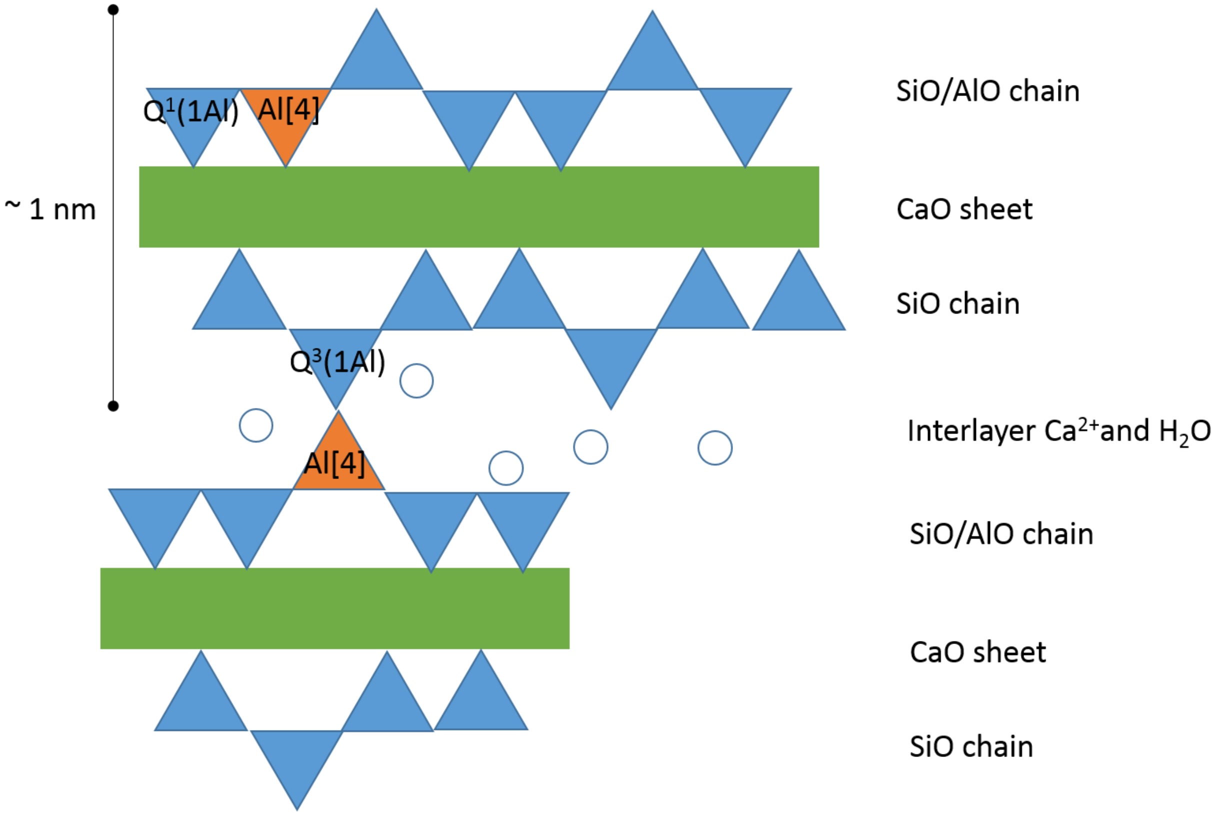

Figure 41: Molecular structure of C-A-S-H with Al[4] in the pairing tetrahedron and crosslinking bridging tetrahedron.

Consequently, a Q^2_B(1Al) environment is highly likely to exist if a Q^1(1Al) environment exists and the proportion of Q^2_B(1Al) must equal to or greater than Q^1(1Al), for the same reasons stated previously. For the purposes of this study, they are assumed to be equal. The Q^2_B(1Al) and Q^1(0Al) peak overlap and are not possible to differentiate by means of deconvolution, thus the proportion of Q^1(0Al) and Q^2_B(1Al) were found by subtracting the area of the peak at -76.9 ppm from the area of the peak at -79.4 ppm. All samples have similar amounts of alumina in the C-A-S-H, as evidenced by the proportion of

Q^2_P(1Al) and Q^1(1Al). The quantity of Q^1(*m*Al) peaks increases with the starting Ca/Si ratio, indicating a decrease in MCL with increasing Ca/Si.

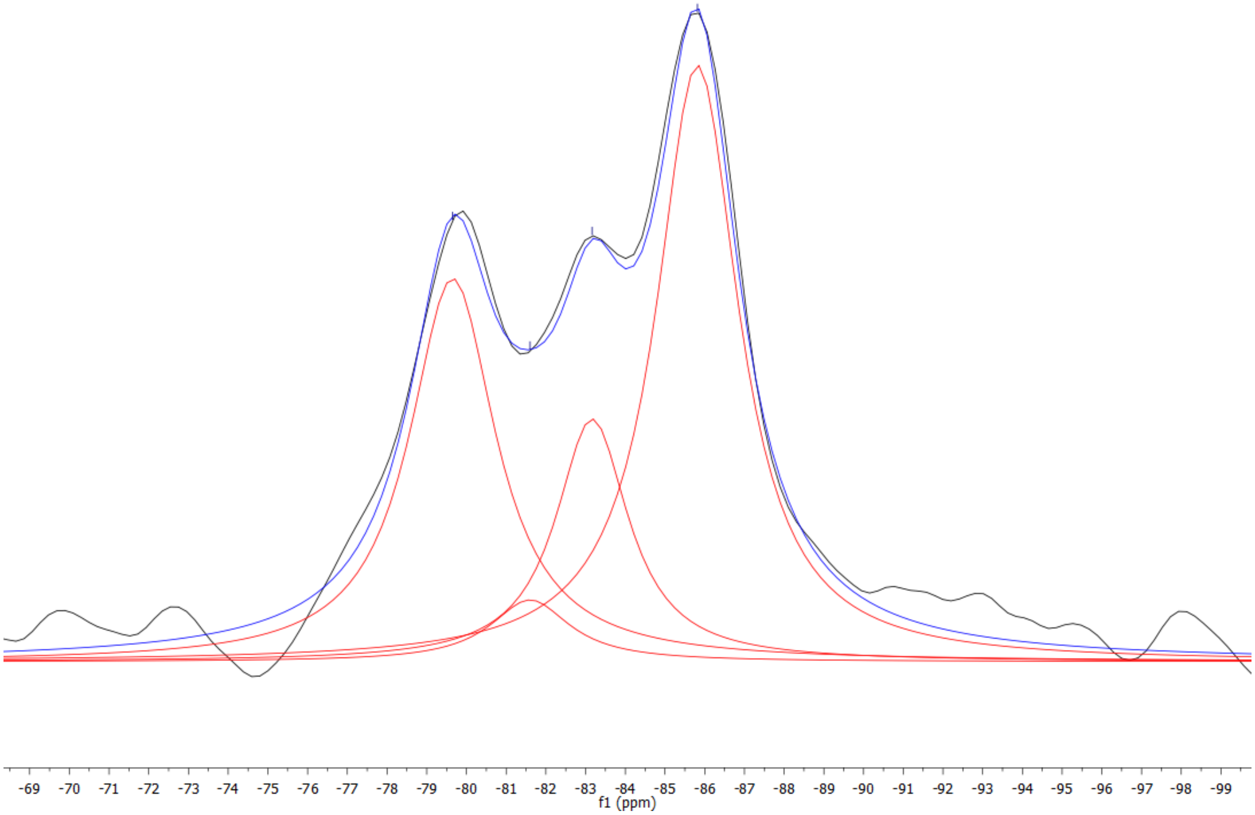

Figure 42: ^{29}Si NMR spectrum of CASH_DR_1.7L.

Table 10: Deconvolution peak properties for CASH_DR_1.7L.

	Q^n(*mAl*)	Chemical shift (ppm)	Width (ppm)	Proportion
CASH_DR_1.7L	Q^1(0Al)	-79.7	2.63	31.6%
	Q^2_P(1Al)	-81.6	2.41	4.7%
	Q^2_B(0Al)	-83.2	2.21	16.8%
	Q^2_P(0Al)	-85.8	2.51	46.9%

The ^{29}Si spectrum for CASH_DR_1.7L, presented in Figure 42 and peak properties in Table 10, indicates C-A-S-H with a larger proportion of Q^1(0Al) than other samples, resulting in a shorter MCL.

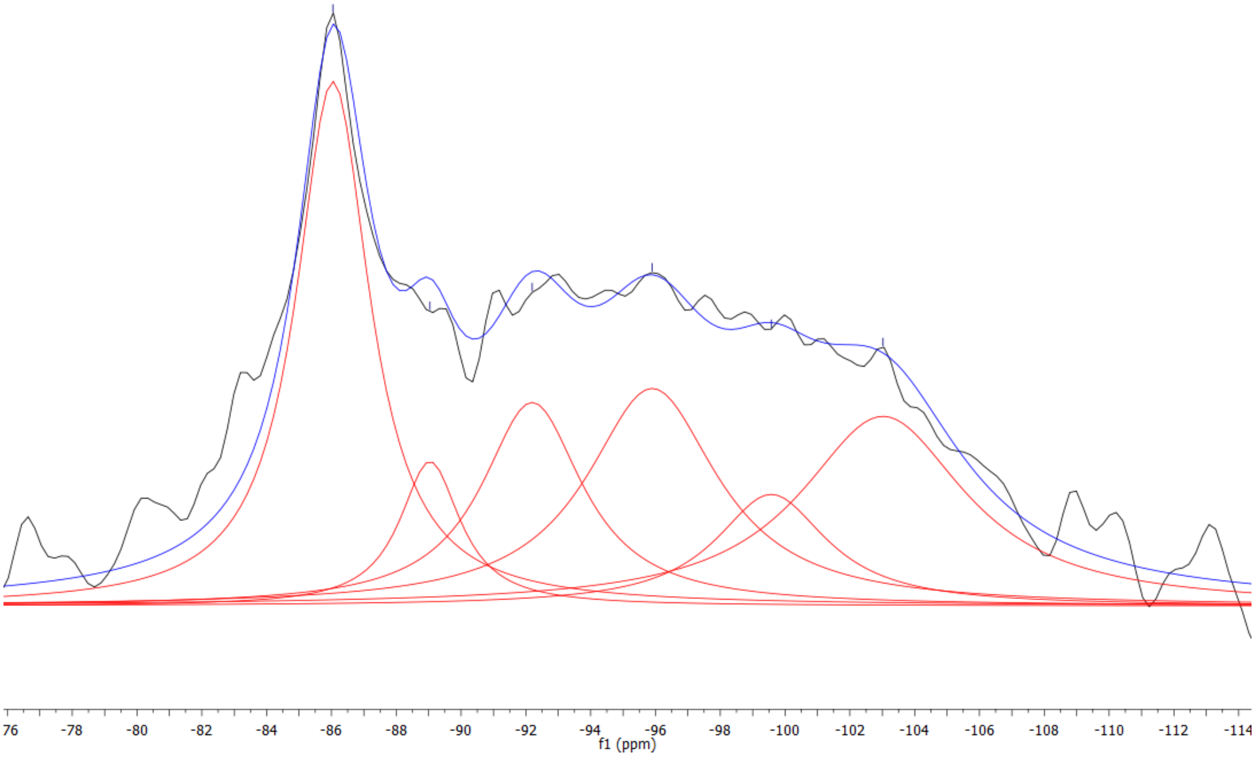

Figure 43: ^{29}Si NMR spectrum of CASH_DR_0.9H.

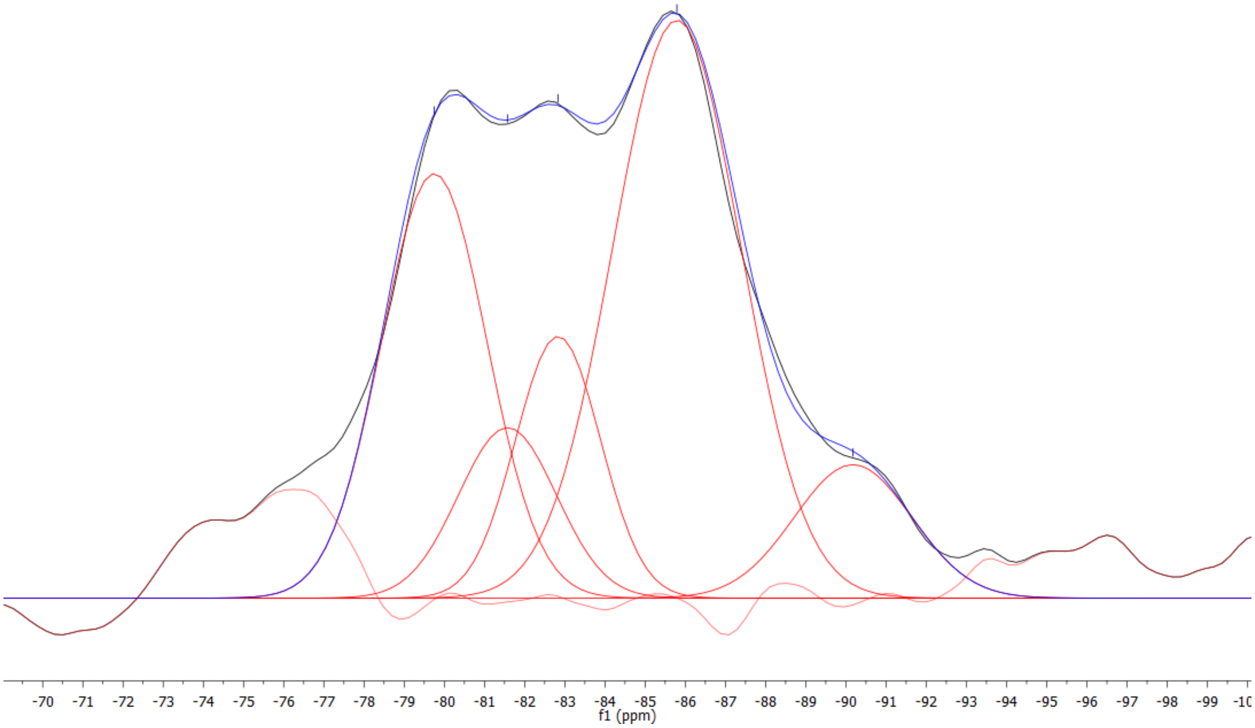

Figure 44: ^{29}Si NMR spectrum of CASH_DR_1.7H.

Table 11: Deconvolution peak properties for CASH_DR_0.9H and CASH_DR_1.7H.

	Q^n(*mAl*)	Chemical shift (ppm)	Width (ppm)	Proportion
CASH_DR_0.9H	Q^4(3Al)	-86	2.75	27.5%
	Q^3(1Al)	-89	2.26	6.2%
	Q^3(0Al)	-92.2	3.79	14.7%
	Q^4(2Al)	-95.9	4.91	20.3%
	Q^4(1Al)	-99.6	4.17	8.9%
	Q^4(0Al)	-103	6.22	22.4%
CASH_DR_1.7H	Q^1(0Al)	-79.7	3.08	25.7%
	Q^2_P(1Al)	-81.6	2.87	9.6%
	Q^2_B(0Al)	-82.8	2.48	12.8%
	Q^2_P(0Al)	-85.8	3.77	42.8%
	Q^3(1Al)	-90.2	3.44	9.0%

The ^{29}Si spectrum for CASH_DR_0.9H, presented in Figure 43 and peak properties in Table 11, indicates that the sample is entirely alumina/silica gel, due to the lack of Q^1 and Q^2 peaks. The signal/noise ratio of this spectrum is quite low, compared to other spectra. CASH_DR_1.7H, presented in Figure 44 and peak properties in Table 11, is typical of a C-A-S-H with a modest amount of crosslinking through alumina in the bridging tetrahedra.

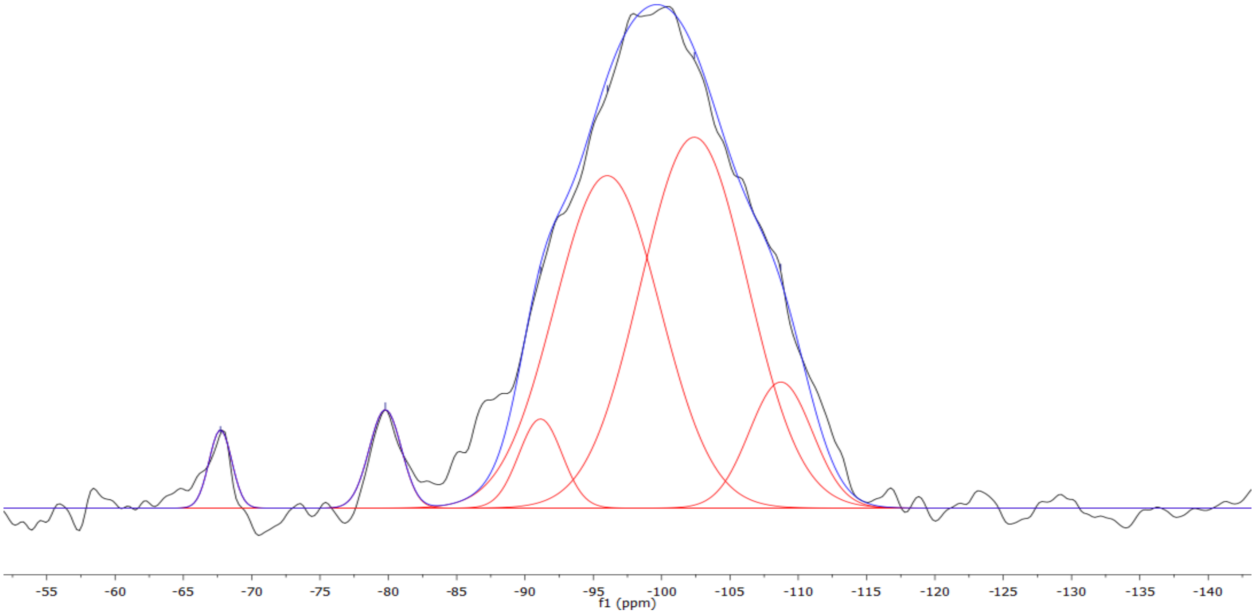

Figure 45: ^{29}Si NMR spectrum of CASH_DR_1.0C.

Table 12: Deconvolution peak properties for CASH_DR_1.0C.

	Q^n(*mAl*)	Chemical shift (ppm)	Width (ppm)	Proportion
CASH_DR_1.0C	Q^0	-67.7	1.94	1.9%
	Q^4(4Al)	-79.8	2.77	3.5%
	Q^3(0Al)	-91.1	3.72	4.2%
	Q^4(2Al)	-96	9.07	38.3%
	Q^4(0Al)	-102.4	9.20	43.4%
	Q^4(0Al)	-108.7	5.43	8.7%

The ^{29}Si spectrum of CASH_DR_1.0C, presented in Figure 45 and peak properties in Table 12, is entirely alumina/silica gel, as evidenced by the large amounts of Q^4(*m*Al) present. This is confirmed by XRD, which showed only an amorphous hump. A small peak at -67.7 ppm exists, which can be attributed to Q^0, or a monomer silica tetrahedra [24]. The presence of the Q^0 peak is odd and is typically not observed in C-S-H, but is observed in portland cement.

4.2.5 CARBONATION TREATMENT OF C-S-H

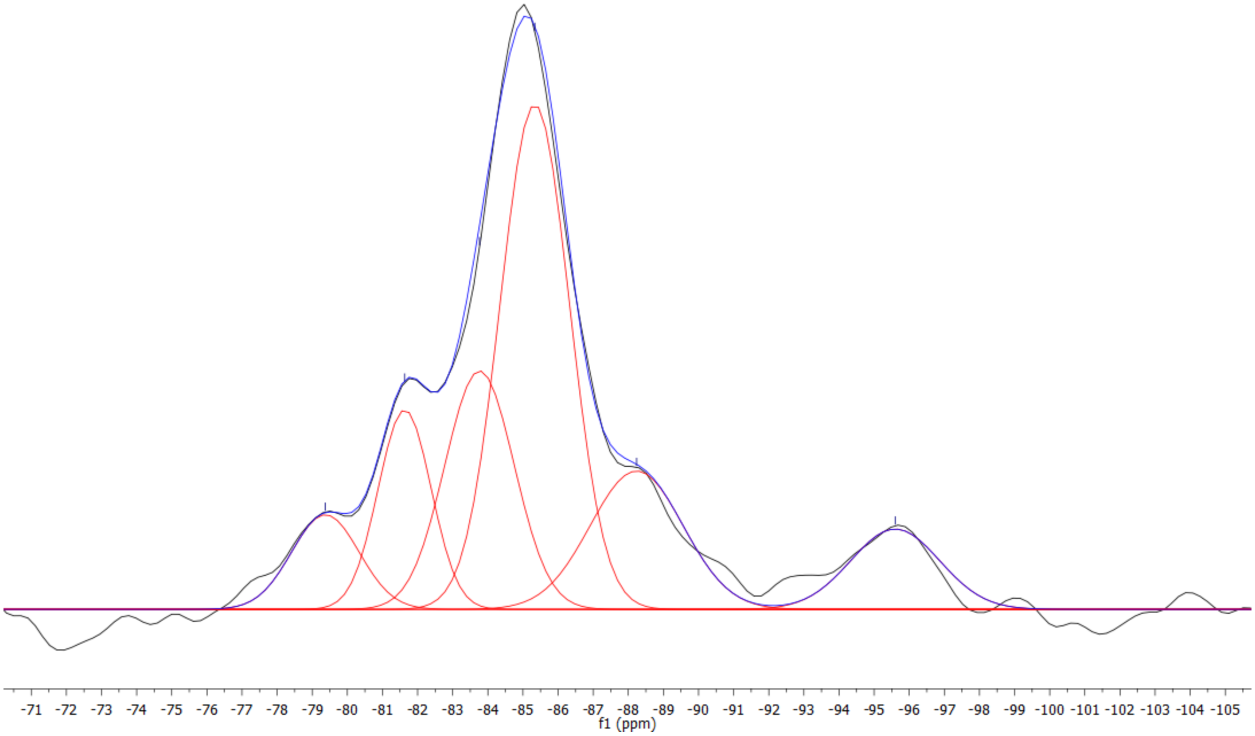

Figure 46: ^{29}Si NMR spectrum of CSH_DR_1.3A_NaNO3.

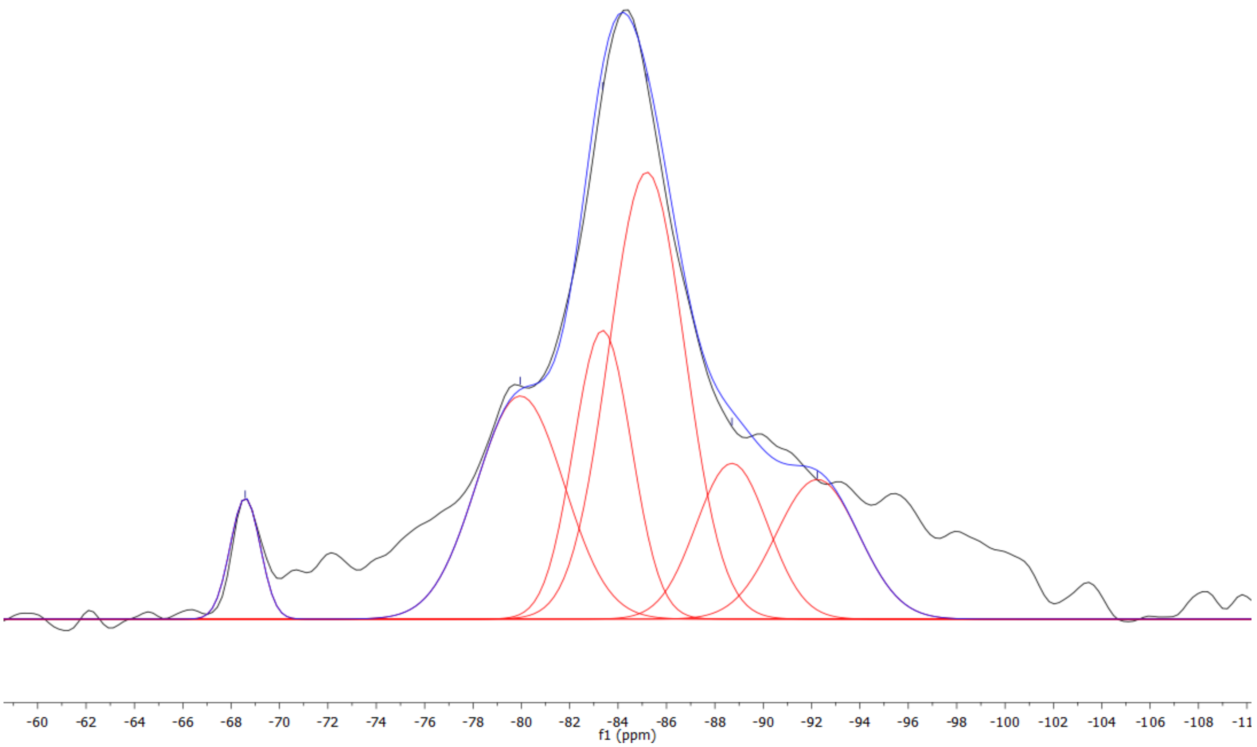

Figure 47: ^{29}Si NMR spectrum of CSH_DR_13A_NaOH.

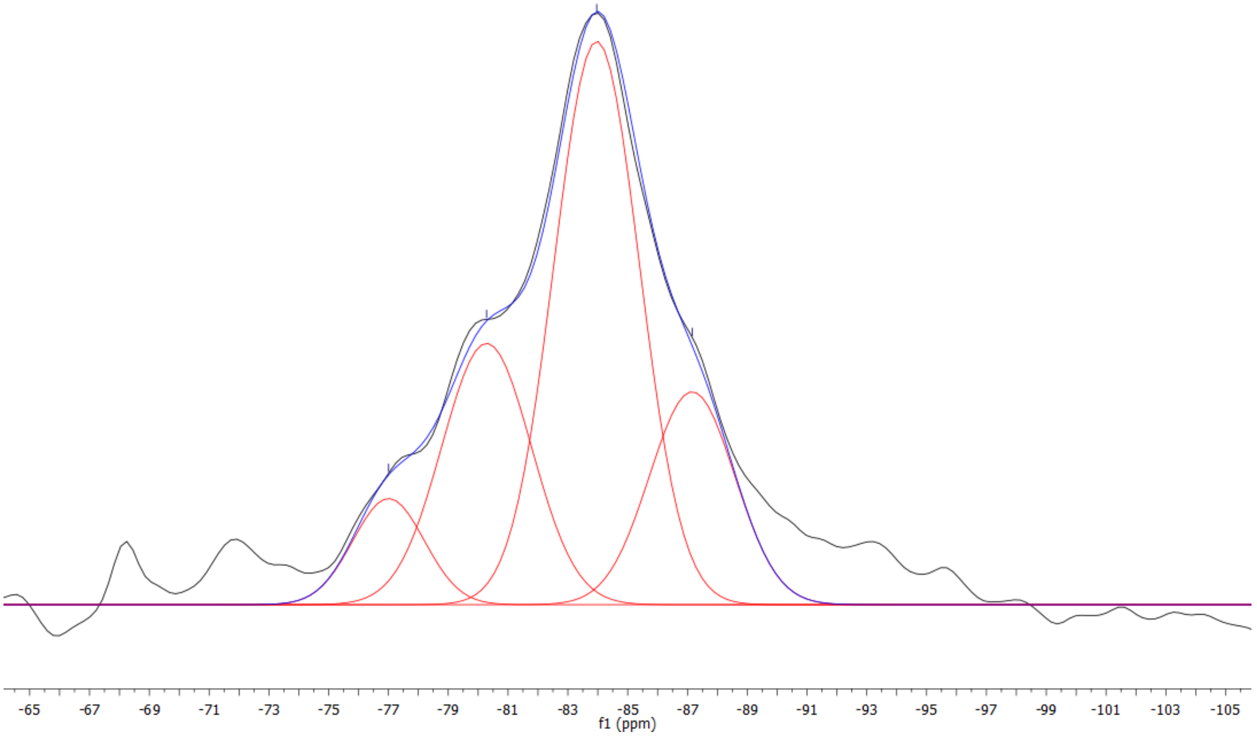

Figure 48: ^{29}Si NMR spectrum of CSH_DR_13A_KOH.

Table 13: Deconvolution peak properties for CSH_DR_1.3A_NaNO3, CSH_DR_1.3A_NaOH, and CSH_DR_1.3A_KOH.

	$Q^n(m\mathrm{Al})$	ppm	Width (ppm)	Proportion
CSH_DR_1.3A_NaNO3	Q^1(0Al)	-79.4	2.26	7.2%
	Q^2_B(0Al)?	-81.6	1.78	11.9%
	Q^2_B(0Al)	-83.8	2.33	18.7%
	Q^2_P(0Al)	-85.3	2.33	39.6%
	Q^3(0Al)	-88.2	3.10	14.5%
	Q^3(0Al)	-95.6	2.98	8.1%
CSH_DR_1.3A_NaOH	Q^0	-68.6	1.46	3.8%
	Q^1(0Al)	-80.0	4.26	20.3%
	Q^2_B(0Al)	-83.4	2.80	17.2%
	Q^2_P(0Al)	-85.2	3.69	35.2%
	Q^3(0Al)	-88.7	3.49	11.6%
	Q^3(0Al)	-92.2	4.02	12.0%
CSH_DR_1.3A_KOH	Q^1(0Al)	-77.0	2.80	7.8%
	Q^2_B(0Al)	-80.3	3.52	24.1%
	Q^2_P(0Al)	-84.0	3.35	49.5%
	Q^3(0Al)	-87.2	3.35	18.7%

The ^{29}Si spectrum for CSH_DR_1.3A_NaNO3, presented in Figure 46 and peak properties in Table 13, is comprised of mostly C-S-H peaks with a some Q^3(0Al). Both Q^3(0Al) peaks are attributed to crosslinking the C-S-H. It is presumed that the more upfield peak is also bonded to sodium, resulting in more chemical shielding. The Q^2 environment is the dominant chemical environment. The peak at -81.6 is of unknown origin. The peak position would indicate a Q^2_P(1Al) peak, but no aluminum is present in this system. It is more likely that this peak comes from a Q^2_B(0Al) site that is charge balanced by sodium instead of calcium, which would push the peak downfield from the -83.8 ppm position, which is charge balanced by calcium. The ^{29}Si spectrum of

CSH_DR_1.3A_NaOH, presented in Figure 47 and peak properties in Table 13, has a small peak attributed to Q^0 that is close to the noise level. Additionally, a C-S-H dreierketten structure with cross-linking is observed. Both Q^3(0Al) peaks are attributed to crosslinking the C-S-H. It is presumed that the more upfield peak is also bonded to sodium, resulting in more chemical shielding. This sample has a higher proportion of Q^1(0Al) than the other samples. The ^{29}Si spectrum for CSH_DR_1.3A_KOH, presented in Figure 48 and peak properties in Table 13, has peaks with chemical shifts that are less negative than previously seen. However, it is believed that these peaks still represent C-S-H since it is observed in the XRD patterns. All four peaks are shifted roughly 2 ppm downfield indicating that there is a universal change in the system, which may be caused by the potassium or a referencing error in the NMR analysis. The Q^3(0Al) peak is attributed to cross-linking in the C-S-H.

4.3 ^{27}Al NMR

4.3.1 C-A-S-H SYNTHESIZED BY DOUBLE DECOMPOSITION

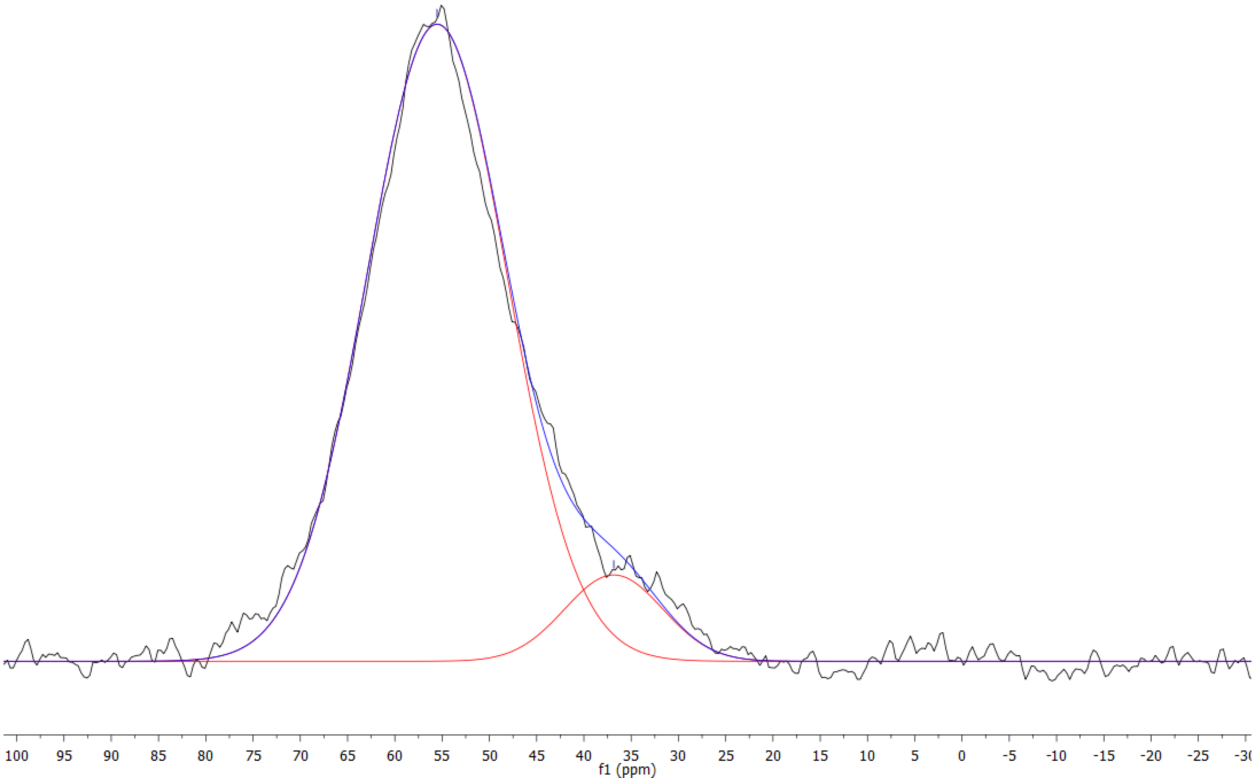

Figure 49: ^{27}Al NMR spectrum of CASH_DD_0.8B.

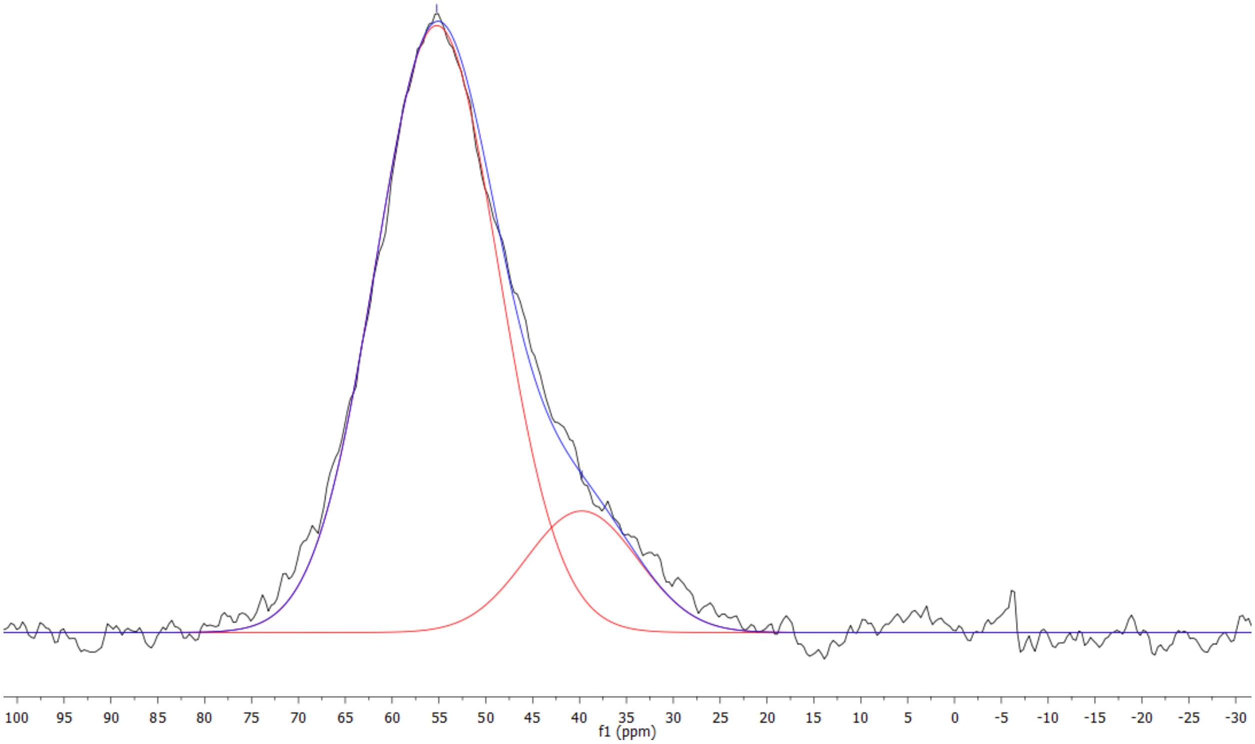

Figure 50: ^{27}Al NMR spectrum of CASH_DD_0.9B.

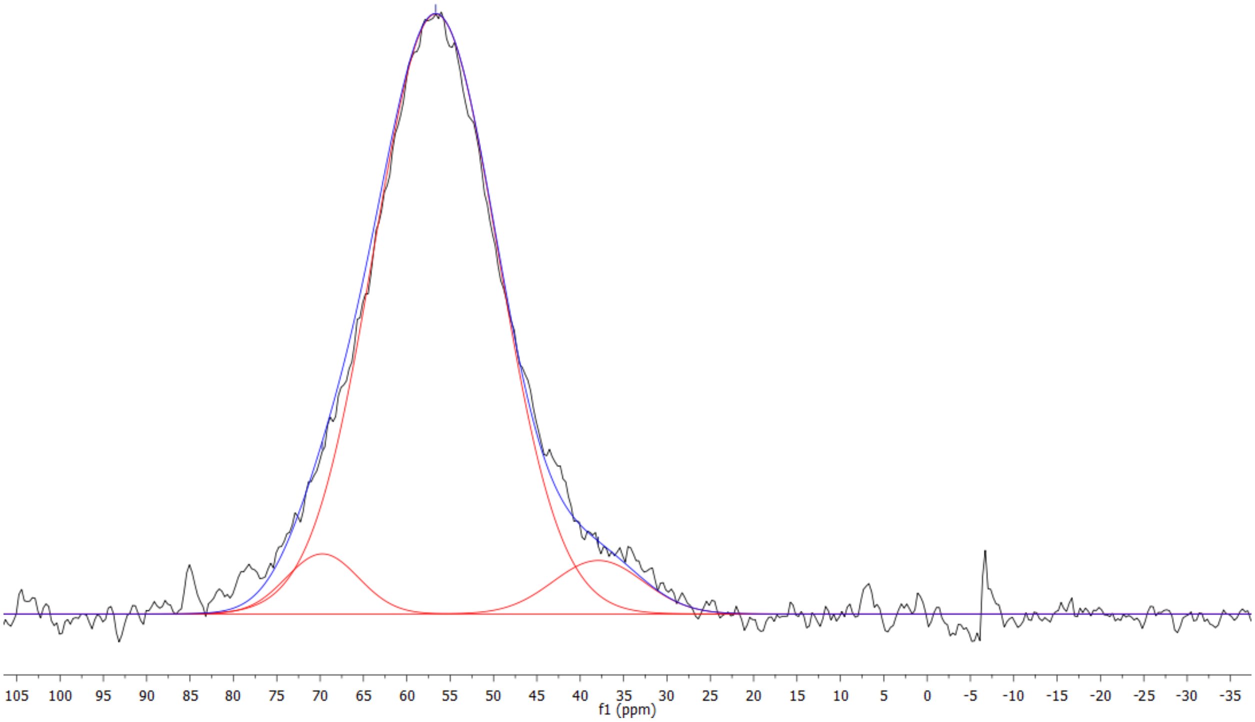

Figure 51: ^{27}Al NMR spectrum of CASH_DD_1.1B.

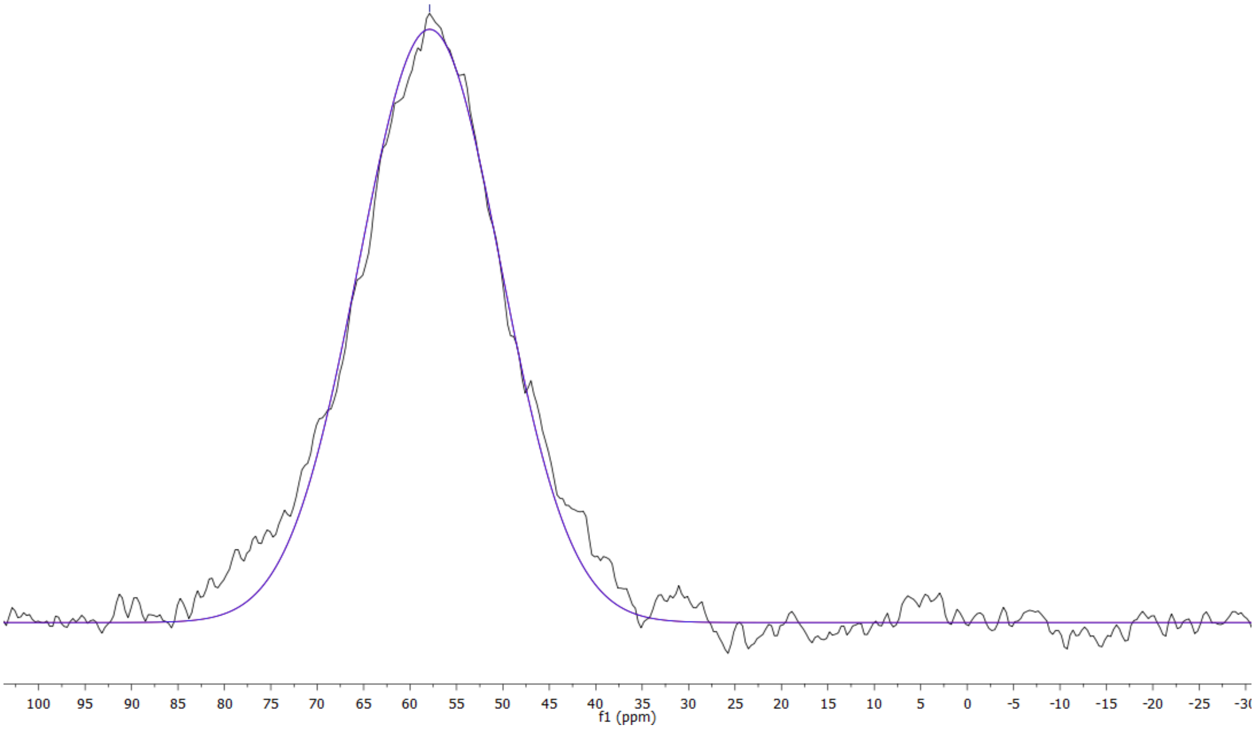

Figure 52: ^{27}Al NMR spectrum of CASH_DD_1.3B.

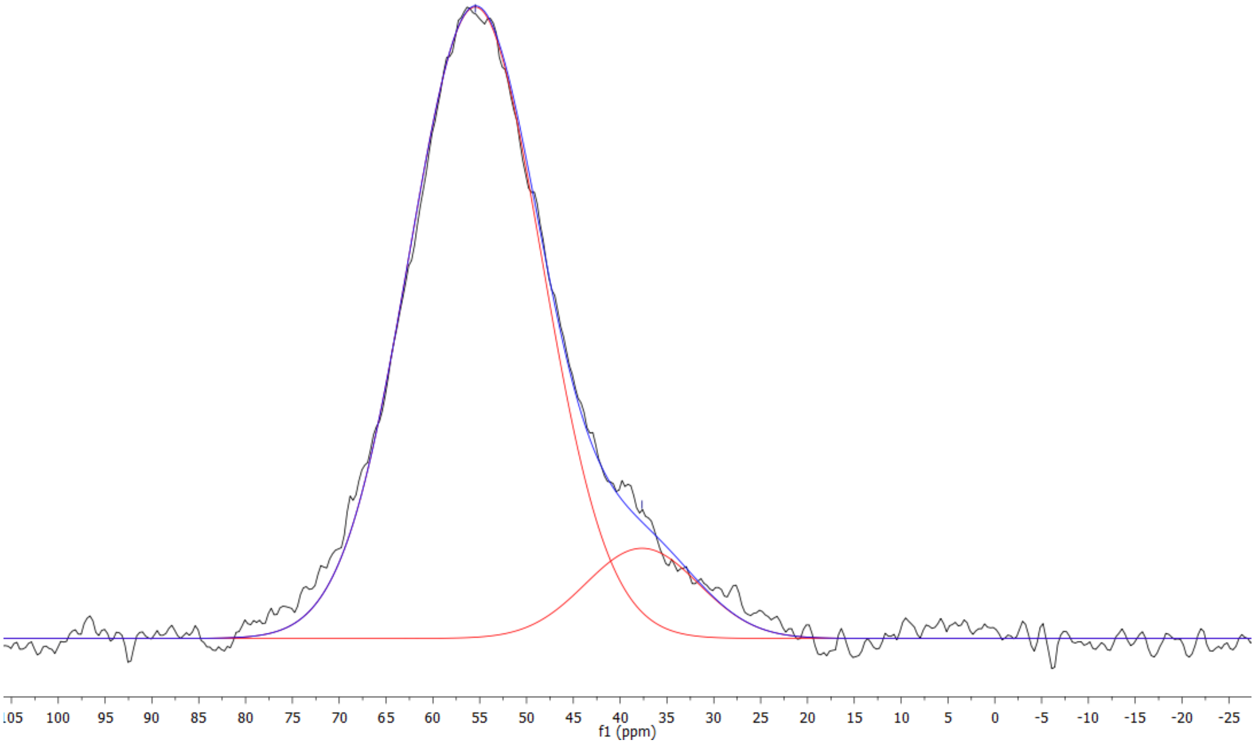

Figure 53: ^{27}Al NMR spectrum of CASH_DD_1.5B.

Table 14: Deconvolution peak properties for CASH_DD_0.8B, CASH_DD_0.9B, CASH_DD_1.1B, CASH_DD_1.3B, and CASH_DD_1.5B.

	Assignment	Chemical shift (ppm)	Width (ppm)	Proportion
CASH_DD_0.8B	Al[4]	55.5	17.46	91.3%
	Al[5]	36.8	12.20	8.7%
CASH_DD_0.9B	Al[4]	55.2	15.38	84.6%
	Al[5]	39.8	14.03	15.4%
CASH_DD_1.1B	Al[4]	69.7	9.78	5.2%
	Al[4]	56.7	16.84	89.0%
	Al[5]	37.9	12.28	5.8%
CASH_DD_1.3B	Al[4]	57.9	17.93	100.0%
CASH_DD_1.5B	Al[4]	55.5	16.62	89.1%
	Al[5]	37.7	14.22	10.9%

The ^{27}Al spectra for all samples, presented in Figures 49-53 and peak properties in Table 14, are dominated by Al[4], which occurs in the 50 to 80 ppm range [9]. CASH_DD_1.1B has an additional, small Al[4] peak that is presumed to exist due to asymmetry from the quadrupolar interactions in the ^{27}Al nucleus. Therefore, only one chemical environment is thought to exist. All samples except for CASH_DD_1.3B also contained an Al[5] peak, which occurs in the 15 to 40 ppm range [9]. Al[5] is presumed to occur in the interlayer spacing of the C-A-S-H [2]. The ^{29}Si results for CASH_DD_0.9B, CASH_DD_1.1B, and CASH_DD_1.3B indicate that Al[4] occurs both in the C-A-S-H and alumina/silica gel due to the $Q^2(1Al)$ peak and $Q^3/Q^4(mAl)$ peaks.

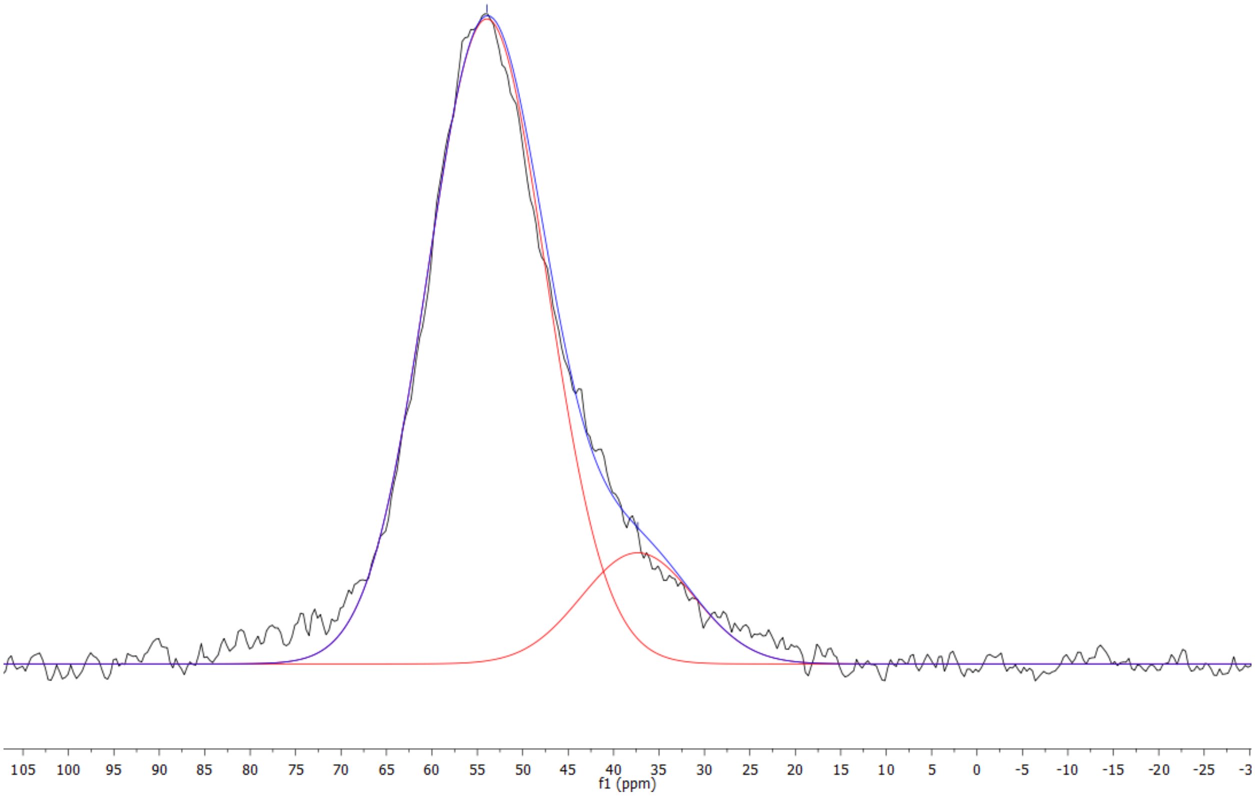

Figure 54: ^{27}Al NMR spectrum of CASH_DD_2.2H.

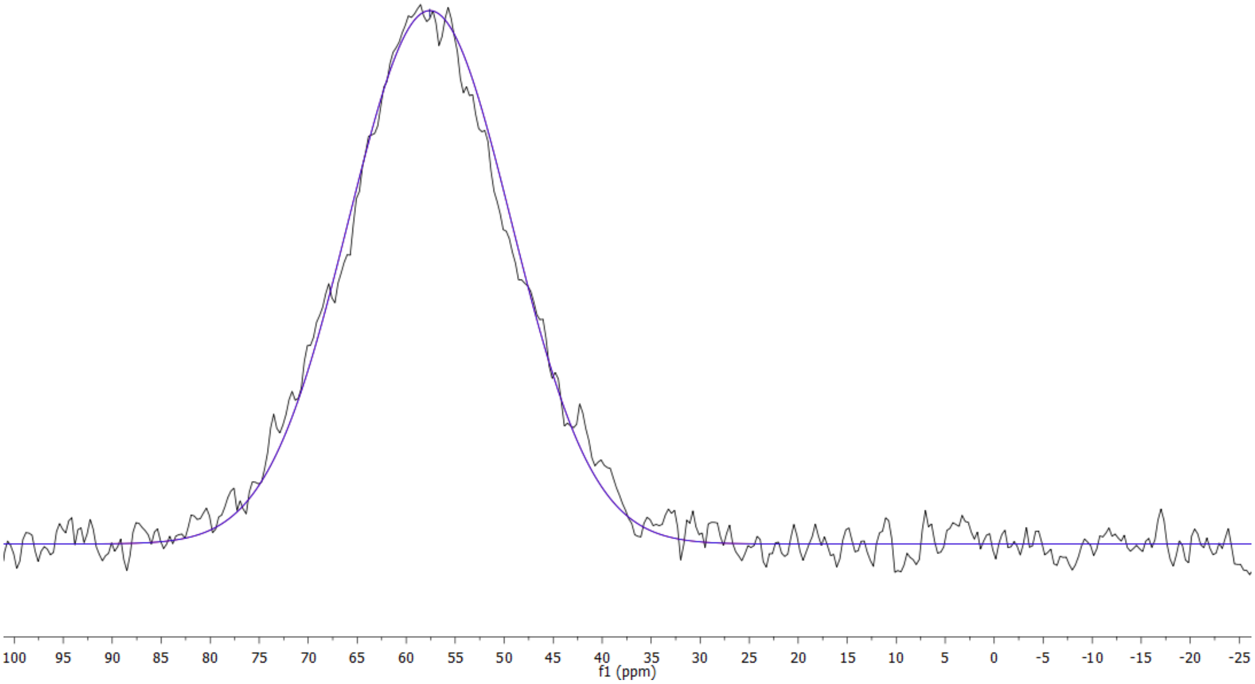

Figure 55: ^{27}Al NMR spectrum of CASH_DD_2.2L.

Table 15: Deconvolution peak properties for CASH_DD_2.2H and CASH_DD_2.2L.

	Assignment	Chemical shift (ppm)	Width (ppm)	Proportion
CASH_DD_2.2H	Al[4]	54	15.35	85.9%
	Al[5]	37.3	14.60	14.1%
CASH_DD_2.2L	Al[4]	57.6	19.54	100.0%

The ^{27}Al spectrum of CASH_DD_2.2H, presented in Figure 54 and peak properties in Table 15, contains both Al[4] and Al[5] while CASH_DD_2.2L, presented in Figure 55 and peak properties in Table 15, only contains Al[4]. The ^{29}Si spectrum for CASH_DD_2.2H is dominated by Q^4 structures and the chemical environment of the Al[5] is unknown, though it may be occurring in an alumina/silica gel. The ^{29}Si spectrum for CASH_DD_2.2L indicates that Al[4] occurs in the C-A-S-H in the bridging tetrahedra by the Q^2(1Al) peak.

4.3.2 C-A-S-H SYNTHESIZED BY DIRECT REACTION

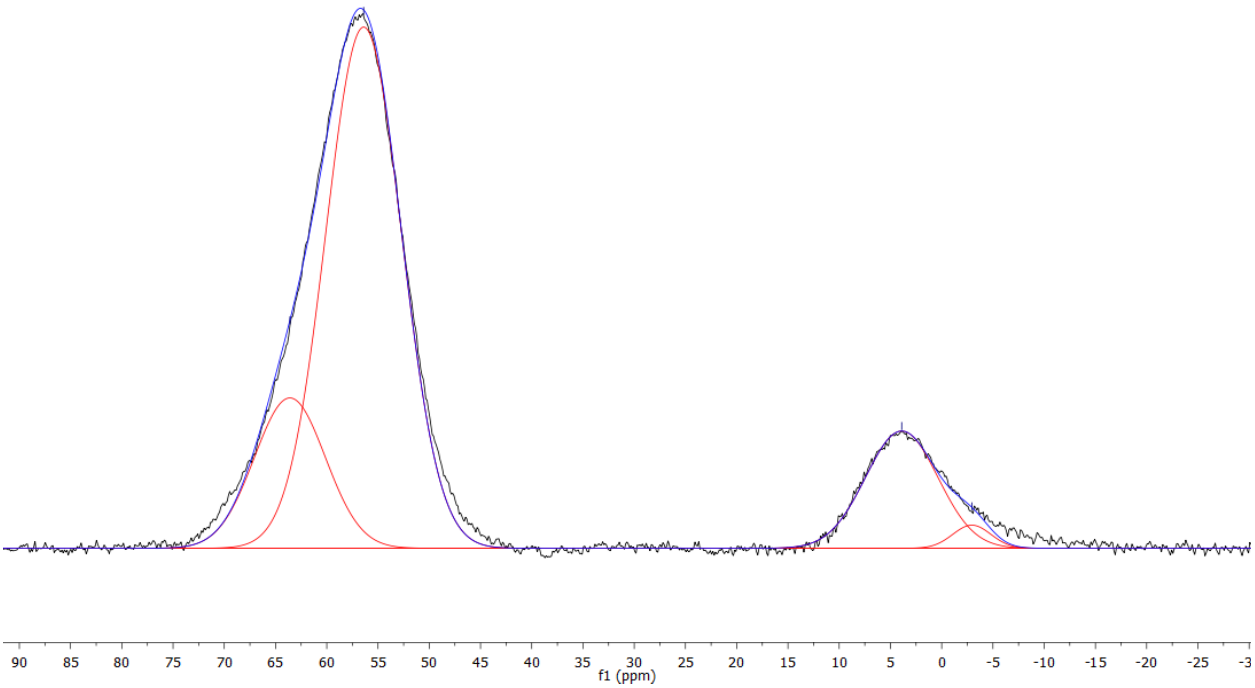

Figure 56: ^{27}Al NMR spectrum of CASH_DR_1.0A.

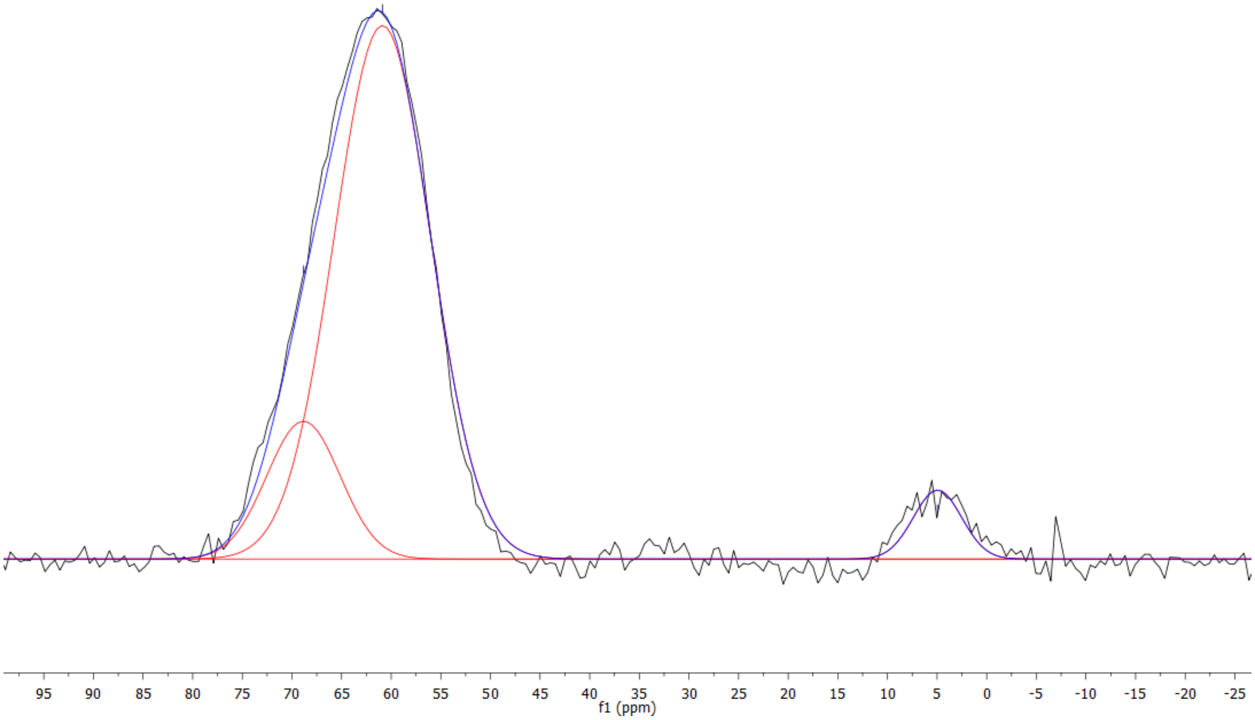

Figure 57: ^{27}Al NMR spectrum of CASH_DR_1.3A.

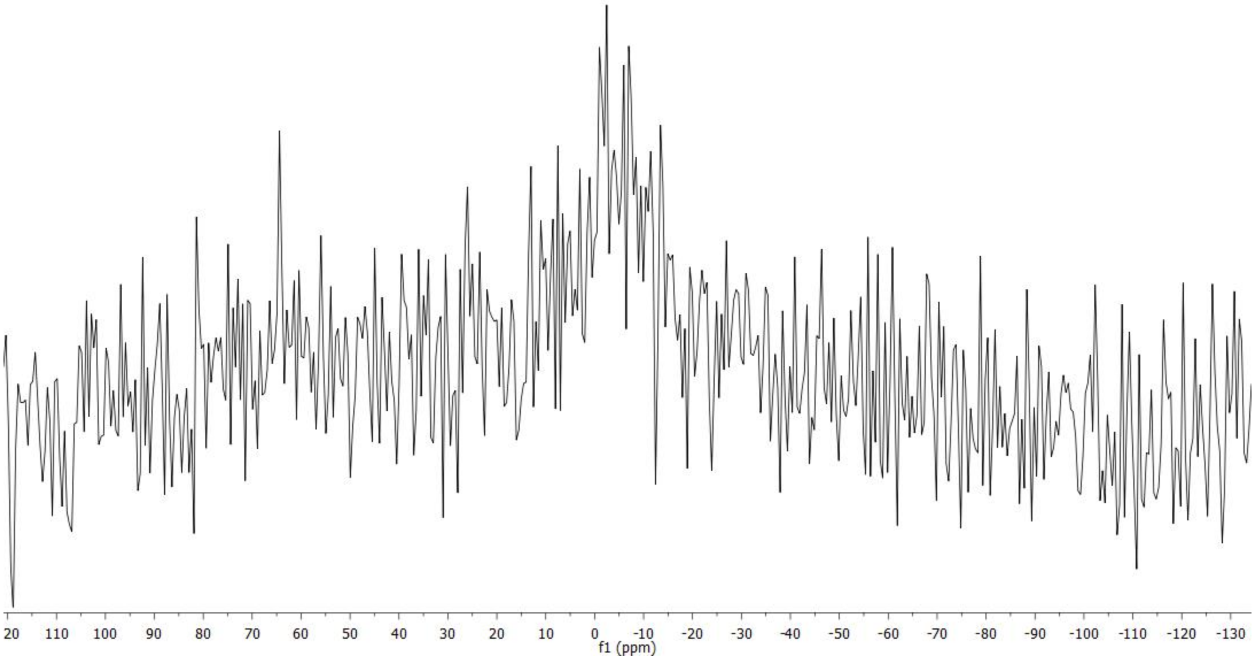

Figure 58: ^{27}Al NMR spectrum of CASH_DR_1.5A.

Table 16: Deconvolution peak properties for CASH_DR_1.0A, CASH_DR_1.3A, and CASH_DR_1.5A.

	Assignment	Chemical shift (ppm)	Width (ppm)	Proportion
CASH_DR_1.0A	Al[4]	63.6	8.14	17.9%
	Al[4]	56.4	8.70	66.3%
	Al[6]	3.9	8.32	14.3%
	Al[6]	-2.94	4.36	1.5%
CASH_DR_1.3A	Al[4]	68.8	8.71	15.6%
	Al[4]	60.9	11.44	79.3%
	Al[6]	5	5.72	5.1%
CASH_DR_1.5A	-	-	-	-

The ^{27}Al spectra for CASH_DR_1.0A, Figure 56, and CASH_DR_1.3A, Figure 57, are both predominantly Al[4] with some Al[6]. The Al[6] environment appears as signal intensity in the -20 to 20 ppm range in ^{27}Al NMR [9]. Deconvolution peak properties are presented in Table 16. The Al[6] is thought to exist in the interlayer space of the C-A-S-H and/or in alumina/silica gel. The alumina/silica gel can contain both Al[4] and Al[6] [ref 90]. The ^{29}Si spectrum for CASH_DR_1.0A indicates that aluminum is present in both the C-A-S-H and alumina/silica gel. The two Al[4] peaks may be a results of the quadrupolar interaction, or two distinct environments. Further experimental methods, such as triple-quantum ^{27}Al NMR may help elucidate this. The ^{29}Si spectrum for CASH_DR_1.3A indicates that aluminum occurs in the C-A-S-H, and exists in both Q^2_P and Q^2_B positions. It should be noted that ^{29}Si NMR is not able to detect alumina gel directly and that this phase may exist. The ^{27}Al spectrum for CASH_DR_1.5A, Figure 58, shows no intensity and no aluminum was incorporated into the structure, which is consistent with the ^{29}Si spectrum.

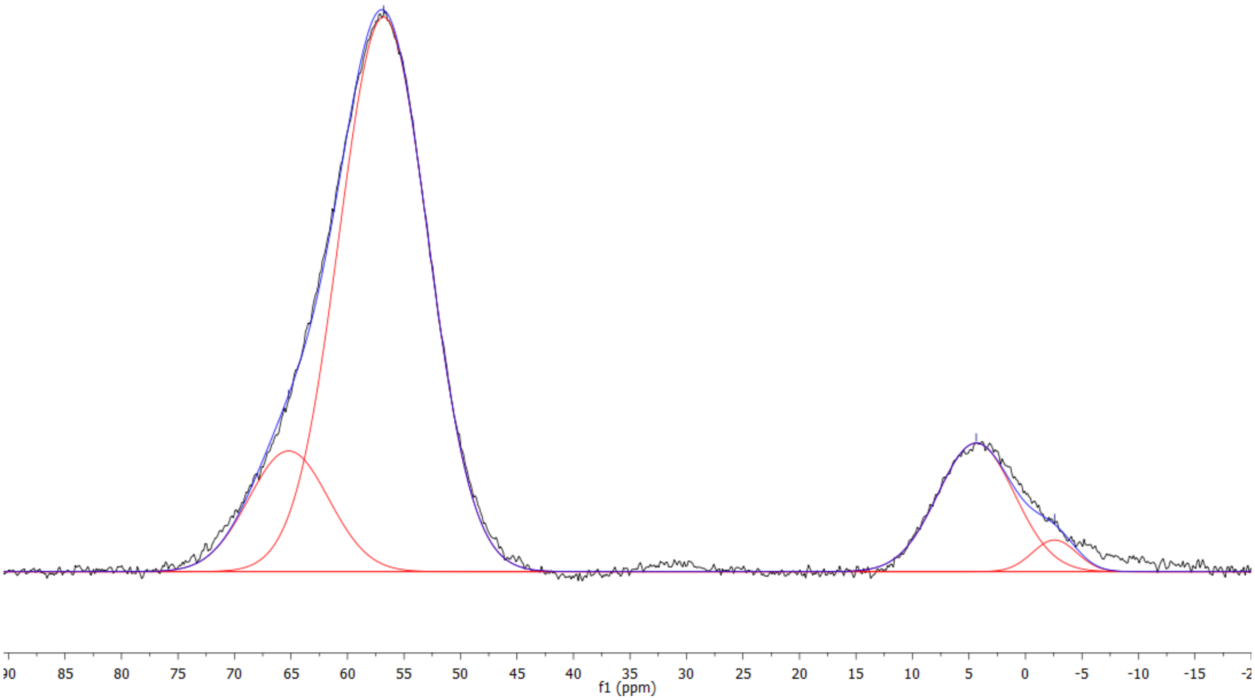

Figure 59: ^{27}Al NMR spectrum of CASH_DR_1.0B.

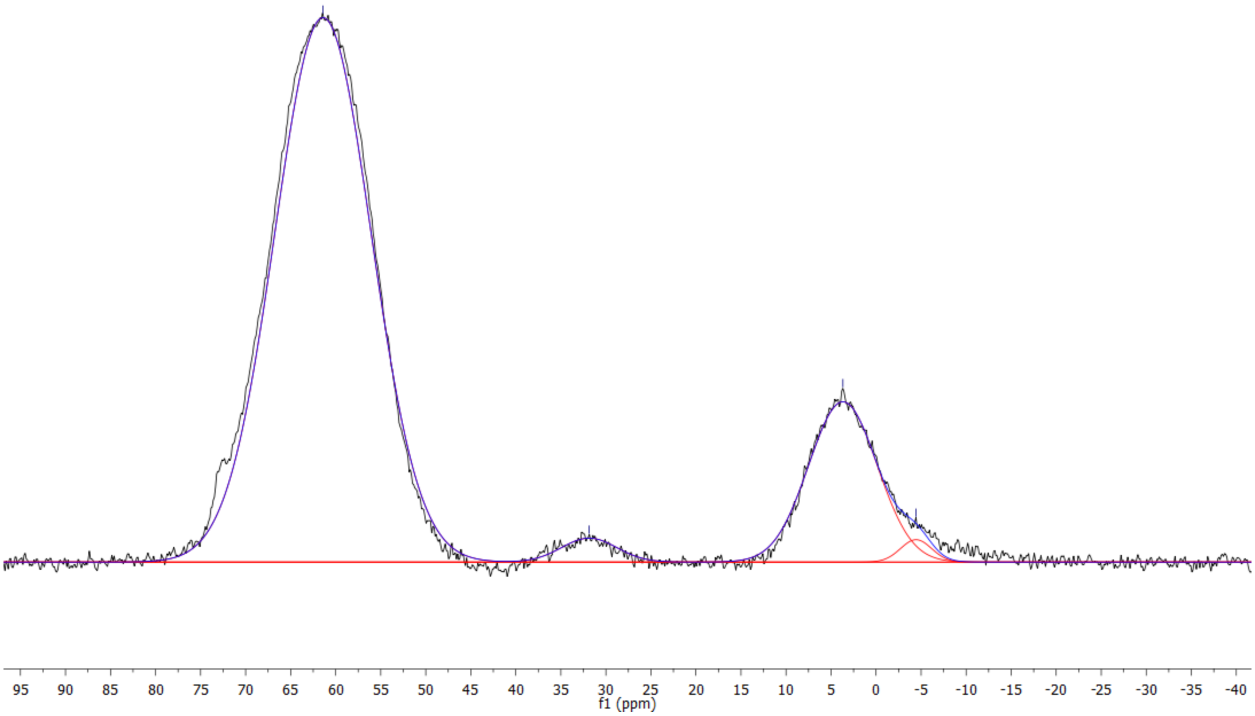

Figure 60: ^{27}Al NMR spectrum of CASH_DR_1.3B.

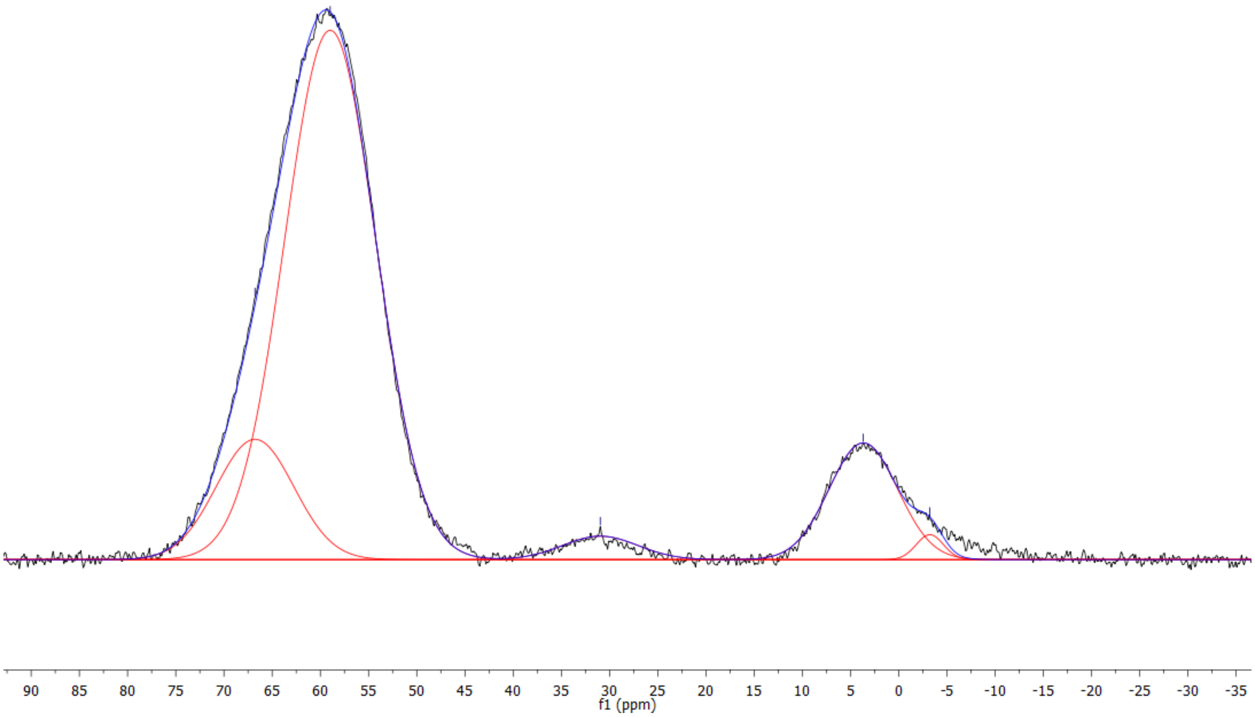

Figure 61: ^{27}Al NMR spectrum of CASH_DR_1.5B.

Table 17: Deconvolution peak properties for CASH_DR_1.0B, CASH_DR_1.3B, and CASH_DR_1.5B.

	Assignment	Chemical shift (ppm)	Width (ppm)	Proportion
CASH_DR_1.0B	Al[4]	65.21	8.32	13.7%
	Al[4]	56.81	9.25	70.2%
	Al[6]	4.36	7.97	14.0%
	Al[6]	-2.57	4.59	2.0%
CASH_DR_1.3B	Al[4]	61.41	12.56	80.1%
	Al[5]	31.85	7.23	2.0%
	Al[6]	3.68	8.94	16.8%
	Al[6]	-4.44	4.05	1.1%
CASH_DR_1.5B	Al[4]	66.78	9.50	13.8%
	Al[4]	58.98	11.10	70.9%
	Al[5]	30.96	9.18	2.6%
	Al[6]	3.67	8.37	11.8%
	Al[6]	-3.23	3.31	1.0%

The ^{27}Al spectrum for CASH_DR_1.0B, presented in Figure 59 and peak properties in Table 17, contains both Al[4] and Al[6] peaks. The smaller Al[6] peak is thought to exist due to the quadrupolar interaction of the ^{27}Al nucleus which causes asymmetry in the peak shape and can manifest itself as a false peak. Al[6] is in the interlayer space of C-A-S-H and in the alumina/silica gel identified by ^{29}Si NMR and XRD [ref 90]. The smaller Al[4] peak may be to the quadrupolar interaction, or a different chemical environment caused by the alumina/silica gel that was identified from the ^{29}Si spectrum [42]. CASH_DR_1.3B, Figure 60, and CASH_DR_1.5B, Figure 61, both are dominantly Al[4] with some Al[5] and Al[6]. The two Al[4] peaks in CASH_DR_1.5B may be due to the quadrupolar interaction or the presence of multiple Al[4] sites as identified by the ^{29}Si spectrum.

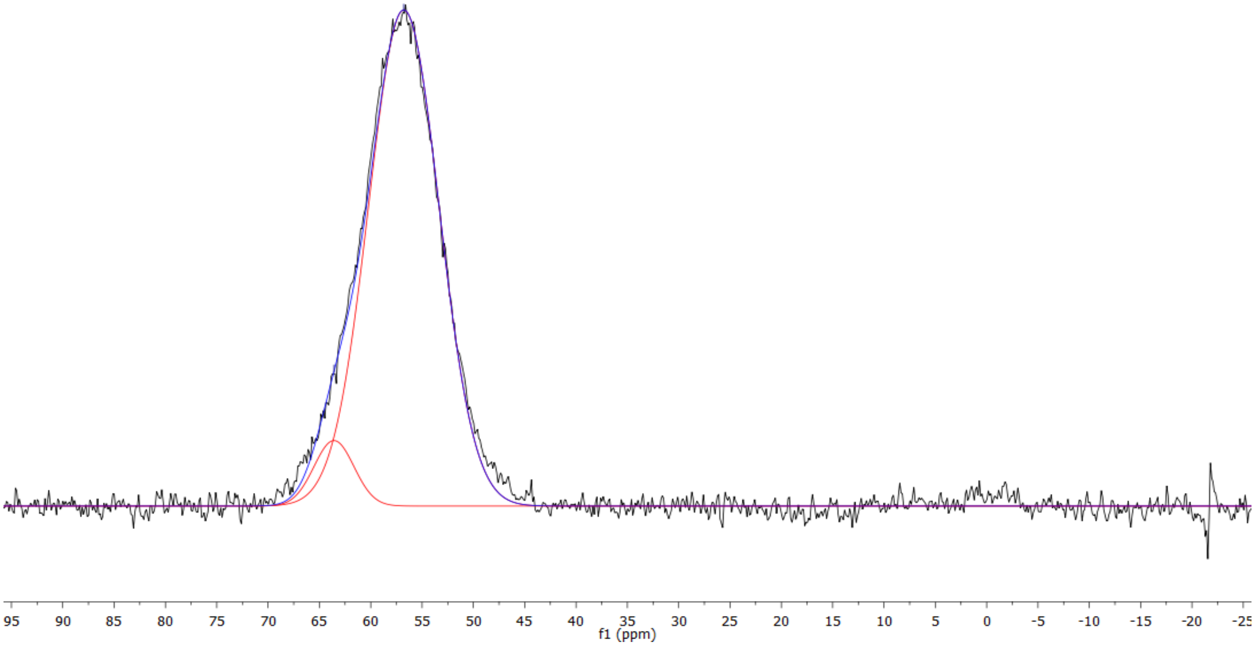

Figure 62: ^{27}Al NMR spectrum of CASH_DR_0.9L.

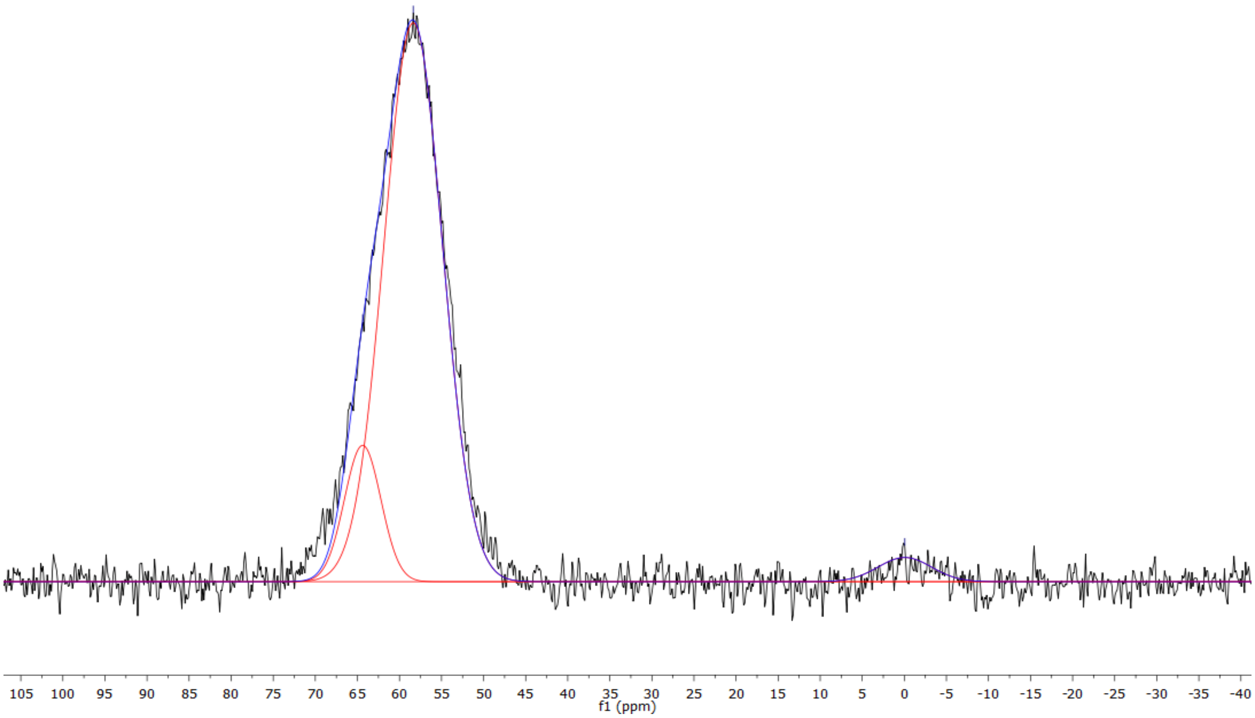

Figure 63: ^{27}Al NMR spectrum of CASH_DR_1.1L.

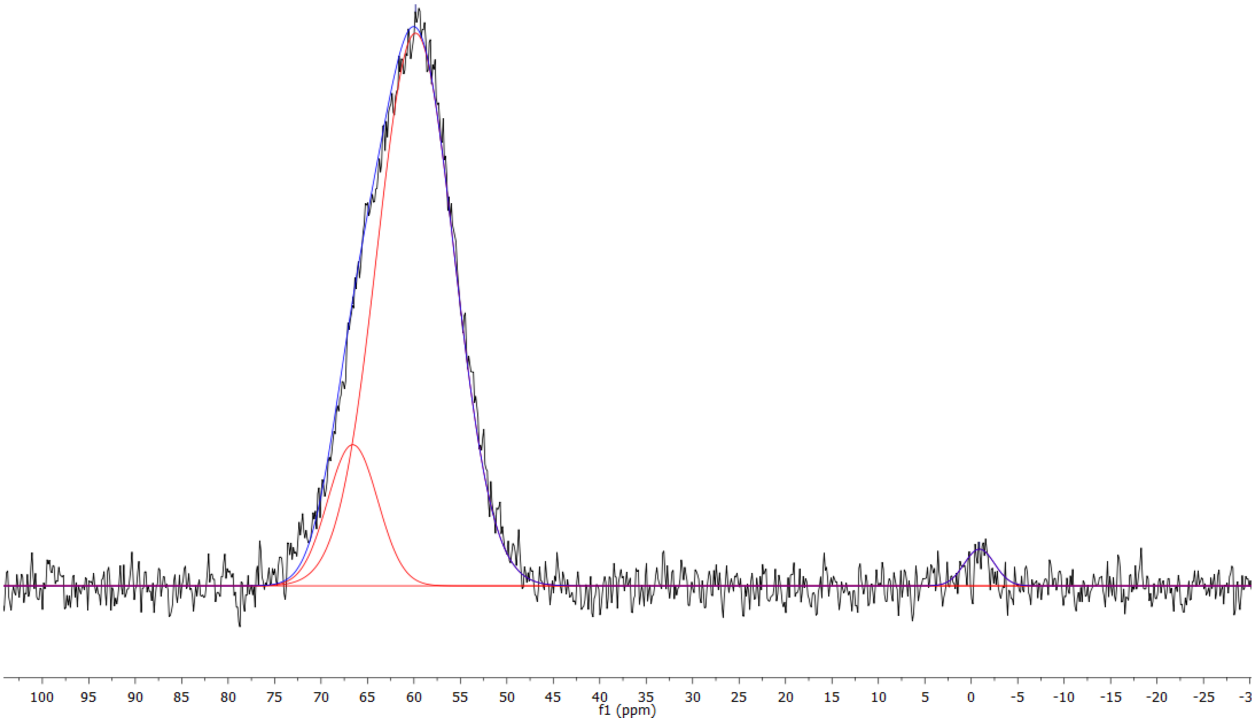

Figure 64: ^{27}Al NMR spectrum of CASH_DR_1.3L.

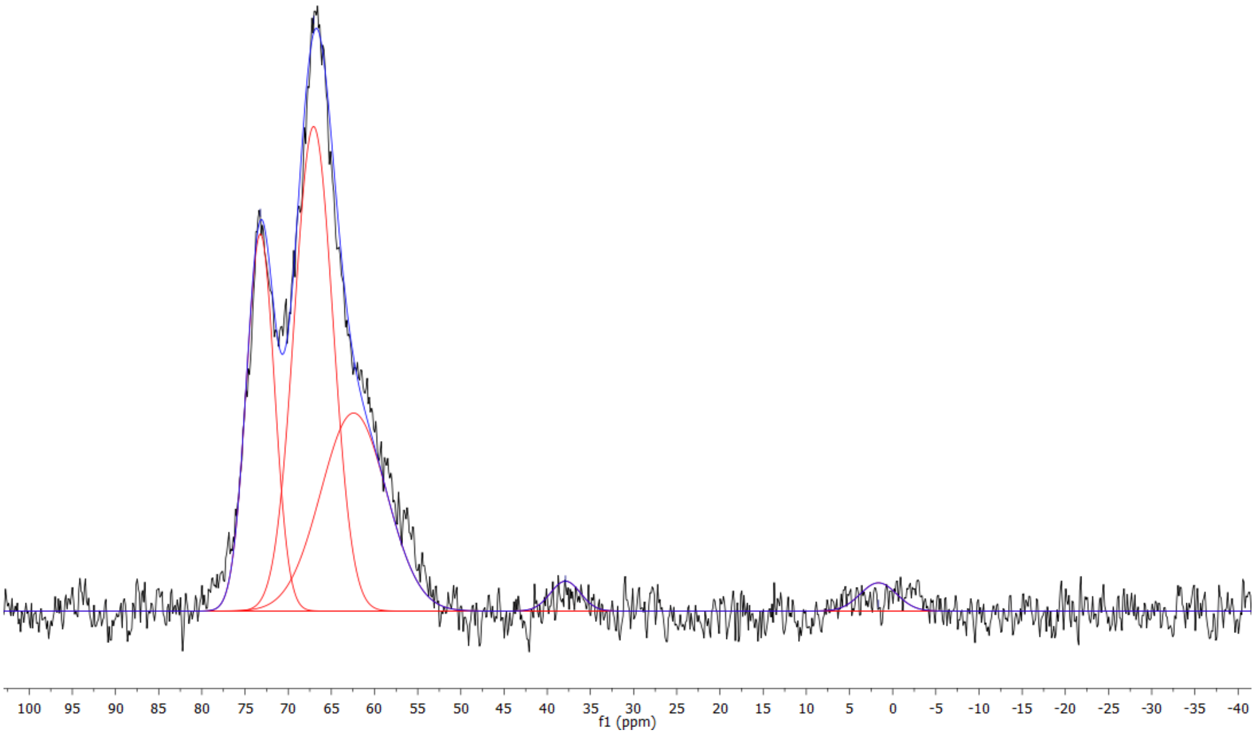

Figure 65: ^{27}*Al NMR spectrum of CASH_DR_1.5L.*

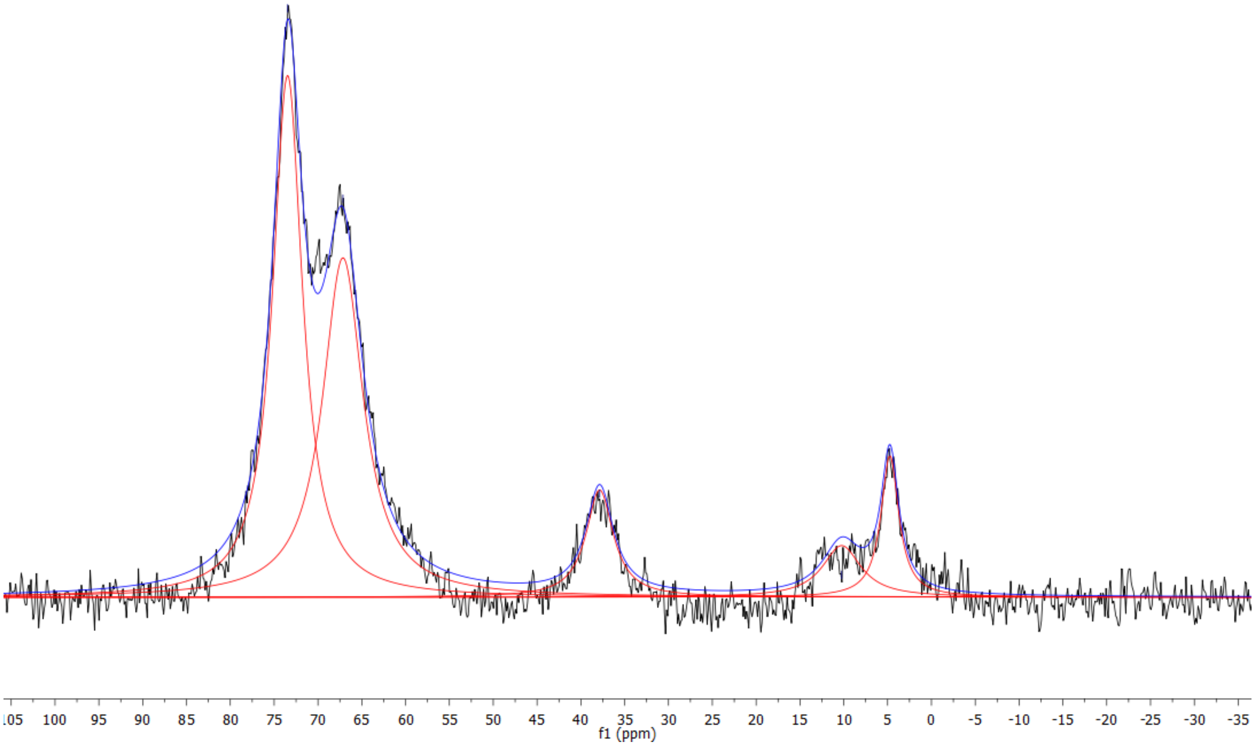

Figure 66: ^{27}*Al NMR spectrum of CASH_DR_1.7L.*

Table 18: Deconvolution peak properties for CASH_DR_0.9L, CASH_DR_1.1L, CASH_DR_1.3L, CASH_DR_1.5L, and CASH_DR_1.7L.

	Assignment	Chemical shift (ppm)	Width (ppm)	Proportion
CASH_DR_0.9L	Al[4]	63.58	4.56	6.9%
	Al[4]	56.78	8.08	93.1%
CASH_DR_1.1L	Al[4]	64.37	5.10	12.8%
	Al[4]	58.36	8.17	83.9%
	Al[6]	-0.05	7.46	3.3%
CASH_DR_1.3L	Al[4]	66.59	6.35	14.0%
	Al[4]	59.83	9.74	83.9%
	Al[6]	-0.88	3.83	2.2%
CASH_DR_1.5L	Al[4]	73.22	3.82	24.0%
	Al[4]	67.06	5.25	42.3%
	Al[4]	62.42	8.91	29.4%
	Al[5]	37.89	4.08	2.0%
	Al[6]	1.65	4.94	2.3%
CASH_DR_1.7L	Al[4]	77.95	4.01	5.8%
	Al[4]	73.46	4.12	36.9%
	Al[4]	67.52	5.61	34.1%
	Al[4]	62.92	6.43	6.5%
	Al[5]	37.86	3.77	6.5%
	Al[6]	10.24	5.36	4.5%
	Al[6]	4.74	2.47	5.6%

The ^{27}Al spectrum for all of the samples presented in Figures 62-66, and peak properties in Table 18, are Al[4] dominant. CASH_DR_1.1L, CASH_DR_1.3L, CASH_DR_1.5L, and CASH_DR_1.7L have some Al[6] present as well. CASH_DR_1.5L and CASH_DR_1.7L have Al[5]. The Al[6] and Al[5] are both thought to occur in the interlayer of the C-A-S-H. The Al[6] and Al[5] may also be in alumina/silica gel since there is evidence of carbonation from XRD. However, this cannot be stated with certainty since the only ^{29}Si spectrum available is for CASH_DR_1.7L. There are multiple, well-defined Al[4] peaks in the CASH_DR_1.5L and CASH_DR_1.7L samples. The ^{29}Si spectrum for CASH_DR_1.7L does not indicate Al[4] environments besides the bridging tetrahedra position in C-A-S-H. The XRD patterns of these samples do not indicate any crystalline phases besides $CaCO_3$ and C-A-S-H. The local atomic environment of these peaks remains unknown. However, techniques such as triple-quantum ^{27}Al NMR may prove useful.

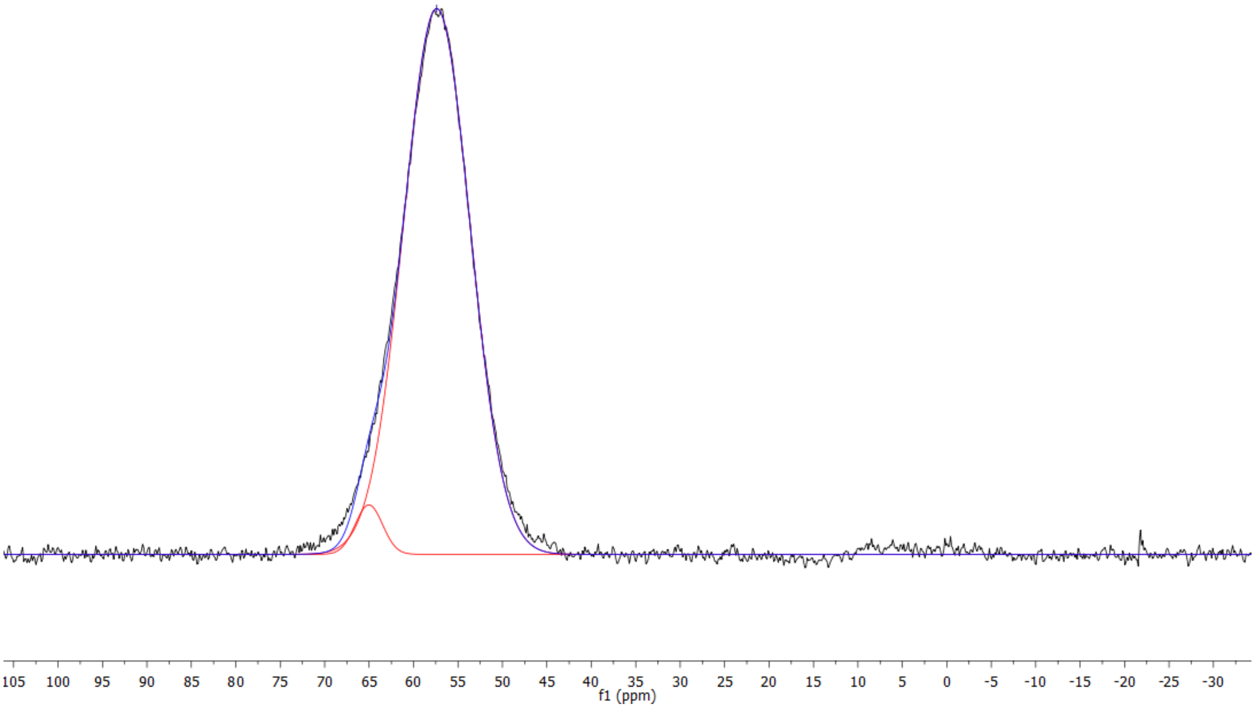

Figure 67: ^{27}Al NMR spectrum of CASH_DR_0.9H.

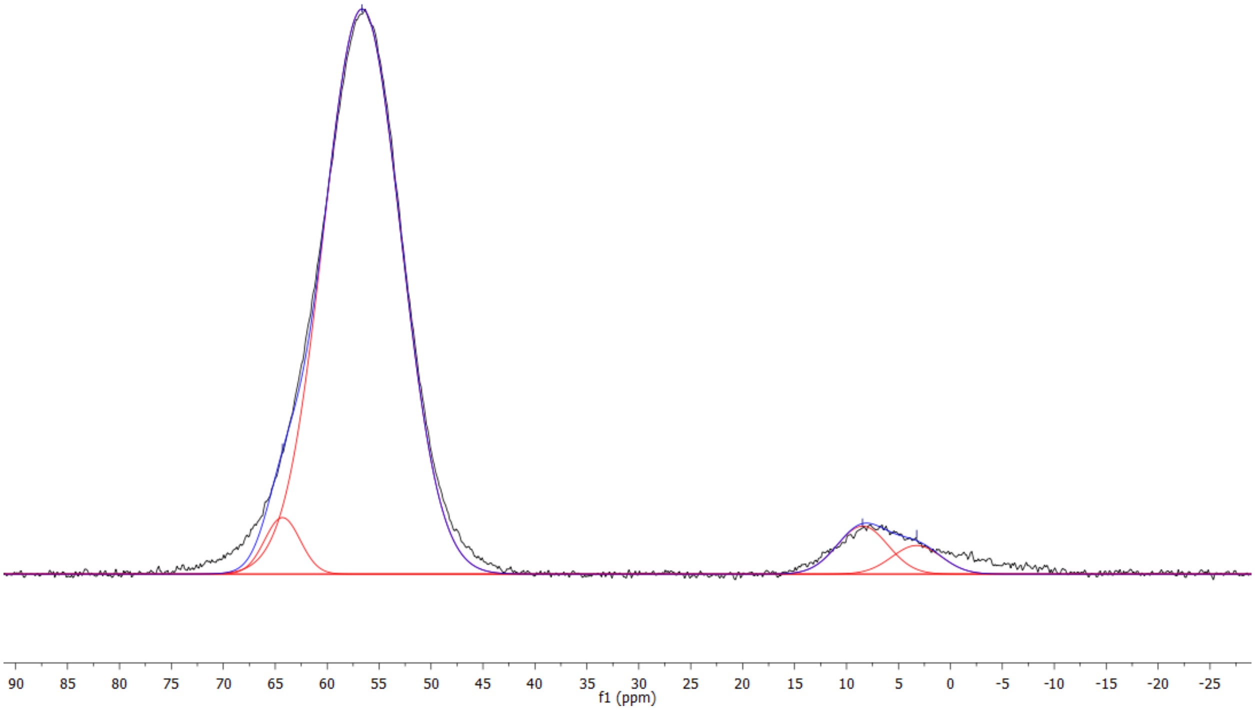

Figure 68: ^{27}Al NMR spectrum of CASH_DR_1.1H.

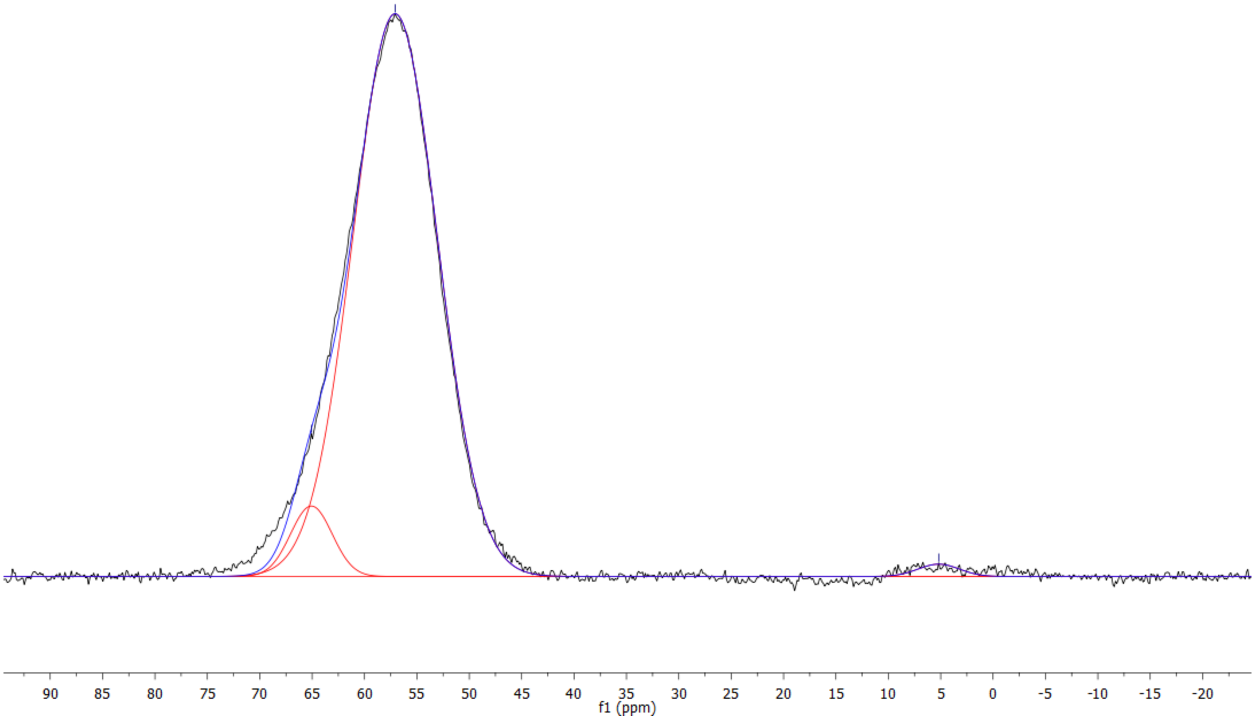

Figure 69: ^{27}Al NMR spectrum of CASH_DR_1.3H.

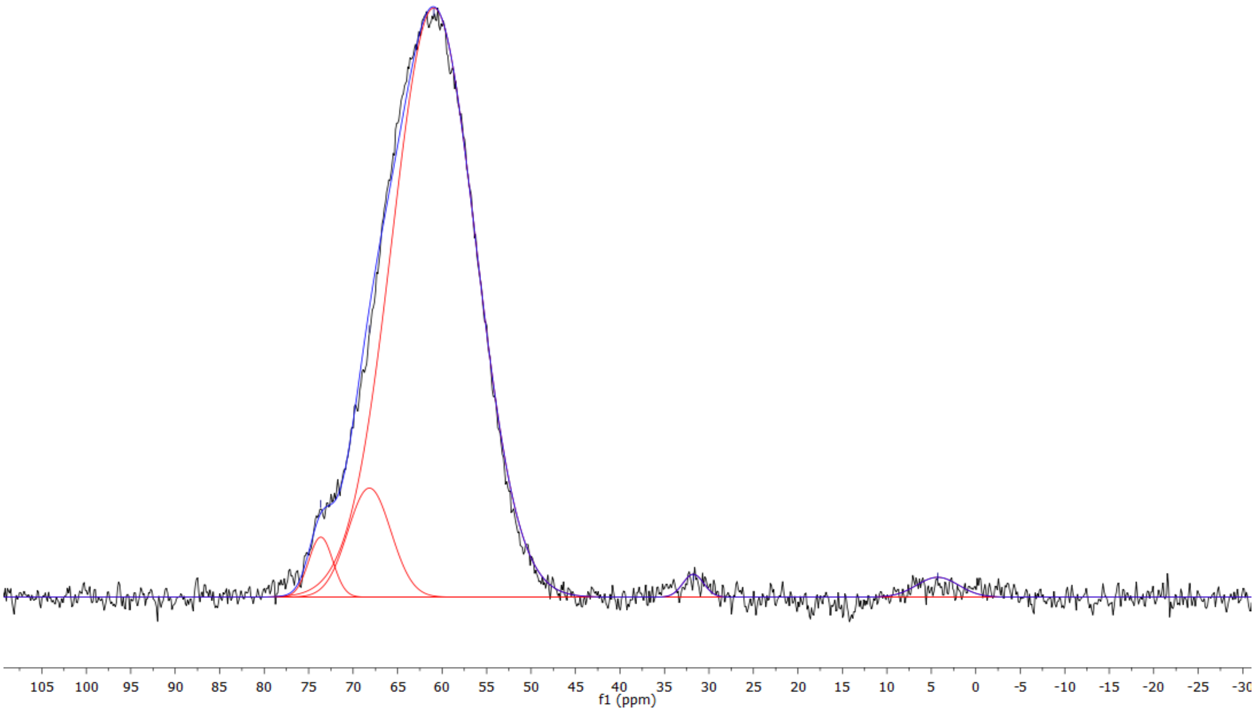

Figure 70: ^{27}Al NMR spectrum of CASH_DR_1.5H.

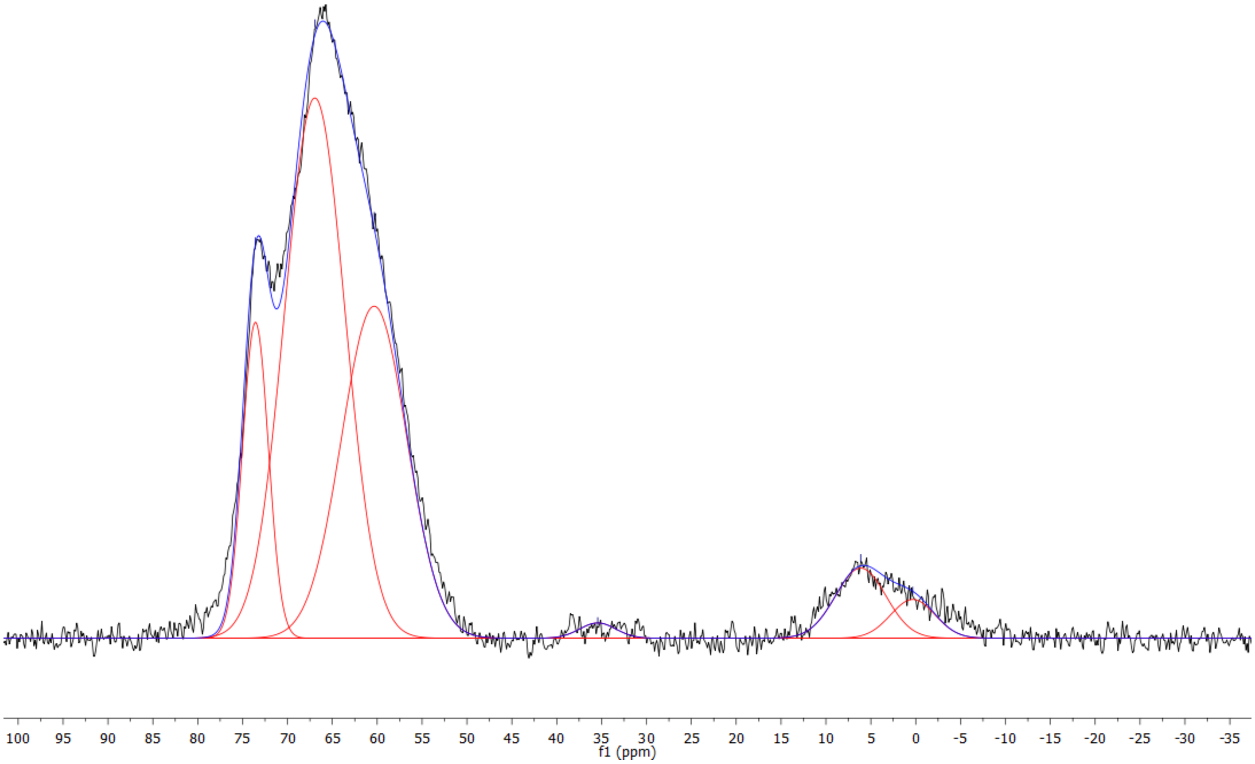

Figure 71: ^{27}Al NMR spectrum of CASH_DR_1.7H.

Table 19: Deconvolution peak properties for CASH_DR_0.9H, CASH_DR_1.1H, CASH_DR_1.3H, CASH_DR_1.5H, and CASH_DR_1.7H.

	Assignment	Chemical shift (ppm)	Width (ppm)	Proportion
CASH_DR_0.9H	Al[4]	65.03	3.61	3.6%
	Al[4]	57.39	8.82	96.4%
CASH_DR_1.1H	Al[4]	64.32	4.01	4.0%
	Al[4]	56.65	8.75	88.2%
	Al[6]	8.46	5.73	4.9%
	Al[6]	3.25	5.59	2.9%
CASH_DR_1.3H	Al[4]	65.07	4.66	5.8%
	Al[4]	57.08	9.46	93.3%
	Al[6]	5.19	4.62	1.0%
CASH_DR_1.5H	Al[4]	73.64	3.19	2.5%
	Al[4]	68.17	5.69	8.3%
	Al[4]	60.94	11.08	86.9%
	Al[5]	31.76	2.75	0.8%
	Al[6]	4.29	5.54	1.5%
CASH_DR_1.7H	Al[4]	73.57	3.40	12.0%
	Al[4]	66.95	7.93	47.8%
	Al[4]	60.34	8.55	31.7%
	Al[5]	35.43	4.73	0.8%
	Al[6]	6.13	6.61	5.2%
	Al[6]	0.32	5.80	2.5%

The ^{27}Al spectrum for CASH_DR_0.9H, Figure 67, contains only Al[4] while all others, Figures 68-71, also contain Al[6]. Deconvolution peak properties are presented in Table 19. CASH_DR_1.5H and CASH_DR_1.7H also contain Al[5]. The Al[4] in CASH_DR_0.9H occurs in the alumina/silica gel, which is the predominant phase indicated by ^{29}Si NMR. In CASH_DR_1.5H and CASH_DR_1.7H there are multiple, well-defined Al[4] peaks. The ^{29}Si spectrum of CASH_DR_1.7H indicates that Al[4] is present in both Q^2 and Q^3 sites, which may lead to multiple peaks in the ^{27}Al spectrum.

However, other ^{29}Si spectra with Q^2 and Q^3 Al[4] sites do not show the same ^{27}Al NMR behavior.

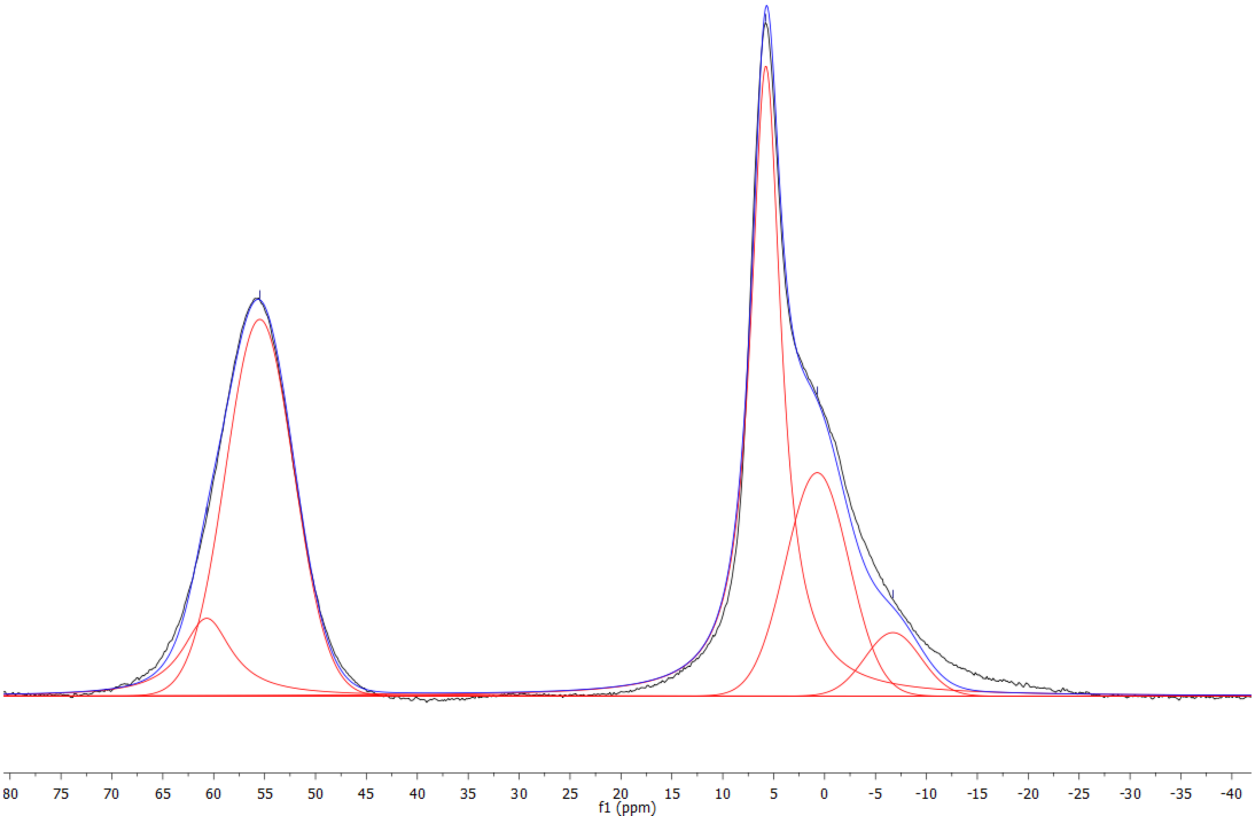

Figure 72: ^{27}Al NMR spectrum of CASH_DR_1.0C.

Table 20: Deconvolution peak properties.

	Assignment	Chemical shift (ppm)	Width (ppm)	Proportion
CASH_DR_1.0C	Al[4]	55.47	7.85	32.8%
	Al[4]	60.68	5.88	7.5%
	Al[6]	0.72	7.30	18.1%
	Al[6]	5.77	3.59	37.1%
	Al[6]	-6.71	6.47	4.6%

The ^{27}Al spectrum for CASH_DR_1.0C, presented in Figure 72 and peak properties in Table 20, consists of Al[4] and Al[6]. The Al[4] and Al[6] both occur in the alumina/silica gel that is detected from XRD and ^{29}Si NMR [ref 90]. No C-A-S-H is present. The Al[6] peak at 0.72 ppm comes from unreacted aluminum nitrate, which is expected to have a chemical shift of 0.00 ppm.

4.4 XRF

4.4.1 C-S-H SYNTHESIZED BY DOUBLE DECOMPOSITION

Table 21: XRF results in mass percent for CSH_DD_1.0A, CSH_DD_1.3A, and CSH_DD_1.5A.

	CSH_DD_1.0A	CSH_DD_1.3A	CSH_DD_1.5A
SiO_2	41.34	38.33	37.9
Al_2O_3	0.04	0.05	0.03
CaO	26.37	29.47	30.84
Fe_2O_3	0.03	0.03	0.03
MgO	0.04	0.04	0.04
SO_3	0.05	0.03	0.03
Na_2O	6.4	2.58	2.95
K_2O	0.01	0.01	0
TiO_2	0	0	0
P_2O_5	0	0	0

Table 22: Calculated molar percent from XRF results for CSH_DD_1.0A, CSH_DD_1.3A, and CSH_DD_1.5A.

	CSH_DD_1.0A	CSH_DD_1.3A	CSH_DD_1.5A
Si	50.30%	51.05%	49.35%
Al	0.06%	0.08%	0.05%
Ca	34.38%	42.05%	43.02%
Fe	0.03%	0.03%	0.03%
Mg	0.07%	0.08%	0.08%
S	0.05%	0.03%	0.03%
Na	15.10%	6.66%	7.45%
K	0.02%	0.02%	0.00%
Ti	0.00%	0.00%	0.00%
P	0.00%	0.00%	0.00%
Ca/Si	0.68	0.82	0.87
Al/Si	0.00	0.00	0.00
Ca/(Al+Si)	0.68	0.82	0.87

Table 21 presents the XRF data and Table 22 presents the calculated molar percentages for CSH_DD_1.0A, CSH_DD_1.3A, and CSH_DD_1.5A. All samples have Ca/Si ratios well below the starting Ca/Si ratios. Additionally, sodium is found in all three samples, likely as a charge balancing cation.

Table 23: XRF results in mass percent for CSH_DD_0.8B, CSH_DD_0.9B, CSH_DD_1.1B, CSH_DD_1.3B, and CSH_DD_1.5B.

	CSH_DD_ 0.8B	CSH_DD_ 0.9B	CSH_DD_ 1.1B	CSH_DD_ 1.3B	CSH_DD_ 1.5B
SiO_2	43.31%	42.58%	40.91%	41.22%	41.94%
Al_2O_3	0.40%	0.31%	0.17%	0.56%	0.4.0%
CaO	29.49%	31.1%	30.5%	31.35%	31.62%
Fe_2O_3	0.04%	0.02%	0.07%	0.06%	0.02%
MgO	0.06%	0.05%	0.07%	0.06%	0.06%
SO_3	0.03%	0.01%	0.06%	0.02%	0.01%
Na_2O	0.01%	0.00%	0.04%	0.00%	0.00%
K_2O	0.01%	0.00%	0.02%	0.00%	0.00%

Table 24: Calculated molar percent from XRF results for CSH_DD_0.8B, CSH_DD_0.9B, CSH_DD_1.1B, CSH_DD_1.3B, and CSH_DD_1.5B.

	CSH_DD_ 0.8B	CSH_DD_ 0.9B	CSH_DD_ 1.1B	CSH_DD_ 1.3B	CSH_DD_ 1.5B
Si	57.32%	55.76%	55.21%	54.51%	54.89%
Al	0.62%	0.48%	0.27%	0.87%	0.62%
Ca	41.82%	43.64%	44.11%	44.42%	44.34%
Fe	0.04%	0.02%	0.07%	0.06%	0.02%
Mg	0.12%	0.10%	0.14%	0.12%	0.12%
S	0.03%	0.01%	0.06%	0.02%	0.01%
Na	0.03%	0.00%	0.10%	0.00%	0.00%
K	0.02%	0.00%	0.03%	0.00%	0.00%
Ca/Si	0.73	0.78	0.80	0.81	0.81
Al/Si	0.01	0.01	0.00	0.02	0.01
Ca/(Al+Si)	0.72	0.78	0.79	0.80	0.80

Table 23 presents the XRF data and Table 24 presents the calculated molar percentages for CSH_DD_0.8B, CSH_DD_0.9B, CSH_DD_1.1B, CSH_DD_1.3B, and CSH_DD_1.5B. All samples have Ca/Si ratios well below the starting Ca/Si ratios. These Ca/Si ratios are almost equivalent across all samples.

4.4.2 C-S-H SYNTHESIZED BY DIRECT REACTION

Table 25: XRF results in mass percent for CSH_DR_1.0A, CSH_DR_1.3A, and CSH_DR_1.5A.

	CSH_DR_1.0A	CSH_DR_1.3A	CSH_DR_1.5A
SiO_2	43.85%	45.27%	37.84%
Al_2O3	0.08%	0.04%	0.03%
CaO	28.24%	25.02%	36.81%
Fe_2O_3	0.04%	0.02%	0.02%
MgO	0.03%	0.03%	0.03%
SO_3	0.05%	0.03%	0.02%
Na_2O	0.00%	0.05%	0.00%
K_2O	0.02%	0.00%	0.00%
TiO_2	0.00%	0.00%	0.00%
P_2O_5	0.00%	0.00%	0.00%

Table 26: Calculated molar percent from XRF results for CSH_DR_1.0A, CSH_DR_1.3A, and CSH_DR_1.5A.

	CSH_DR_1.0A	CSH_DR_1.3A	CSH_DR_1.5A
Si	58.98%	62.61%	48.89%
Al	0.13%	0.07%	0.05%
Ca	40.70%	37.08%	50.96%
Fe	0.04%	0.02%	0.02%
Mg	0.06%	0.06%	0.06%
S	0.05%	0.03%	0.02%
Na	0.00%	0.13%	0.00%
K	0.03%	0.00%	0.00%
Ti	0.00%	0.00%	0.00%
P	0.00%	0.00%	0.00%
Ca/Si	0.69	0.59	1.04
Al/Si	0.00	0.00	0.00
Ca/(Al+Si)	0.69	0.59	1.04

Table 25 presents the XRF data and Table 26 presents the calculated molar percentages for CSH_DR_1.0A, CSH_DR_1.3A, and CSH_DR_1.5A. The Ca/Si ratios for all samples are all significantly lower than the starting Ca/Si ratios. Additionally, they do not maintain the same relative order of Ca/Si ratio, with CSH_DR_1.3A having a lower Ca/Si than CSH_DR_1.0A.

4.4.3 C-A-S-H SYNTHESIZED BY DOUBLE DECOMPOSITION

Table 27: XRF results in mass percent for CASH_DD_0.8B, CASH_DD_0.9B, CASH_DD_1.1B, CASH_DD_1.3B, and CASH_DD_1.5B.

	CASH_DD_ 0.8B	CASH_DD_ 0.9B	CASH_DD_ 1.1B	CASH_DD_ 1.3B	CASH_DD_ 1.5B
SiO_2	35.54%	34.22%	32.97%	33.62%	33.27%
Al_2O3	11.92%	11.20%	11.03%	11.40%	10.60%
CaO	24.86%	25.54%	26.02%	26.03%	25.40%
Fe_2O_3	0.04%	0.03%	0.06%	0.04%	0.03%
MgO	0.03%	0.03%	0.04%	0.04%	0.05%
SO_3	0.01%	0.01%	0.02%	0.02%	0.01%
Na_2O	0.03%	0.03%	0.03%	0.00%	0.02%
K_2O	0.01%	0.01%	0.01%	0.00%	0.00%

Table 28: Calculated molar percent from XRF results for CASH_DD_0.8B, CASH_DD_0.9B, CASH_DD_1.1B, CASH_DD_1.3B, and CASH_DD_1.5B.

.

	CASH_DD	CASH_DD	CASH_DD_1.	CASH_DD_1.	CASH_DD
Si	46.53%	45.67%	44.53%	44.79%	45.50%
Al	18.39%	17.62%	17.56%	17.90%	17.09%
Ca	34.87%	36.52%	37.65%	37.16%	37.22%
Fe	0.04%	0.03%	0.06%	0.04%	0.03%
Mg	0.06%	0.06%	0.08%	0.08%	0.10%
S	0.01%	0.01%	0.02%	0.02%	0.01%
Na	0.08%	0.08%	0.08%	0.00%	0.05%
K	0.02%	0.02%	0.02%	0.00%	0.00%
Ca/Si	0.75	0.80	0.85	0.83	0.82
Al/Si	0.40	0.39	0.39	0.40	0.38
Ca/(Al+Si)	0.54	0.58	0.61	0.59	0.59

Table 27 presents the XRF data and Table 28 presents the calculated molar percentages for CASH_DD_0.8B, CASH_DD_0.9B, CASH_DD_1.1B, CASH_DD_1.3B, and CASH_DD_1.5B. The samples all have Ca/Si lower than the starting Ca/Si, and samples CASH_DD_1.1B, CASH_DD_1.3B, and CASH_DD_1.5B are approximately equal. The Al/Si ratios for all samples are approximately equal. The Al/Si ratios in these samples are close to maximum aluminum content in alumina/silica gel if Lowenstein's rule (no Al-O-Al bonds) of 38% [25]. This supports the ^{29}Si NMR spectra of these samples that indicate significant amounts of alumina/silica gel.

4.4.4 C-A-S-H SYNTHESIZED BY DIRECT REACTION

Table 29: XRF results in mass percent for CASH_DR_1.0A, CASH_DR_1.3A, and CASH_DR_1.5A.

	CASH_DR_1.0A	CASH_DR_1.3A	CASH_DR_1.5A
SiO_2	44.94%	37.14%	37.50%
Al_2O3	8.38%	7.33%	0.23%
CaO	18.75%	27.69%	30.56%
Fe_2O_3	0.04%	0.02%	0.02%
MgO	0.01%	0.02%	0.03%
SO_3	0.03%	0.03%	0.03%
Na_2O	0.01%	0.00%	0.00%
K_2O	0.00%	0.00%	0.00%
TiO_2	0.00%	0.00%	0.00%
P_2O_5	0.00%	0.00%	0.00%

Table 30: Calculated molar percent from XRF results for CASH_DR_1.0A, CASH_DR_1.3A, and CASH_DR_1.5A.

	CASH_DR_1.0A	CASH_DR_1.3A	CASH_DR_1.5A
Si	59.92%	49.18%	53.12%
Al	13.17%	11.44%	0.38%
Ca	26.79%	39.29%	46.38%
Fe	0.04%	0.02%	0.02%
Mg	0.02%	0.04%	0.06%
S	0.03%	0.03%	0.03%
Na	0.03%	0.00%	0.00%
K	0.00%	0.00%	0.00%
Ti	0.00%	0.00%	0.00%
P	0.00%	0.00%	0.00%
Ca/Si	0.45	0.80	0.87
Al/Si	0.22	0.23	0.01
Ca/(Al+Si)	0.37	0.65	0.87

Table 29 presents the XRF data and Table 30 presents the calculated molar percentages for CASH_DR_1.0A, CASH_DR_1.3A, and CASH_DR_1.5A. The Ca/Si ratios for the samples are all well below the starting Ca/Si ratios. The Al/Si ratios of CASH_DR_1.0A and CASH_DR_1.3A are approximately equal while CASH_DR_1.5A did not take up any aluminum.

Table 31: XRF results in mass percent for CASH_DR_1.0B, CASH_DR_1.3B, and CASH_DR_1.5B.

	CASH_DR_1.0B	CASH_DR_1.3B	CASH_DR_1.5B
SiO_2	42.72%	36.61%	34.40%
Al_2O3	8.60%	7.60%	6.76%
CaO	18.97%	26.26%	25.08%
Fe_2O_3	0.04%	0.04%	0.02%
MgO	0.02%	0.02%	0.02%
SO_3	0.06%	0.03%	0.03%
Na_2O	0.04%	0.00%	0.00%
K_2O	0.01%	0.00%	0.00%
TiO_2	0.00%	0.00%	0.00%
P_2O_5	0.00%	0.00%	0.00%

Table 32: Calculated molar percent from XRF results for CASH_DR_1.0B, CASH_DR_1.3B, and CASH_DR_1.5B.

	CASH_DR_1.0B	CASH_DR_1.3B	CASH_DR_1.5B
Si	58.22%	49.61%	49.63%
Al	13.81%	12.14%	11.50%
Ca	27.70%	38.13%	38.77%
Fe	0.04%	0.04%	0.02%
Mg	0.04%	0.04%	0.04%
S	0.06%	0.03%	0.03%
Na	0.11%	0.00%	0.00%
K	0.02%	0.00%	0.00%
Ti	0.00%	0.00%	0.00%
P	0.00%	0.00%	0.00%
Ca/Si	0.48	0.77	0.78
Al/Si	0.24	0.24	0.23
Ca/(Al+Si)	0.38	0.62	0.63

Table 31 presents the XRF data and Table 32 presents the calculated molar percentages for CASH_DR_1.0B, CASH_DR_1.3B, and CASH_DR_1.5B. The Ca/Si ratios of all the samples are significantly lower than the starting Ca/Si, and CASH_DR_1.3B and CASH_DR_1.5B are almost equivalent. The Al/Si ratios remains approximately constant across all samples.

Table 33: XRF results in mass percent for CASH_DR0.9H, CASH_DR_1.1H, CASH_DR_1.3H, CASH_DR_1.5H, and CASH_D_1.7H.

	CASH_DR_0.9H	CASH_DR_1.1H	CASH_DR_1.3H	CASH_DR_1.5H	CASH_DR_1.7H
SiO_2	43.83%	41.05%	27.15%	36.98%	29.19%
Al_2O3	9.46%	9.58%	5.45%	8.08%	6.74%
CaO	16.69%	18.28%	14.13%	24.53%	22.42%
Fe_2O_3	0.17%	0.07%	0.03%	0.05%	0.03%
MgO	0.11%	0.04%	0.04%	0.04%	0.03%
SO_3	0.03%	0.02%	0.01%	0.01%	0.01%
Na_2O	0.04%	0.00%	0.00%	0.00%	0.00%
K_2O	0.05%	0.01%	0.01%	0.01%	0.01%
TiO_2	0.01%	0.00%	0.00%	0.00%	0.00%
P_2O_5	0.00%	0.00%	0.00%	0.00%	0.00%

Table 34: Calculated molar percent from XRF results for CASH_DR0.9H, CASH_DR_1.1H, CASH_DR_1.3H, CASH_DR_1.5H, and CASH_D_1.7H.

	CASH_DR_0.9H	CASH_DR_ 1.1H	CASH_DR_ 1.3H	CASH_DR_ 1.5H	CASH_DR_ 1.7H
Si	59.77%	56.96%	55.62%	50.72%	47.66%
Al	15.21%	15.67%	13.16%	13.06%	12.97%
Ca	24.39%	27.18%	31.01%	36.05%	39.22%
Fe	0.17%	0.07%	0.05%	0.05%	0.04%
Mg	0.22%	0.08%	0.12%	0.08%	0.07%
S	0.03%	0.02%	0.02%	0.01%	0.01%
Na	0.11%	0.00%	0.00%	0.00%	0.00%
K	0.09%	0.02%	0.03%	0.02%	0.02%
Ti	0.01%	0.00%	0.00%	0.00%	0.00%
P	0.00%	0.00%	0.00%	0.00%	0.00%
Ca/Si	0.41	0.48	0.56	0.71	0.82
Al/Si	0.25	0.28	0.24	0.26	0.27
Ca/(Al+Si)	0.33	0.37	0.45	0.57	0.65

Table 33 presents the XRF data and Table 34 presents the calculated molar percentages for CASH_DR_0.9H, CASH_DR_1.1H, CASH_DR_1.3H, CASH_DR_1.5H, and CASH_DR_1.7H. The Ca/Si ratios for all of the samples are less than the starting Ca/Si ratios. The Al/Si ratio is approximately equivalent across all samples.

Table 35: XRF results in mass percent for CASH_DR0.9L, CASH_DR_1.1L, CASH_DR_1.3L, CASH_DR_1.5L, and CASH_D_1.7L

	CASH_DR_0.9L	CASH_DR_1.1L	CASH_DR_1.3L	CASH_DR_1.5L	CASH_DR_1.7L
SiO_2	43.37	-	30.31	31.14	28.33
Al_2O_3	5.11	-	3.11	3.06	3.11
CaO	21.99	-	19.03	23.66	25.46
Fe_2O_3	0.03	-	0.02	0.02	0.02
MgO	0.02	-	0.02	0.02	0.03
SO_3	0.01	-	0.01	0.01	0.01
Na_2O	0	-	0	0	0
K_2O	0	-	0	0	0
TiO_2	0	-	0	0	0
P_2O_5	0	-	0	0	0

Table 36: Calculated molar percent from XRF results for CASH_DR0.9L, CASH_DR_1.1L, CASH_DR_1.3L, CASH_DR_1.5L, and CASH_D_1.7L.

	CASH_DR_0.9L	CASH_DR_1.1L	CASH_DR_1.3L	CASH_DR_1.5L	CASH_DR_1.7L
Si	59.40%	-	55.70%	51.77%	47.74%
Al	8.25%	-	6.74%	6.00%	6.18%
Ca	32.27%	-	37.47%	42.15%	45.97%
Fe	0.03%	-	0.03%	0.03%	0.03%
Mg	0.04%	-	0.05%	0.05%	0.08%
S	0.01%	-	0.01%	0.01%	0.01%
Na	0.00%	-	0.00%	0.00%	0.00%
K	0.00%	-	0.00%	0.00%	0.00%
Ti	0.00%	-	0.00%	0.00%	0.00%
P	0.00%	-	0.00%	0.00%	0.00%
Ca/Si	0.54	-	0.67	0.81	0.96
Al/Si	0.14	-	0.12	0.12	0.13
Ca/(Al+Si)	0.48	-	0.60	0.73	0.85

Table 35 presents the XRF data and Table 36 presents the calculated molar percentages for CASH_DR0.9L, CASH_DR_1.1L, CASH_DR_1.3L, CASH_DR_1.5L, and CASH_D_1.7L. XRF results for sample CASH_DR_1.1L could not be obtained due to a loss of vacuum during the experiment. All samples have lower Ca/Si ratios than the starting Ca/Si ratios. The Al/Si ratio is approximately equal across all samples. These samples had an Al/Si of approximately half that of the CASH_DR_#H samples.

4.5 TGA

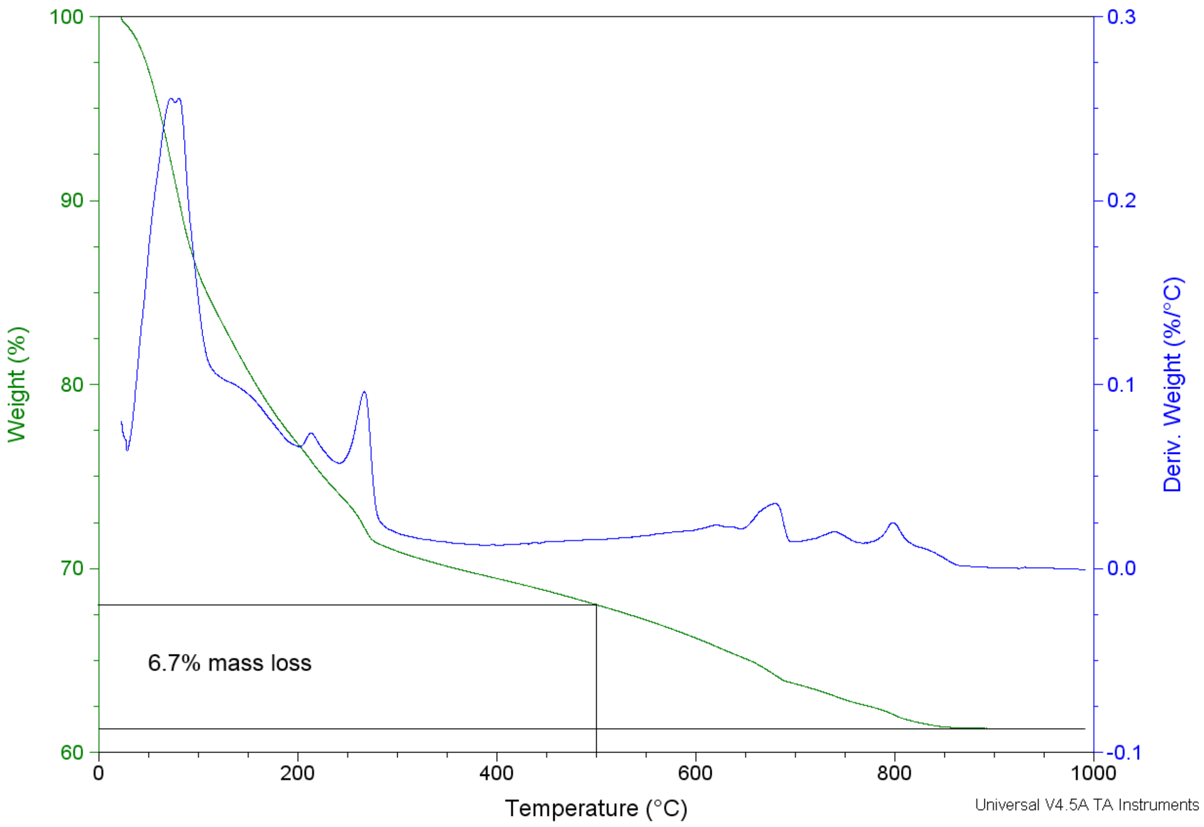

Figure 73: TGA results of CSH_DR_1.3A_NaNO3.

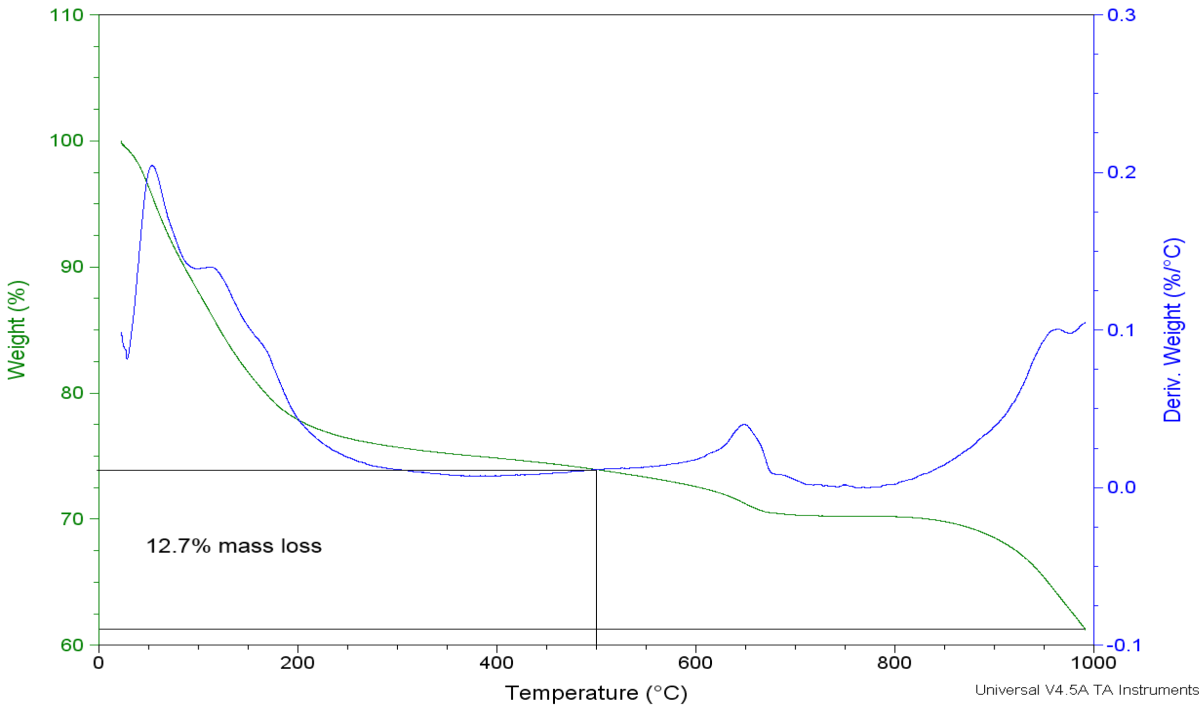

Figure 74: TGA results for CSH_DR_1.3A_NaOH.

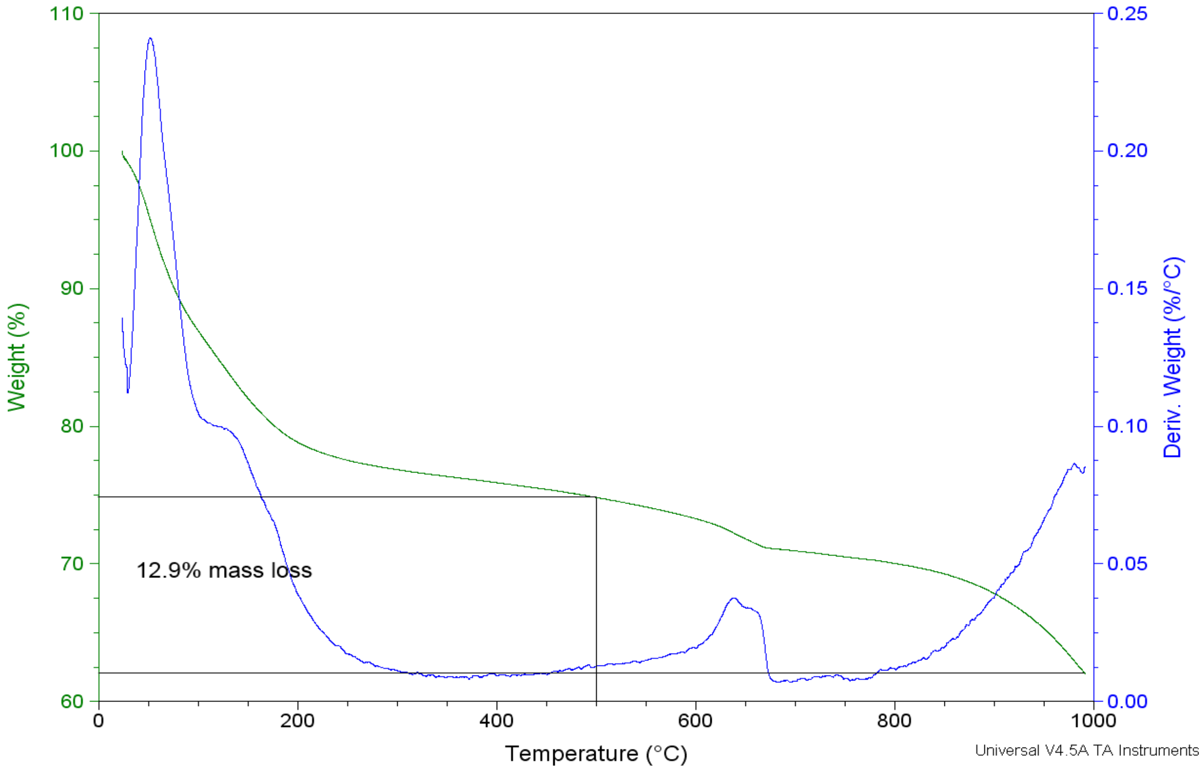

Figure 75: TGA results for CSH_DR_1.3E_KOH.

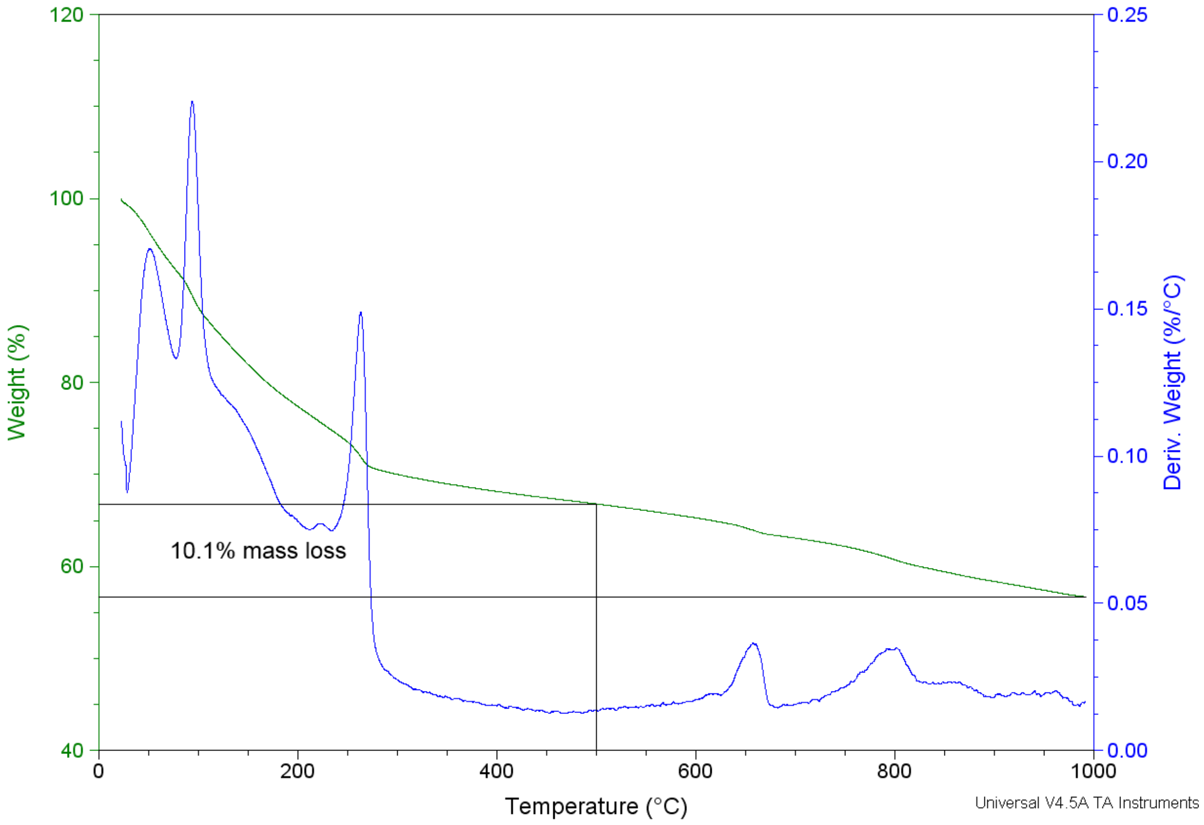

Figure 76: TGA results for CSH_DR_1.3A_H2O.

The TGA results for the carbonation treatment reveal mass loss associated with CO_2 release (550-1000°C) in Figures 73-76. The sample treated with KOH had the largest mass loss (12.9%) followed by NaOH (12.7%), H_2O (10.1%), and $NaNO_3$ (6.7%).

5. DISCUSSION

The results presented in Chapter 4 use advanced characterization techniques to probe the molecular structure of C-S-H and C-A-S-H with varying Ca/Si ratios and aluminum content. Additionally, the carbonation behavior of C-S-H under different alkali and pH conditions was observed. These results were analyzed in order to understand the effect of these factors on the composition and molecular structure of these phases.

5.1 EFFECT OF CA/SI RATIO

5.1.1 CRYSTAL STRUCTURE

The XRD analysis shows that C-S-H was formed in all syntheses of C-S-H. Many of the patterns contained basal peaks, but there is no relation to the Ca/Si ratio of the C-S-H. The samples in series CSH_DD_#A have more intense C-S-H peaks as the Ca/Si ratio decreases. However, this trend does not hold with the samples synthesized by direct reaction in which there is no apparent trend. There is no shift in peak position with changing Ca/Si ratio.

5.1.2 MOLECULAR STRUCTURE

The effect of the Ca/Si ratio is most readily observed from ^{29}Si NMR. The calculation of MCL of the silicate chain in C-S-H can be calculated under the assumption of a dreierkettern structure by:

$$\mathrm{MCL} = \frac{2}{\frac{Q^1(0Al)}{Q^1(0Al) + Q_P{}^2(0\mathrm{Al}) + Q_B{}^2(0\mathrm{Al}) + \frac{3}{2}Q^2(1\mathrm{Al}) + Q^3(0Al) + Q^3(1Al)}} \tag{4}$$

which is a modified version of Equation 1 to include Q^3. The presence of Q^3 is incorporated into this equation by simply adding Q^3(0Al) and Q^3(1Al) to the sum all tetrahedra in the denominator. The original equation did only considered linear chain structures. Figure 77 and Table 37 show the MCL data in relation to the Ca/Si ratio from XRF.

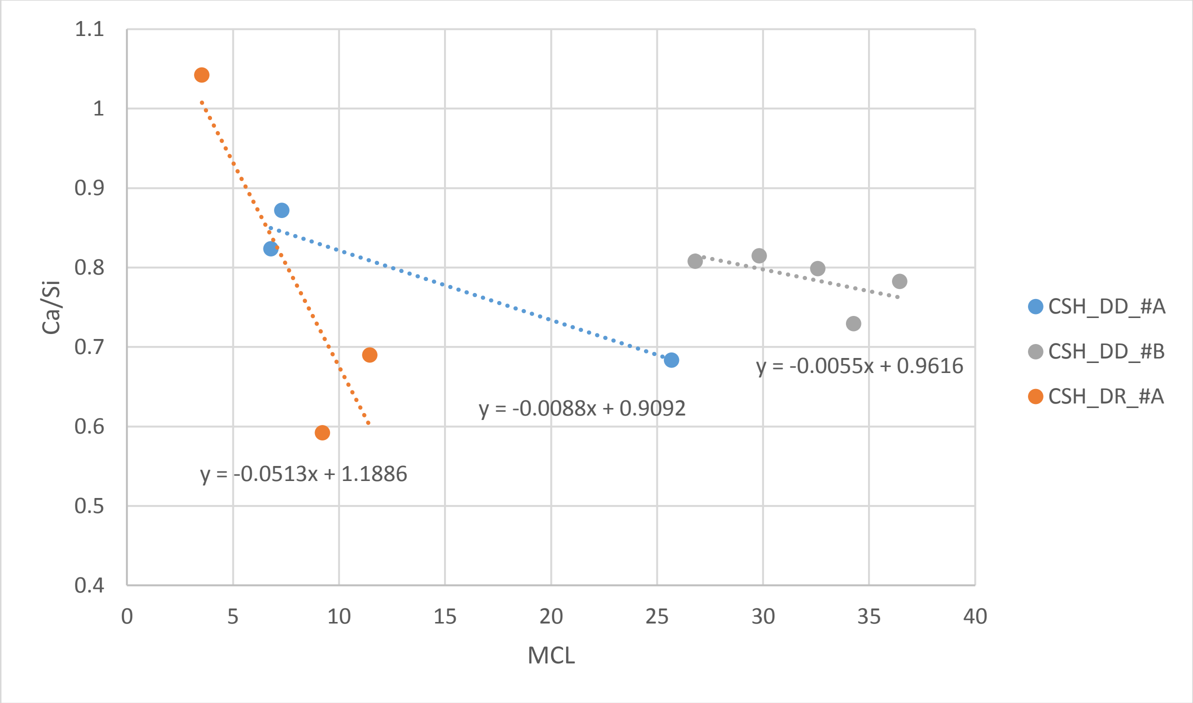

Figure 77: Plot of Ca/Si ratio from XRF versust MCL from ^{29}Si NMR for C-S-H.

Table 37: MCL from ^{29}Si NMR and Ca/Si ratio from XRF for C-S-H.

	MCL	Ca/Si
CSH_DD_1.0A	25.7	0.68
CSH_DD_1.3A	6.8	0.82
CSH_DD_1.5A	7.3	0.87
CSH_DD_0.8B	34.3	0.73
CSH_DD_0.9B	36.4	0.78
CSH_DD_1.1B	32.6	0.80
CSH_DD_1.3B	29.8	0.81
CSH_DD_1.5B	26.8	0.81
CSH_DR_1.0A	11.4	0.69
CSH_DR_1.3A	9.2	0.59
CSH_DR_1.5A	3.5	1.04

From Figure 77 it is apparent that there is a general trend of increase in MCL with a decrease in Ca/Si ratio, this agrees with the literature [11, 30]. However, the relationship is not strong. The narrow spread of Ca/Si ratios limits broad interpretation of the samples. The slopes of the linear regressions for the C-S-H synthesized by double decomposition are similar and the slope of the linear regression line of the C-S-H synthesized by direct reaction is greater. The CSH_DD_#B samples have a higher MCL than CSH_DD_#A for a given Ca/Si ratio due to the effect of carbonation increasing the MCL. Carbonation was more significant for the CSH_DD_#B samples, as indicated by XRD. The influence of Ca/Si ratio on MCL is dependent on the synthesis method.

5.2 EFFECT OF AL INCORPORATION

5.2.1 CRYSTAL STRUCTURE

The XRD analysis shows that, in most cases, C-A-S-H was formed. The position of the diffraction peaks for C-A-S-H is indistinguishable from the position of the diffraction peaks in C-S-H. Samples CASH_DR_1.0A and CASH_DR_1.0B, presented in Figure 10 and Figure 11, do not indicate C-A-S-H. These plots show only one peak at about 29.2° that has been previously reported for C-S-H, but this peak can also be attributed to calcite. Additionally, a large amorphous hump is present between about 20° and 30°. This hump indicates alumina/silica gel with low structural order. Neither of these samples showed substantial $CaCO_3$ peaks. The lack of $CaCO_3$ peaks suggests that the silica gel and very poorly ordered C-S-H were formed during synthesis and that these phases are not the results of carbonation.

When Al is incorporated into the C-S-H structure there is no change in diffraction peak positions. Specifically, the peaks corresponding to the (200) at 32.0° and (020) at 49.8° dimensions of C-S-H did not change position. These dimensions are of the octahedral CaO layer. The lack of change in these dimensions indicates that octahedral aluminum is not being incorporated into the CaO layer of the C-S-H. The dimensions of the octahedral CaO layer were not observed to change in Sun's work either [2]. The Al[6] and Al[5] that were observed by ^{27}Al NMR is presumed to be located in the interlayer where there is little long range order as proposed by Sun et al. [2]. The lack of change in the XRD patterns with aluminum addition reflects this lack of long range order.

5.2.2 MOLECULAR STRUCTURE

The effect of aluminum incorporation on the molecular structure is most easily observed from ^{29}Si NMR. Samples CASH_DR_1.3A and CASH_DR_1.5B have Al[4] in the pairing tetrahedron position. The MCL was calculated for C-A-S-H samples by a modification of Equation 4 to include the presence of Al[4] in the pairing position of the alumino-silicate chain:

$$\mathrm{MCL} = \frac{2}{\dfrac{Q^1 + Q^1(1Al)}{Q^1 + Q^1(1Al) + {Q_P}^2 + {Q_B}^2 + \frac{3}{2}{Q_P}^2(1Al) + 2{Q_B}^2(1Al) + Q^3 + Q^3(1Al) - \frac{1}{2}\left({Q_B}^2(1Al) - Q^1(1Al)\right)}}. \quad (5)$$

The aluminum in the pairing tetrahedron position was considered by adding $Q^1(1Al)$ to the numerator and denominator and $Q^2_B(1Al)$ times a factor of two to the denominator in order to count both the detected silicon tetrahedron in the bridging position and the bonded aluminum in the pairing position. The term $-\frac{1}{2}({Q_B}^2(1Al) - Q^1(1Al)$ is in the denominator to ensure that the aluminum in pairing positions in the middle of the chain are not counted multiple times since aluminum in the pairing position is bonded to silicon in the bridging position and silicon in the pairing position.

In the C-A-S-H samples which contained C-A-S-H and alumina/silica gel two MCL values were calculated, with and without Q^3, to find lower and upper bounds of the MCL since it is difficult to differentiate between Q^3 in the C-S-H and Q^3 in the alumina/silica gel. Figure 78 and Table 38 show the MCL data in relation to the Ca/(Si+Al) ratio from XRF. The MCL in Figure 78 is the lower bound MCL.

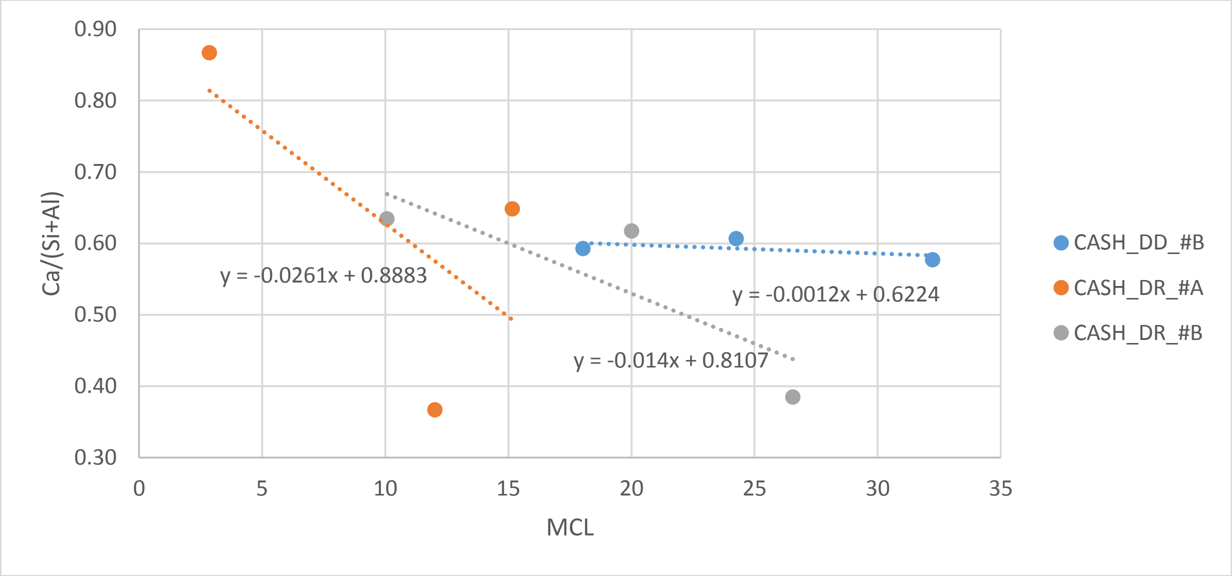

Figure 78: Plot of Ca/(Si+Al) from XRF against MCL from ^{29}Si NMR for C-A-S-H.

Table 38: MCL from ^{29}Si NMR and Ca/Si ratio from XRF for C-A-S-H.

	MCL lower bound	MCL upper bound	Ca/Si	Ca/(Si+Al)
CASH_DD_0.9B	32.2	44.3	0.80	0.58
CASH_DD_1.1B	24.3	37.5	0.85	0.61
CASH_DD_1.3B	18.0	23.6	0.83	0.59
CASH_DR_1.0A	12.0	18.3	0.45	0.37
CASH_DR_1.3A	15.2	-	0.80	0.65
CASH_DR_1.5A	2.9	-	0.87	0.87
CASH_DR_1.0B	26.6	33.0	0.48	0.38
CASH_DR_1.3B	20.0	-	0.77	0.62
CASH_DR_1.5B	10.1	-	0.78	0.63

Generally, the MCL increases as the Ca/(Si+Al) ratio decreases but the relationship is not strong. Sun et al also observed a similar relationship between MCL and Ca/(Si+Al) ratio [2].

When the Ca/Si ratios from XRF for C-A-S-H are compared to the Ca/Si ratios from XRF for C-S-H it is apparent that there is a large discrepancy. Table 39 shows the MCL and Ca/Si for the direct reaction samples, sorted by Ca/Si.

Table 39: Comparison of C-S-H and C-A-S-H MCL and Ca/Si ratios.

	MCL	Ca/Si		MCL lower bound	MCL upper bound	Ca/Si	Ca/(Si+ Al)
CSH_DR_1.3A	9.2	0.59	CASH_DR_1.0A	12.0	18.3	0.45	0.37
CSH_DR_1.0A	11.4	0.69	CASH_DR_1.0B	26.6	33.0	0.48	0.38
CSH_DR_1.5A	3.5	1.04	CASH_DR_1.3B	20.0	-	0.77	0.62
			CASH_DR_1.5B	10.1	-	0.78	0.63
			CASH_DR_1.3A	15.2	-	0.80	0.65
			CASH_DR_1.5A	2.9	-	0.87	0.87

The direct reaction syntheses for the C-S-H and the C-A-S-H "A" series had the same initial Ca/Si ratios, but the XRF data indicate that the final Ca/Si ratios were lower for the C-A-S-H than the C-S-H. The analysis is complicated further by the fact that sample CSH_DR_1.0A had a higher Ca/Si ratio than CASH_DR_1.3A from XRF. The C-A-S-H "B" series had starting Ca/(Si+Al) values equal to the Ca/Si of the C-S-H. From the XRF data the C-A-S-H "B" series had lower Ca/(Si+Al) values than the C-S-H. The inconsistency in Ca/Si ratios makes it difficult to determine if aluminum is having an effect on the MCL. Certainly the MCL is generally longer for C-A-S-H samples, but the Ca/Si ratio is generally lower as well, which has been seen to increase the MCL here and in the literature [11, 30].

The discrepancy in Ca/Si ratios of the C-S-H and the C-A-S-H even when the starting Ca/Si ratios were the same appears to be due to the addition of aluminum. To further explore this, CASH_DR_1.0C was synthesized by placing CSH_DR_1.0A in a solution of aluminum nitrate backfilled with nitrogen and stirring for 24 hours. The XRD pattern in Figure 16 of this sample shows only alumina/silica gel in the form of an amorphous hump from 20° to 30° with no $CaCO_3$ or C-S-H peaks. The ^{29}Si spectrum in Figure 45 also shows only alumina/silica gel in this sample. From these experiments, it appears that the addition of aluminum to C-S-H is a dissolution/precipitation phenomenon. If dissolution/precipitation does not occur, it is expected that the general structure of C-S-H would be preserved with the addition of aluminum. The dissolution/precipitation process may explain the discrepancy in the C-S-H and C-A-S-H Ca/Si ratios from XRF in which the precipitate is tending towards alumina/silica gel.

5.3 DEPENDENCE OF AL UPTAKE ON CA/SI RATIO

5.3.1 QUANTITY OF AL UPTAKE

The quantity of aluminum taken into the C-S-H structure was determined using three different methods. The area of the Al[4] peaks from ^{27}Al NMR was normalized to the mass of the sample and compared. An area function was developed to correlate data taken using the 750NB and 750WB magnets by running a sample of reagent grade $NaAlO_2$ on each spectrometer and comparing the integrated areas, shown in Table 40. The samples run on the 300UI spectrometer are compared to each other, but not to other samples, shown in Table 41. The Al/Si ratio was calculated from XRF in molar percent. The Al/Si ratio was also calculated from the ^{29}Si spectra according to:

$$\mathrm{Al/Si} = \frac{\frac{1}{2}Q_P{}^2(1Al) + Q_B{}^2(1Al) - \frac{1}{2}(Q_B{}^2(1Al) - Q^1(1Al))}{Q^1(0Al) + Q^1(1Al) + Q_P{}^2(0Al) + Q_B{}^2(0Al) + Q_P{}^2(1Al) + Q_B{}^2(1Al) + Q^3(0Al) + Q^3(1Al)} \qquad (6)$$

which is a modification of an equation proposed by Richardson [14] to include aluminum in the pairing tetrahedron position and Q^3 positions. The aluminum in the pairing tetrahedron position was considered by adding Q^1(1Al) and $Q^2{}_B$(1Al) in the denominator and adding $Q^2{}_B$(1Al) in the numerator. The term $-\frac{1}{2}(Q_B{}^2(1Al) - Q^1(1Al)$ is in the numerator to ensure that the aluminum in pairing positions in the middle of the chain are not counted multiple times since aluminum in the pairing position is bonded to silicon in the bridging position and silicon in the pairing position. The Q^3 position is considered by adding Q^3(0Al) and Q^3(1Al) to the denominator. Not all samples have ^{29}Si NMR data and therefore Al/Si ratios from ^{29}Si NMR are not available for these samples.

Table 40: Quantity of aluminum uptake into C-A-S-H.

	Normalized Al[4] -	Al/Si -	Al/Si -
CASH_DR_1.0A	130.8	0.22	0.02
CASH_DR_1.3A	61.0	0.23	0.18
CASH_DR_1.5A	0.0	0.01	0.00
CASH_DR_1.0B	142.4	0.24	0.05
CASH_DR_1.3B	121.3	0.24	0.05
CASH_DR_1.5B	155.5	0.23	0.09
CASH_DR_0.9H	113.8	0.25	-
CASH_DR_1.1H	232.2	0.28	-
CASH_DR_1.3H	173.9	0.24	-
CASH_DR_1.5H	37.0	0.26	-
CASH_DR_1.7H	50.7	0.27	0.05
CASH_DR_0.9L	45.4	0.14	-
CASH_DR_1.1L	15.1	-	-
CASH_DR_1.3L	17.9	0.12	-
CASH_DR_1.5L	15.9	0.12	-
CASH_DR_1.7L	15.0	0.13	0.02

Table 41: Quantity of aluminum uptake in C-A-S-H.

	Normalized Al[4] - ^{27}Al	Al/Si - XRF	Al/Si - ^{29}Si
CASH_DD_0.8B	147.1	0.40	-
CASH_DD_0.9B	119.7	0.39	0.04
CASH_DD_1.1B	150.0	0.39	0.03
CASH_DD_1.3B	141.1	0.40	0.03
CASH_DD_1.5B	123.9	0.38	-

The normalized Al[4] content is not constant across samples and is discussed in more detail below. The Al/Si ratios from XRF for the CASH_DR_#A and CASH_DR_#B series are all similar (≈0.23) and close to the maximum observed by others [2, 5, 22, 23], with the exception of CASH_DR_1.5A which contained no aluminum. Similarly, the CASH_DR_#H series also had Al/Si ratios that were consistent and ≈0.26. The CASH_DR_#L series had consistent Al/Si ratios of approximately half that of the CASH_DR_#H series. The concentration of the aluminum nitrate solution used to add aluminum to the C-S-H in the CASH_DR_#L series was half that of the CASH_DR_#H series. The Al/Si ratio is dependent on the concentration of aluminum in the solution when adding aluminum to already formed C-S-H.

The CASH_DD_#B series also have similar Al/Si ratio from XRF. However, they are ≈0.39 which is well above the maximum Al/Si ratios observed in the literature. The ^{29}Si spectra for CASH_DD_0.9B, CASH_DD_1.1B, and CASH_DD_1.3B all have Q^3 and Q^4 peaks associated with alumina/silica gel. Since aluminum appears to be occurring in the alumina/silica gel, then the Al/Si ratio given by XRF is not the Al/Si ratio of the C-

A-S-H, which aids in the explanation of the discrepancy in Al/Si ratios from the XRF and ^{29}Si data.

The Al/Si ratios from ^{29}Si are not consistent with the Al/Si ratios from XRF. One reason for this is that the ^{29}Si spectra only detect aluminum which is bonded to silicon which, in C-A-S-H, is tetrahedral. The ^{27}Al spectra for these samples also include Al[5] and Al[6] which are not detected by ^{29}Si NMR, and are not included in the assumptions for the equations for calculating Al/Si from the ^{29}Si NMR spectra. Due to these factors, it is reasonable that the Al/Si ratios from the ^{29}Si calculation are lower than the Al/Si ratios from the XRF data. However, this large of a discrepancy is still surprisingly large.

The quantities of Al[4] from ^{27}Al NMR of the samples synthesized by direct reaction have a weak positive correlation to the MCL and a weak negative correlation to the Ca/Si ratio, as seen in Figure 79 and Figure 80.

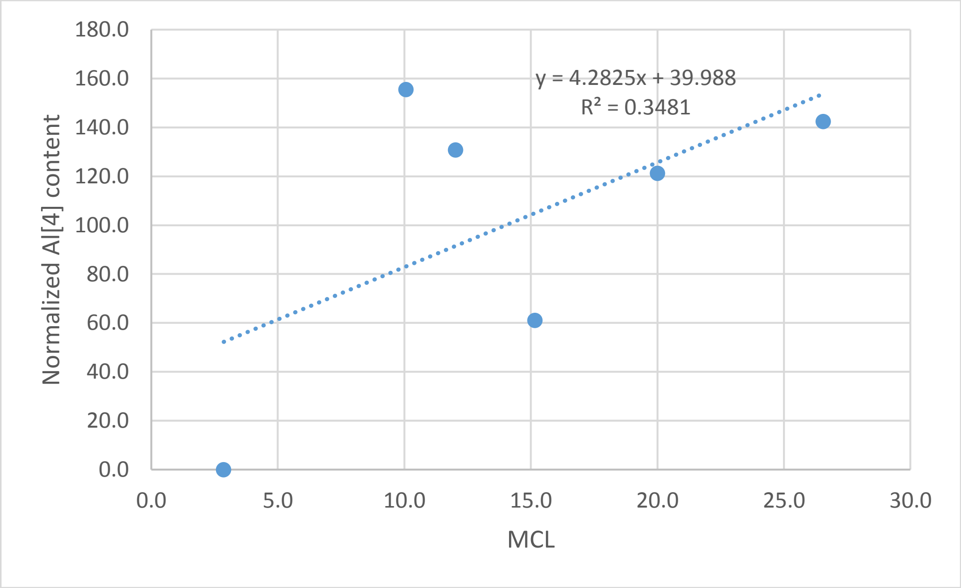

Figure 79: Plot of CASH_DR_#A and CASH_DR_#B Al[4] content against MCL.

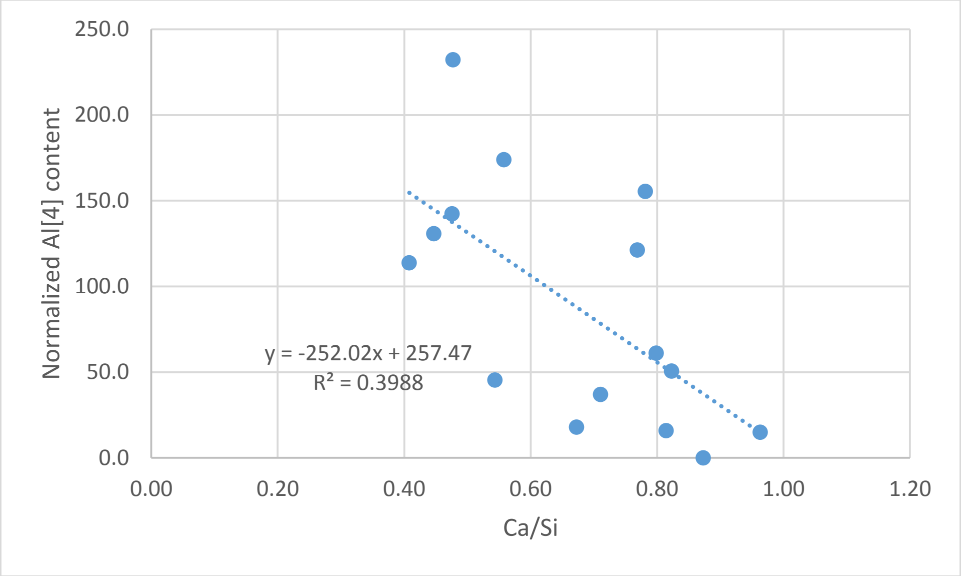

Figure 80: Plot of CASH_DR series Al[4] content against Ca/Si ratio.

These weak correlations suggest that the Ca/Si ratio or MCL impact the quantity of Al[4] incorporated. Since the Ca/Si ratio is correlated to the MCL, it is expected that the Al[4] content would correlate with both. However, the causation of the increase in Al[4] content is not apparent. The samples synthesized by double decomposition all have similar Ca/Si ratios from XRF and similar normalized Al[4] contents. The limited range of Ca/Si ratios in these samples makes it difficult to draw conclusions from these correlations. Faucon et al showed a similar lack of dependence of Al/Si ratio on Ca/(Si+Al) ratio to this work when the Ca/(Si+Al) ratio was less than 1.00, as is the case in our samples. At Ca/(Si+Al) greater than 1.00, the Al/Si ratio decreased with Ca/(Si+Al) ratio [22].

5.3.2 CHEMICAL SHIFT IN THE ^{27}AL SPECTRA

The chemical shift of the dominant Al[4] peak in the ^{27}Al spectra were observed to change with respect to the Ca/(Si+Al) ratio from XRF, as presented in Figure 81.

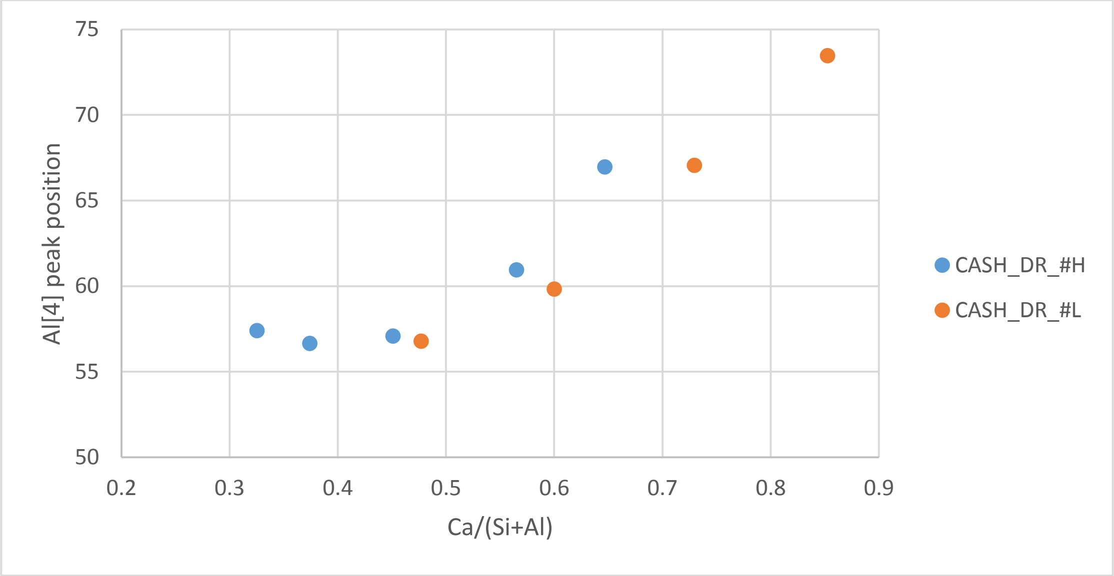

Figure 81: Dependence of Al[4] peak position on Ca/(Si+Al) ratio in C-A-S-H synthesized by direct reaction.

The Al[4] peak position increases with Ca/(Si+Al) ratio once the Ca/(Si+Al) ratio is greater than 0.5. A more positive chemical shift indicates less magnetic shielding of the aluminum nuclei. As seen previously, as the Ca/(Si+Al) ratio increases the MCL becomes shorter. A shorter MCL means that there is less magnetic shielding since there are fewer atoms in the vicinity of aluminum nuclei. At sufficiently high magnetic fields, such as those encountered here, the chemical shift of the ^{27}Al spectrum is sensitive to the MCL of the C-A-S-H. A similar trend in ^{27}Al chemical shift with change in Ca/Si ratio was observed by Faucon et al [25].

5.4 CARBONATION

The XRD patterns show that peaks associated with $CaCO_3$ were more prevalent in the C-S-H samples synthesized by double decomposition. None of the direct reaction syntheses indicated $CaCO_3$ polymorphs, while all but one, CSH_DD_1.3A, of the double decomposition syntheses had peaks associated with $CaCO_3$. Additionally, an amorphous hump associated with silica gel is seen in three of the double decomposition syntheses (CSH_DD_1.0A, CSH_DD_1.3B, and CSH_DD_1.1B) indicating a substantial change to the C-S-H structure caused by carbonation.

From Figure 77 it is apparent that the trend for double decomposition and direct reaction syntheses are different. The slopes of the linear regressions for the samples synthesized by double decomposition are similar, while the slope of the linear regression for the samples synthesized by direct reaction is much steeper. Additionally, the MCL is generally higher for a given Ca/Si when synthesized by double decomposition. This is thought to be due to the modification of the C-S-H structure from carbonation, as observed from XRD.

Similarly, in Figure 78 the slopes of the linear regressions are different for double decomposition and direct reaction synthesis methods in C-A-S-H. The slope of the double decomposition linear regression is significantly less than that of the direct reaction linear regressions, indicating a change in behavior with synthesis method. All three of the double decomposition samples were carbonated, as observed by XRD. Of the direct reaction samples, only CASH_DR_1.0A, CASH_DR_1.0B, and

CASH_DR_1.5B contained any $CaCO_3$ peaks and they were less well defined. Again, the MCL is generally higher for a given Ca/(Si+Al) when synthesized by double decomposition. The change in MCL dependence on Ca/(Si+Al) ratio in the double decomposition samples is thought to be due to the modification of the C-S-H structure from carbonation, as observed from XRD.

When C-S-H was treated with 0.1M solutions of NaOH, KOH, $NaNO_3$, and water, carbonation was detected by XRD. The most intense carbonate peaks were in samples that were treated with NaOH and KOH. Table 34 presents the MCL and $\%Q^3$ for each treatment. An increase in MCL and $\%Q^3$ are both results of the modification of C-S-H by carbonation. The data for the original C-S-H before treatment are also included.

Table 42: ^{29}Si NMR properties related to carbonation of treated samples.

	MCL	$\%Q^3$
NaOH	8.3	23.6
KOH	25.7	18.7
NaNO3	22.2	21.6
Original	9.2	6.1

The sample treated with KOH had the largest increase in MCL while the sample treated with NaOH had the largest increase in $\%Q^3$. Interestingly, the MCL for the NaOH treatment was lower than that of the original. The mass loss of carbonate, obtained from TGA, was 12.7% for NaOH, 12.9% for KOH, 6.7% for $NaNO_3$, and 10.1% for H_2O. The XRD and TGA results indicate that the samples treated with NaOH and KOH were more carbonated than those treated with $NaNO_3$ and H_2O. The ^{29}Si spectra are inconclusive in terms of the amount of carbonation that has occurred. From the XRD and TGA results, the pH, not sodium content, is affecting the carbonation rate of the C-S-H. When the reaction for the formation of $CaCO_3$ in water is examined, one of the reasons for this increase in carbonation is apparent.

$$CO_2 + 2OH^- \leftrightarrow CO_3^{2-} + H_2O$$

$$CO_3^{2-} + H_2O + Ca^{2+} \leftrightarrow CaCO_3 + H_2O$$

In a high pH solution there are more hydroxide ions present, which is on the reactant side for the reaction. Therefore, when the pH is high the reaction will proceed more quickly. Additionally, the solubility of $CaCO_3$ is affected by pH. Since the anion of $CaCO_3$ is the salt of a weak acid, CO_3^{2-} becomes protonated when acid is added to the solution and the concentration of carbonate ion is reduced. Le Chatelier's principle then dictates that some $CaCO_3$ will dissolve to maintain equilibrium. Thus, as pH is decreased the solubility of $CaCO_3$ increases. Therefore, at high pH the solubility of $CaCO_3$ is low and precipitation occurs more readily.

Further evidence of the effect of pH on carbonation of C-S-H can be seen from the carbonation of C-S-H samples synthesized by double decomposition and direct reaction. The pH of the supernatant solution of the C-S-H syntheses are presented in Table 43.

Table 43: pH values for C-S-H syntheses.

	pH
CSH_DD_1.0A	12.55
CSH_DD_1.3A	11.75
CSH_DD_1.5A	11.48
CSH_DR_1.0A	10.6
CSH_DR_1.3A	10.1
CSH_DR_1.5A	12.51

Generally, the C-S-H synthesized by double decomposition had a higher pH than C-S-H synthesized by direct reaction. The C-S-H synthesized by double decomposition showed more $CaCO_3$ polymorphs as indicated by XRD and higher MCL and Q^3 quantities as indicated by ^{29}Si NMR.

6. CONCLUSIONS

The primary objectives of this thesis were to synthesize C-S-H and C-A-S-H and characterize the structures. Changes were observed with varying Ca/Si ratios and aluminum content. Additionally, the effect of carbonation on synthesized C-S-H was examined. The use of ^{29}Si and ^{27}Al NMR provided critical information on the effect of varying Ca/Si ratio, aluminum content, and synthesis method.

The following conclusions can be drawn from this work:

- The MCL of C-S-H increases with decreasing Ca/Si.
- The dependence of MCL on Ca/Si ratio changes when different synthesis methods are used.
- The crystal structure of C-S-H does not change with Ca/Si ratio.
- Incorporation of Al in C-S-H is a dissolution/precipitation procedure.
- Al does not enter the octahedral CaO layer,
- Al[5] and Al[6] occur in the interlayer and/or the alumina/silica gel.
- The crystal structure does not change when aluminum is added to C-S-H.
- Al[4] does occur in the pairing tetrahedron position, but the bridging tetrahedron position is favored.
- A formula for MCL from ^{29}Si deconvolutions including Al[4] in the pairing tetrahedron position and Q^3 positions was derived.
- A formula for Al/Si from ^{29}Si deconvolutions including Al[4] in the pairing tetrahedron position and Q^3 positions was derived.

- The Al/Si ratio of the C-A-S-H is dependent on the concentration of aluminum in the solution when adding aluminum to already formed C-S-H.
- There is a weak negative correlation between the Ca/Si ratio and normalized Al[4] content.
- There is a weak positive correlation between the MCL and normalized Al[4] content.
- The chemical shift of the ^{27}Al spectrum is sensitive to the MCL or Ca/Si ratio of the C-A-S-H.
- The rate of carbonation of C-S-H is increased with higher pH.
- Double decomposition has longer MCL for a given Ca/Si, partially due to increased carbonation sensitivity.

7. REFERENCES

1. J.S. Dolado, M. Griebe, and J. Hamaekers, "A Molecular Dynamic Study of Cementitious Calcium Silicate Hydrate (C-S-H) Gels," *Journal of the American Ceramics Society* 90 (2007): 3938-3942.

2. G.K. Sun, J.F. Young, and R.J. Kirkpatrick, "The role of Al in C-S-H: NMR, XRD, and compositional results for precipitated samples," *Cement and Concrete Research* 36 (2006): 18-29.

3. G.L. Kalousek, "Crystal chemistry of hydrous calcium silicates: I. Substitution of aluminum in lattice of tobermorite," *Journal of the American Ceramics Society* 40 (1957): 74-80.

4. S. Kwan, J. LaRosa, and M.W. Grutzeck, "Structures and phase relations of aluminum-substituted calcium silicate hydrate," *Journal of the American Ceramics Society,* 79 (1996): 967-971.

5. P. Faucon, T. Charpentier, A. Nonat, and J.C. Petit, "Triple-quantum two-dimensional ^{27}Al magic angle nuclear magnetic resonance study of the aluminum incorporation in calcium silicate hydrates," *Journal of the American Chemical Society* 120 (1998): 12075-12082.

6. M.D. Andersen, H.J. Jakobsen, and J. Skibsted, “Incorporation of aluminum in the calcium silicate hydrate (C-S-H) of hydrated Portland cements: A high-field ^{27}Al and ^{29}Si MAS NMR investigation,” *Inorganic Chemistry* 42 (2003): 2280-2287.

7. K.J.D MacKenzie and M.E. Smith, *Multinuclear Solid-State NMR of Inorganic Materials* (Oxford: Pergamon, 2002), 50-74.

8. G. Engelhardt, “Silicon-29 NMR of Solid Silicates,” *eMagRes,* online (John Wiley & Sons, Ltd., 2007)

9. K.J.D MacKenzie and M.E. Smith, *Multinuclear Solid-State NMR of Inorganic Materials* (Oxford: Pergamon, 2002), 271-273.

10. I.G. Richardson, “The calcium silicate hydrates,” *Cement and Concrete Research* 38 (2008): 137-158.

11. X.D. Cong and R.J. Kirkpatrick, “^{29}Si MAS NMR study of the structure of calcium silicate hydrate,” *Advanced Cement Based Materials* 3 (1996): 144-156.

12. I.G. Richardson and G.W. Groves, “Models for the composition and structure of calcium silicate hydrate (C-S-H) gel in hardened tricalcium silicate pastes,” *Cement and Concrete Research* 22 (1992): 1001-1010.

13. H.F.W Taylor, “Proposed structure for calcium silicate hydrate gel,” *Journal of the American Ceramics Society* 69 (1986): 464-467.

14. I.G. Richardson, “The nature of C-S-H in hardened cements,” *Cement and Concrete Research* 29 (1999): 1131-1147.

15. H.F.W Taylor and J.W. Howison, “Relationships between calcium silicates and clay minerals,” *Clay Minerals* 3 (1956): 98-111.

16. H.G. Kurczyk and H.E. Schwiete, “Concerning the hydration productrs of C_3S and β-C_2S,” *Proceedings of the 4th International Symposium on the Chemistry of Cement*, 1 (1962): 349-358.

17. I.G. Richardson and G.W. Groves, “The incorporation of minor and trace elements into calcium silicate hydrate (C-S-H) gel in hardened cement pastes,” *Cement and Concrete Research* 23 (1993): 131-138.

18. I.G. Richardson, “Tobermorite/jennite- and tobermorite/calcium hydroxide-based models for the structure of C-S-H: applicability to hardened pastes of tricalcium silicate, β-dicalcium silicate, Portland cement, and blends of Portland cement with blast-furnace slag, metakaolin, or silica fume,” *Cement and Concrete Research* 34 (2004): 1733-1777.

19. A. Nonat and X. Lecoq, “The structure, stoichiometry and properties of C-S-H prepared by C_3S hydration under controlled conditions,” in *Nuclear Magnetic Resonance Spectroscopy of Cement-Based Materials* eds. P. Colombet, A.R. Grimmer, H. Zanni, and P. Sozzani, 197-207. Berlin: Springer, 1998.

20. J.J. Chen, J.J. Thomas, H.F.W. Taylor, and H.M. Jennings, "Solubility and structure of calcium silicate hydrate," *Cement and Concrete Research* 34 (2004): 1499-1519.

21. S. Komarneni, R. Roy, D. Roy, C. Fyfe, G. Kennedy, A. Bothner-By, J. Dadok, and A. Chesnick, "^{27}Al and ^{29}Si magic angle spinning nuclear magnetic resonance spectroscopy

22. P. Faucon, J.C. Petit, T. Charpentier, J.F. Jacquinot, and F. Adenot, "Silicon substitution for aluminum in calcium silicate hydrates," *Journal of the American Ceramics Society* 82 (1999): 1307-1312.

23. P. Faucon, T. Charpentier, D. Bertrandie, A. Nonat, J. Virlet, and J.C. Petit, "Characterization of calcium aluminate hydrates and related hydrates of cement pastes by ^{27}Al MQ-MAS NMR," *Inorganic Chemistry* 37 (1998): 3726-3733.

24. M.D. Andersen, H.J. Jakobsen, and J. Skibsted, "Characterization of white Portland cement hydration and the C-S-H structure in the presence of sodium aluminate by ^{27}Al and ^{29}Si MAS NMR spectroscopy," *Cement and Concrete Research* 34 (2004): 857-868.

25. P. Faucon, A. Delagrave, J.C. Petit, C. Richet, J.M. Marchand, and H. Zanni, "Aluminum incorporation in calcium silicate hydrate (C-S-H) depending on their Ca/Si ratio," *Journal of Physical Chemistry B* 103 (1999): 7796-7802.

26. J. Schneider, M.A. Cincotto, and H. Panepucci, "^{29}Si and ^{27}Al high-resolution NMR characterization of calcium silicate hydrate phases in activated blast-furnace slag pastes," *Cement and Concrete Research* 31 (2001): 993-1001.

27. P. Faucon, J.M. Delaye, J. Virlet, J.F. Jacquinot, and F. Adenot, “Study of the structural properties of the C-S-H(I) by molecular dynamics simulation,” *Cement and Concrete Research* 27 (1997): 1581-1590.

28. H. Manzano, J.S. Dolado, and A. Ayuela, “Aluminum incorporation to dreierketten silicate chains,” *Journal of Physical Chemistry B*, 113 (2009): 2832-2839.

29. H. Manzano, J.S. Dolado, M. Griebel, and J. Hamaekers, “A molecular dynamics study of the aluminosilicate chain structure in Al-rich calcium silicate hydrated (C-S-H) gels,” *Physica Status Solidi A* 205 (2008): 1324-1329.

30. M. Grutzeck, A. Benesi, and B. Fanning, “Silicon-29 magic angle spinning nuclear magnetic resonance study of calcium silicate hydrates,” *Journal of the American Ceramic Society* 72 (1989): 665-668.

31. I. Garcia-Lodeiro, A. Fernandez-Jimenez, I. Sobrados, J. Sanz, and A. Palomo, “C-S-H gels: Interpretation of ^{29}Si MAS-NMR spectra,” *Journal of the American Ceramics Society* 95 (2012): 1-7.

32. F. Puertas, M. Palacios, H. Manzano, J.S. Dolado, A. Rico, and J. Rodriguez, “A model for the C-A-S-H gel formed in alkali-activated slag cements,” *Journal of the European Ceramic Society* 31 (2011): 2043-2056.

33. I. Garcia-Lodeiro, A. Fernandez-Jimenez, D.E. Macphee, I. Sobrados, J. Sanz, and A. Palomo, "Stability of synthetic calcium silicate hydrate gels in presence of alkalis, aluminum, and soluble silica," *Transportation Research Record: Journal of the Transportation Research Board* 2142 (2010): 52-57.

34. I. Garcia Lodeiro, A. Fernandez-Jimenez, A. Palomo, and D.E. Macphee, "Effect on fresh C-S-H gels of the simultaneous addition of alkali and aluminum," *Cement and Concrete Research* 40 (2010): 27-32.

35. L. Black, C. Breen, J. Yarwood, K. Garbev, P. Stemmermann, and B. Gasharova, "Structural features of C-S-H(I) and its carbonation in air – A Raman spectroscopic study. Part II: Carbonated phases," *Journal of the American Ceramics Society* 90 (2007): 908-917.

36. H.F.W Taylor, *Cement Chemistry* (London: Thomas Telford, 1997), 114-116.

37. G.W. Groves, A. Brough, I.G. Richardson, and C.M. Dobson, "Progressive changes in the structure of hardened C_3S cement pastes due to carbonation," *Journal of the American Ceramics Society* 74 (1991): 2891-2896.

38. I. Garcia Lodeiro, D.E. Macphee, A. Palomo, and A. Fernandez-Jimenez, "Effect of alkalis on fresh C-S-H gels. FTIR analysis," *Cement and Concrete Research* 39 (2009): 147-153.

39. R. Alizadeh, J.J. Beaudoin, and L. Raki, "Viscoelastic nature of calcium silicate hydrate," *Cement & Concrete Composites* 32 (2010): 369-376.

40. K.J.D MacKenzie and M.E. Smith, *Multinuclear Solid-State NMR of Inorganic Materials* (Oxford: Pergamon, 2002), 146.

41. K.J.D MacKenzie and M.E. Smith, *Multinuclear Solid-State NMR of Inorganic Materials* (Oxford: Pergamon, 2002), 207.

42. S. Komarneni, R. Roy, C.A. Fyfe, G.J. Kennedy, and H. Strobl, "Solid-state ^{27}Al and ^{29}Si magic-angle spinning NMR of aluminosilicate gels,"*Communications of the American Ceramic Society* 69 (1986): 42-44.